INFORMATION TO USERS

This manuscript has been reproduced from the microfilm master. UMI films the text directly from the original or copy submitted. Thus, some thesis and dissertation copies are in typewriter face, while others may be from any type of computer printer.

The quality of this reproduction is dependent upon the quality of the copy submitted. Broken or indistinct print, colored or poor quality illustrations and photographs, print bleedthrough, substandard margins, and improper alignment can adversely affect reproduction.

In the unlikely event that the author did not send UMI a complete manuscript and there are missing pages, these will be noted. Also, if unauthorized copyright material had to be removed, a note will indicate the deletion.

Oversize materials (e.g., maps, drawings, charts) are reproduced by sectioning the original, beginning at the upper left-hand corner and continuing from left to right in equal sections with small overlaps.

ProQuest Information and Learning
300 North Zeeb Road, Ann Arbor, MI 48106-1346 USA
800-521-0600

University of Alberta

Study of the Droplet Surface Interaction Effects on a Naturally Laminar Flow Airfoil in Multi-phase Flow

by

Terry Michael Gunderson 

A thesis submitted to the Faculty of Graduate Studies and Research in partial fulfillment of the

requirements for the degree of Master of Science

Department of Mechanical Engineering

Edmonton, Alberta
Fall 2005

Abstract

Wind tunnel experiments were conducted on a naturally laminar-flight airfoil developed by ARC Development Corporation in a simulated rainfall with a liquid water content of 5.37 g/m^3 to determine the influence of rain on the aerodynamic performance at a Reynolds number of 300,000. This work was done after developing a set of procedures to test equipment within a multi-phase Marine Icing Wind Tunnel.

Testing to determine the effects of surface wettability on the aerodynamic performance of the airfoil during simulated rainfall was also conducted. Experimental results indicate that a hydrophilic coated airfoil had a significantly lower lift degradation in simulated rainfall than the non-coated airfoil whereas the hydrophobic coated airfoil had a much greater degradation in the aerodynamic performance. The relationship between the surface wettability and lift and drag are presumed to be due to the size of droplets created on the airfoil surface. Their subsequent interaction with the laminar boundary layer affects skin friction drag and the onset of separation. It appears that hydrophilic surfaces lead to thinner, more evenly distributed layers of liquid that have less impact on the boundary layer.

Acknowledgments

I would like to thank Dr. Brian Fleck and Dr. Ted Heidrick for their guidance throughout the completion of my thesis and during my course work. Their help during the final hours of my preparation was incredible. As well, I would also like thank Dr. Lorenz Sigurdson and Dr. Alidad Amirfazli for their expertise and advice in areas of my thesis topic. This thesis could not have been completed without the electrical knowledge of Terry Nord, the instrumentation knowledge of Bernie Faulkner, and the machining know how of Dave Roberts. I also benefited from two undergraduate research students, Kevin Dewar and Todd Meikle, whose help did not go unnoticed.

I would also like to thank my family and friends for their years of support. My parents, Terry and Alice, I wouldn't be here without you. I have relied on your support through the duration of both my undergraduate and graduate degrees. Wayne Klaczek, the two of us have burned the midnight oil studying for exams together, and you have become a truly amazing friend. Finally to my fiancee, Julie Mercer, who has sacrificed many date nights for thesis review nights, and who can love me like only a masters students' girlfriend could, thank you.

This research was completed with financial support from Dr. Brian Fleck. Personal funding was also received by the National Sciences and Engineering Research Council of Canada (NSERC), the University of Alberta, the Mechanical Engineering Department, Dr. Ted Heidrick, Dr. Brian Fleck and the Provincial Government to ensure that I was able to finish.

Table of Contents

List of Figures

List of Tables

Nomenclature

DAQ:	Data Acquisition
GUI:	Graphical User Interface
LE:	Leading Edge of airfoil
LWC:	Liquid Water Content (g/m^3)
MIWT:	Marine Icing Wind Tunnel
NACA:	National Advisory Committee for Aeronautics
TE:	Trailing Edge of airfoil

Symbols

A	=	Cross Sectional Spray Area of the Water Injection System (m^2)
$A_{airfoil}$	=	Projected Frontal Area of Airfoil (m^2)
A_p	=	Planform Area of Airfoil (m^2)
A_{wind}	=	Cross Sectional Area of Wind Tunnel (m^2)
BR	=	Blockage Ratio (dimensionless)
c	=	Chord Length of the Airfoil (m)
C_d	=	Coefficient of Drag (dimensionless)
C_l	=	Coefficient of Lift (dimensionless)
C_p	=	Pressure Coefficient (dimensionless)
g	=	Gravitational Constant, 9.81 m/s
h	=	Height of the Manometer Column (in gauge fluid)
$\dot{m}_w$	=	Injection Rate of Water (kg/hr)
M_{air}	=	Molecular Weight of Air, simplified mixture (kg/kmol)
N	=	Normal Component of Force (N)
P_{atm}	=	Local Atmospheric Pressure (Pa)
P_S	=	Static Air Pressure (Pa)
P_T	=	Total Air Pressure (Pa)
P_V	=	Velocity Air Pressure (Pa)
R_n	=	Resistance of 'n^{th}' Resistor (Ohms)
Re	=	Reynolds Number (dimensionless)
Re_c	=	Reynolds Number based on airfoil chord length (dimensionless)
St	=	Strouhal Number (dimensionless)
t	=	Thickness of the Airfoil (m)
T	=	Air Temperature (°K)
U_o	=	Free Stream Velocity of the Wind Tunnel (m/s)
U_T	=	Measured Wind Tunnel Velocity (m/s)
U_F	=	Corrected Wind Tunnel Velocity (m/s)
w_a	=	Width of the Airfoil (m)
w_t	=	Width of the Wind Tunnel Test Section (m)
We	=	Weber Number (dimensionless)
X	=	Chord-wise Component of Force (N)
z	=	Height of the Wind Tunnel (m)
α	=	Angle of Attack or Angle of Incidence (degrees)
ε_s	=	Blockage Factor (dimensionless)
θ	=	Experimental Contact Angle (degrees)
θ_A	=	Advanced Contact Angle (degrees)
θ_R	=	Receded Contact Angle (degrees)
ΔP	=	Difference Between the Total Pressure and Static Pressure (Pa)
λ	=	Airfoil Body Factor (dimensionless)
μ	=	Dynamic Viscosity (Ns/m^2)
ρ	=	Density of Fluid (kg/m^3)
ρ_{air}	=	Density of Air (kg/m^3)
ρ_{gauge}	=	Density of Manometer Fluid (kg/m^3)
τ	=	Wind Tunnel Factor (dimensionless)

1.0 Introduction

Recent interest in Micro Aerial Vehicles (MAVs), Unmanned Aerial Vehicles (UAVs) and Remotely Piloted Vehicles (RPVs) have revived the research on the performance of airfoils at relatively low Reynolds numbers ($50{,}000 < Re < 300{,}000$). Hansman et al. (1985) anticipates that the next generation of general aviation aircrafts will be designed using naturally laminar flow airfoils. The presence of light to heavy rainfall has adverse effects on low Reynolds number flight, as naturally laminar flow airfoils are very sensitive to environmental disturbances. Due the high sensitivity to environmental disturbances, low Reynolds number flight can be extremely dangerous to pilots who have been caught in an unsuspecting rainfall. According to a recent report by Lansberg (2004), in 1998, 17.3% of all aircraft fatalities (4.3% of all accidents) were the result of weather related accidents. While this number has dropped to 13.6% (3.6% of all accidents) for 2002, the number is still sobering. Also mentioned, was a 76.9% increase in the probability that an accident will result in a fatality when poor weather is involved. Haines et al. (1983) observed a 20% increase in drag coupled with a 30% reduction of lift of a naturally laminar flow airfoil in heavy rain rates (greater than 1800 mm/h). Water droplets collecting on the skin of the low Reynolds number airfoils cause a premature stall of flight. The effects of stalled flight have been the cause of many deaths in the recreational glider community.

Coatings on the airfoil that will change the droplet surface interaction properties are being investigated (Haines et al. 1983, Hansman et al. 1985, Marchmann et al. 1987, Thompson et al. 1995) to reduce the chance of an airfoil

entering a stalled condition. The main droplet surface characteristic under investigation is the surface wettability of a droplet on the airfoil skin surface. The contact angle between the water droplet and the airfoil skin surface may affect airfoil characteristics by changing how the water beads off the surface as well as the size of the individual water droplet beads. Lift and drag of the airfoil are the two main airfoil characteristics under investigation.

ARV Development Corporation, an Edmonton based aircraft kit manufacturer for aviation enthusiasts was seeking more information on their custom designed airfoil to determine its performance in rainy conditions. The ARV Development Corporation custom designed airfoil was tested at the Marine Icing Wind Tunnel (hereafter referred to as the MIWT) at the University of Alberta. The MIWT is capable of three phase flow, but during the testing, only two phase, two component (liquid water and air) flow was used. A series of experiments was conducted in single and two phase flow with Reynolds number ranging from 1.5×10^5 and 3×10^5 and angles of attack ranging from 0° to 16°. The series of experiments was then conducted with two airfoil surface coatings that altered the droplet surface interaction. Comparisons and conclusions were drawn between the dry condition and simulated rainfall over a range of angles of attack with three different airfoil surface conditions.

2.0 Statement of Objectives

The application of this research is for unmanned aerial vehicles, small wind turbines, and any other airfoils that operate in the "low Reynolds number regime" ($Re < 500{,}000$) that are susceptible to light or heavy rainfall.

The goals of this study are to:

1. Refurbish the existing Marine Icing Wind Tunnel (MIWT) at the University of Alberta in order to assist future research in areas which may include meteorological study.
2. Develop experimental procedures to facilitate the analysis of the water droplet surface interaction.
3. Determine the effects of various surface properties on the aerodynamic characteristics of airfoils in a water spray laden cross flow.

The MIWT (with a brine injection system) needed refurbishing after 15 years of intermittent use with little to no maintenance. An experimental procedure to use the new MIWT water injection system was required in order to facilitate preliminary data collection. Experiments were performed to determine the surface behavior characteristics. As well, these preliminary tests were fundamental in developing experimental procedures to provide a solid baseline for future researchers to further the development of droplet surface interaction theory in multiple phase, multi component flow.

3.0 Literature Review

The effects of rainfall on the lift and drag forces of an airfoil have been studied at various research institutions. The following discussed some of the previous research that is relevant to this study.

3.1 Airfoil Performance in Simulated Rain Conditions

3.1.1 Rain Effects at Low Reynolds Number

Marchman et al. (1987) conducted a study to determine the influence of rain on the aerodynamic properties of a Wortmann FX63-137 wing. The study was performed in a wind tunnel while varying the Reynolds numbers from 1×10^5 to 3×10^5. The study also investigated the wettability effects as the wing was tested with waxed and soaped surfaces. The tests were conducted in a closed circuit facility with a 1.8 x 1.8 x 8.5 m test section with the wing mounted on a 6 component balance. The 6 component balance measures 3 forces and 3 moments. The 3 forces that are measured are lift, drag and cross-wind force and the 3 moments that are measured are pitching, rolling, and yawing moments. In order to simulate rain conditions, seven ordinary garden spray nozzles were mounted horizontally 4.0 m upstream of the model. The spray nozzles were initially set in a wide flow pattern so that the nozzles would not have to be adjusted at higher air flow rates, and the flow was kept constant at 12.9 L/min in order for all rain experiments to maintain a uniform spray. The liquid water content could not be held constant during this experiment. The liquid water content was a function of spray area and the free stream

velocity; therefore, as the spray area was reduced due to the increase in free stream velocity, the liquid water content was reduced.

Liquid car wax was used to coat the wing during the nonwettable tests and glycerin soap, used during the wettable tests. While performing the wet experiments, the glycerin soap coating would wash away so that practical results could not be gathered for data analysis. The angle of attack was varied between -14° through to the stall point for the wet and dry experiments of the different surface coatings of the wing.

The dry wing results showed a linear coefficient of lift between -14° to 6° angle of attack. This linearity was attributed to a separation bubble (laminar separation followed by turbulent reattachment) that existed on the wing's lower surface. At large angles of attack, large pressure gradients overcame the force the separation bubble applied to attach the flow on the wing. Complete separation occurred when the flow was separated over the entire body of the wing. With a drastic reduction of the angle of attack, the flow would reattach to the wing again and perform a stalled wing hysteresis as normally characterized by a low Reynolds behavior of the flow.

In the wet wing case however, the rain nullified the effect of a normal low Reynolds behavior of the flow. The rainfall established a turbulent boundary layer on both the upper and lower wing surfaces. The difference in the coefficient of lift curve could be attributed to the elimination of the separation bubble inherent in laminar flow. With the elimination of the laminar bubble at higher angles of attack, the maximum coefficient of lift was lower than the dry wing case, but the massive-

surface separation that was found in the dry wing case, which resulted in the drastic stall, had been replaced by a gentle slope stall inherent in a turbulent flow wing. The coefficient of drag was also increased with the simulated rain.

Wax was applied to the surface of the wing that reduced the wing's wettability in order to determine the effects of the beading characteristics of water to the aerodynamic properties. The waxing did not affect the flow characteristics in the dry wing case, but the decreased wettability of the wing in the wet wing case further reduced the coefficient of lift.

Rain impacted the aerodynamic properties of the Wortmann FX63-137 airfoil at low Reynolds numbers more than those of most airfoils. Also, the rain might have been beneficial to low Reynolds number flight at high angles of attack, because the gentle stall caused by the rain would be better than the drastic reduction of lift during a laminar flow stall. Coating the wing with wax would cause a further deterioration of the wing performance because the water droplets accumulated in regions of flow separation. The accumulation within the region of flow separation changes the effective shape of the airfoil and enhances the separation process.

3.1.2 Surface Wetting Effects in Simulated Heavy Rain

Another study conducted by Hansman et al. (1985) determined the effects of heavy rainfall on a Wortmann FX-67-K-170 naturally laminar flow airfoil. The airfoil had a chord length of 16.2 cm (6 inches) and was mounted horizontally on a two component strain gauge balance in a 0.3 x 0.3 m test section. The test section was constructed from clear plexiglass to allow photographic observation. Water was

injected into the test section by commercial nozzles 1.5 m upstream to simulate rain conditions. The nozzles were adjusted to distribute the droplets uniformly over the entire test section. The wind tunnel air velocity was kept constant to maintain a Reynolds number of 3.1×10^5; as well, the water injection rate was kept constant to continually supply a liquid water content of 14.6 g/m^3 in order to simulate a rainfall of 440 mm/h. The airfoil was coated with 3 different coatings; an epoxy gel with a contact angle of 53°, a wax with a contact angle of 90°, and a soap coating. The soap coating proved to be more difficult to apply uniformly which resulted in physical and chemical irregularities on the wing surface. The lift and drag measurements were taken under both wet and dry conditions for all the surfaces applied at angles of attack between 0° and 16° in two degree increments. Photographs were taken of the upper surface of the airfoil from outside the test section.

There was a significant reduction in performance for all the surfaces tested under the simulated rain conditions. The Lift to Drag ratio (*L/D*) polar resulted in a downward translation in all cases with the simulated rain. As well, the waxed surface also showed an effective decrease of 2° for the angle of attack. The waxed airfoil experienced the greatest performance reduction of the *L/D* polar, with a reduction of approximately 75% from the dry gel coated base case. The wet gel coating had the least reduction in performance with an approximately 45% decrease in the *L/D* polar from the base case. This is contrary to the expectation that the soap covered surface would have the least reduction of performance; the soap covered airfoil had an intermittent reduction of performance in this case. This was attributed to the irregularities in the airfoil surface which would have increased the roughness in the

water layer. In all cases, there was a slight, but clear, reduction in the coefficient of lift under the simulated rain conditions. The angle of attack at which the maximum coefficient of lift was achieved also had a positive translation from the dry base case. There was an increase of the coefficient of drag for all simulated rain cases with the waxed coating case having the greatest increase.

The photographic results during the simulated rain conditions showed three distinct water behavioral regions; the water impingement zone, the forward runback zone and the aft runback zone. The water impingement zone was located at the leading edge of the airfoil and was dominated by droplet splashing. The droplet splashing created an ejecta fog of small droplets in front of the airfoil and could be visible by light scattering. The forward runback zone, which is located just downstream chord-wise of the water impingement zone, was dominated by a pushing effect of the water downstream of the airfoil by the air flow. The aft runback zone, the water seemed to be stagnant as surface tension became greater than the force from the air flow pushing the water downstream. Both the runback regions can be characterized by the Weber number, a dimensionless number which represents an index of the inertial force to the surface tension acting on a fluid element: a low Weber number implies that the effects of surface tension are important. The forward runback region would have a higher Weber number than the aft runback region. The transition between the forward and aft runback region was located at 50% chord length, but moved to 20% chord length as the angle of attack was increased. The gel coated airfoil displayed a fairly smooth surface in the forward runback region, and then the water droplets formed rivulets (runoff streams) which ran directly to the tail

of the wing where a small amount of water collected before being carried off by the air flow. The wax coated airfoil displayed a beading effect of water in the forward and aft runback regions. The water beads in the aft runback region were much greater in size than with the gel coated airfoil. The beads were dragged back to the tail of the wing where they were collected into even greater sized water beads before being carried off by the air flow.

The aerodynamic performance of a naturally laminar flow airfoil was reduced in the presence of simulated rain. The surface wettability effect showed that there is a possibility the effects of heavy rainfall can be minimized using surface coatings that increase the wettability of the surface which in turn will decrease the size of the water droplet beads. The size of the water beads contributes greatly to the degradation of the airfoil performance which was evident by the wax coating tests of the airfoil. The wax coated airfoil in simulated rain showed the greatest reduction of the *L/D* polar (approximately 75%) from the reference case of a dry gel coated airfoil. Conclusions from the soap covered airfoil may be suspect due to the physical and chemical irregularities while applying the coating, therefore were not considered.

3.1.3 Wing Performance in Moderate Rain

Thompson et al. (1995) conducted a study to determine wing performance at low Reynolds numbers in the presence of a moderate rainfall; as defined by a rainfall of 77 mm/h to 137 mm/h in the study. A NACA 4412 airfoil profile, with a rectangular profile and a chord length and wingspan of 6 inches and 36 inches, respectively, was mounted in the middle of a tunnel on three pressure side struts. The

aerodynamic forces and moments were determined by an external six component strain gauge balance. A data acquisition system was used to collect the mean values obtained from the six component strain gauge balance. The wind tunnel was equipped with windows in the side walls to allow visualization of the airfoil and the simulated rain. The dimension of the wind tunnel test section was 1.2 x 1.6 x 6.1 m. A chord Reynolds number of 2.5×10^5 was maintained by adjusting the wind tunnel flow rate. The wind tunnel air flow was measured using a Pitot tube mounted at the inlet to the test section. The water spray system used compressed air at 140 psi to pressurize water to a pressure of 80 psi in order to achieve an injection rate of 34.1 L/min. The water was injected through three nozzles that supplied a uniform spray throughout the test section located approximately 3 meters upstream of the airfoil. The spray bar was adjusted vertically to ensure that the leading edge of the airfoil was being sprayed by the water injection system. The mean droplet size measured in this study was 18 μm with a standard deviation of 1 μm.

The airfoil was placed in the wind tunnel with the wind tunnel flow rate and the water injection rate held constant, and the angle of incidence was varied from 2° to 8°, then to a final angle of incidence of 18°. Photographs were taken of the upper wing surface at each angle of incidence. At a 2° angle of incidence, the initial stages of rivulet formation occurred at 50% of the chord length, while the region forward of this was characterized by water sheeting. At 8° angle of incidence, the initial stages of rivulet formation occurred at 20% of the chord length. These rivulets appeared to have larger beads than the 2° angle of incidence case. At 18° angle of incidence, the water beads were formed in the water sheeting and rivulet forming

region. The airfoil was then subjected to rainfalls between 77 mm/h and 137 mm/h while increasing the angle of incidence in increments of 2°. In the range between 5° - 12° incidence, the airfoil experienced a 15% loss of lift, but at angles greater than the angle of incidence in which the maximum lift occurred, the surface water was delaying separation. This implied that an airfoil would experience greater lift at higher angles of incidence in rain than in dry conditions. This would lead to a higher margin of safety when approaching stall; as well, when stall was achieved in rain conditions, the drop in lift was much gentler than in dry conditions, giving the pilot more control of the airplane during stall. The coefficient of drag was increased at all angles of incidence. Below the 5° angle of incidence, the drag increase for all rain rates was approximately 15%. Between 5° and 12° angle of incidence, the coefficient of drag increased linearly, but it was also noted that the coefficient of drag also increased linearly with an increase in rain rate. This is contrary to the coefficient of lift, which was fairly constant through the 5° and 12° angle of incidence. This linear increase in drag due to an increase in the angle of incidence is believed to be attributed to an increase in skin friction along the airfoil. The authors' flow visualization results supported this belief which showed that the surface-water flow became more turbulent as the angle of incidence increased thereby increasing the drag.

The transition from laminar to turbulent flow occurred much farther down the chord length in low Reynolds number flight ($Re < 5x10^5$) than in higher Reynolds number flight. The transition and transition position in low Reynolds number flight was more sensitive to disturbances and irregularities in the free stream airflow, airfoil

profile, surface roughness and Reynolds number. Therefore, the transition was subjective to instabilities that were incurred in the leading-edge separation bubble. Rain caused a premature laminar to turbulent transition of the boundary layer. Visualization results showed four distinct regions of surface flow patterns which were identified as: droplet-impact, film-convection, rivulet formation and droplet convection regions.

The droplet-impact region extended to 6% of the chord length and was independent of rain rates. This region was characterized by the impact of droplets where large craters and waves were observed. Ejecta fog was seen on the leading edge of the airfoil and the authors believed that this droplet fog absorbed energy from the boundary layer which affected the downstream development of the boundary layer. For all angles of attack, the length of the droplet-impact region remained constant. The film-convention region is immediately aft of the droplet-impact region.

The film convection region was characterized by a transparent sheet covering the airfoil. The water was carried down the chord length in what appeared to be laminar flow with some surface waves created by the boundary layer flow. The film convection region decreased from 80% chord length to 50% chord length as the angle of attack was increased from -5° to 5°. In the 5° – 12° of incidence regime, the film convection region remained constant. From 12° – 18° of incidence, the region of film convection was reduced from 50% chord length to 20% chord length. After 18° of incidence, the film convection region by definition was non-existent.

Downstream from the film-convection region was the rivulet-formation region. Water beads and rivulets formed in this region, where the sinuosity,

wavelength and amplitudes were dependent on the rain rate. The distance between two rivulets was also dependent on the rain rate. When the angle of incidence was increased from -5° to 5°, the region of rivulet-formation increased in area, which resulted in linear increase in the coefficient of lift. From 5° – 12° angle of incidence, the beads of water in the rivulets increased to approximately 5 mm in diameter, but the region of rivulet formation stayed constant, as did the coefficient of lift. The size of the beads in the rivulets increased dramatically, from 5 mm to 15 mm, and was stagnated in both the rivulet-formation and droplet-convection region when the angle of incidence was increased to 18°. The coefficient of lift increased incrementally with the increase of incidence. As with the film convection region, the rivulet-formation region became non-existent after 18° of incidence.

The droplet-convection region was the leeward most region along the chord length. This region was characterized by the coalescing of beads where they were dragged to the trailing edge of the airfoil before being torn away by the external flow. As the angle of incidence increased, so did the size of the droplet-convection region increase. At angles of incidence greater than 18°, the droplet-convection region absorbed the film-convection and rivulet-formation region.

The percentage of the wing that was covered with each flow pattern region was largely dependent on the angle of attack of the airfoil.

3.1.4 Scaling Laws of Airfoils in Heavy Rainfall

Bilanin (1985) conducted theoretical models of high lift airfoils under heavy rainfall in which he determined some scaling laws between models and full size

airfoils. The author warned that the extrapolation of small scale data to full scale conditions must be undertaken with extreme caution, as incorrect scaling laws could seriously impact performance predictions. Previous papers by authors using experimental data (such as Haines et al. 1983) concluded that heavy rainfall would reduce the stall angle and the maximum coefficient of lift by 30%. These results were contrary to articles published by authors using analytical techniques that showed that under heavy rainfall, the lift would actually increase, though these authors generally neglected droplet interactions with the wing surface. Previous papers presented (Haines et al. 1983, Luers et al. 1983, Luers, 1983) that used experimental data on the performance of laminar flow airfoils, showed a lift penalty when operating in heavy rainfall. Therefore, it appears that scaling laws must be developed in order to test small scale airfoils under heavy rain conditions. The greatest rainfall ever recorded achieved rainfall rates of 1872 mm/hr; nevertheless, the actual liquid water content was only 80 g/m^3. Assuming a mean droplet diameter of 4 mm, the mean distance between droplets in a heavy rainfall would be in the order of 7 cm. As the thickness of a wing is in the order of fractions of a meter, it is safe to assume that many droplets will impact the wing simultaneously; therefore, if small scale testing is done without changing the mean distance between drops, it will have serious implications on the scalability of the results.

Small scale tests can be at lower Reynolds number unless very high air velocities are used (possibly resulting in Mach number issues) since models are a fraction of the full scale size. Generally, wind tunnel velocities are not available to offset the model size reduction in such cases. This distortion of Reynolds number can

be modeled in dry testing by methods such as implementing devices that trip the boundary layer, which can be added onto the airfoil. When rain is introduced, a second Reynolds number involving the viscosity of water is also distorted at small scale, which is not easily modeled in small scale and therefore, introduces a difference between the small scale model to the real scale. A third parameter, the Weber number squared, may not be preserved as the velocity must vary as the scale size is reduced. Surface tension may need to be modified as well as it affects the wettability of the surface which in turn affects the rivulet formation. Therefore the same material that is used in aircraft design may not be applicable in subscale testing. The rainfall rate will not scale either, for example, if the model to full scale ratio is 1/4, then a rainfall of 100 mm/hr would result in a scaled rainfall of 38 mm/h.

In conclusion, it is clear that data collected from small scale models need to be extrapolated with extreme caution as many parameters (Reynolds number, Weber number, film thickness, airfoil wettability and rivulet formation) may experience a distortion in the scaling laws.

3.2 Droplet Contact Angle

3.2.1 Measuring Contact Angles

Kwok et al. (1998) conducted studies on a FC-725 coated wafer using 30 different liquids to determine contact angle behavior. An important relationship in the field of contact angle research is Young's equation, [1]. The Young contact angle (θ_Y) is determined by relating the liquid-vapor surface tension (γ_{lv}), solid-vapor surface tension (γ_{sv}), and the solid-liquid surface tension (γ_{sl}).

$$\gamma_{lv}\cos\theta_Y = \gamma_{sv} - \gamma_{sl} \qquad [1]$$

The solid-vapor and solid-liquid surface tension are not directly measurable; therefore, other relations to determine these unknown surface tensions are necessary in order to determine the Young contact angle. The Young's equation gives the sense that there is only one unique contact angle; whereas in practice, it is widely known that many contact angles exist and the term contact angle can be convoluted. Figure 6 shows a receding (θ_R) and advancing (θ_A) contact angles, where the difference between these two angles is the contact angle hysteresis. On ideal solid surfaces, there is no contact angle hysteresis and the experimental contact angle, (θ), is equal to the Young contact angle. In experiments however, the contact angle that is measured is not necessarily equal to the Young contact angle due to contact angle hysteresis. On smooth surfaces the advanced contact angle can be a good approximation of the Young contact angle; therefore, great care must be practiced in experiments to ensure that the apparent advanced contact angle is being measured.

The apparent contact angle increases linearly with the drop volume in the case where the fluid is water. This is due to contact angle hysteresis, where the water drop's apparent contact angle will increase until the advancing contact angle is reached. Even if great care was taken to place an initial droplet of fluid on the surface, and then another droplet was placed within the existing drop, the apparent contact angle may still be between the advancing and receding contact angle. The solution to this is to increase the droplet volume until the droplet visibly advances to ensure that the advanced contact angle is being measured. As opposed to many other liquids, water does not display the slip/stick behavior, which is inherent in many

liquids. The contact angle of water can be described to behave linearly to the drop volume.

3.2.2 Contact Angle Hysteresis

Krasovitski et al. (2005) conducted a theoretical study of the contact angles that are measured during a tilted plate experiment. An equation that is widely used in publications is shown in [2], which relates the slip angle (α) to the contact angles at the upper edge (θ_{min}) and the lower edge of the drop (θ_{max}):

$$\sin\alpha = C\sigma(\cos\theta_{\min} - \cos\theta_{\max}), \qquad [2]$$

where C is a constant which includes gravitational acceleration, density of the liquid and geometrical parameters of the drop, and σ is the surface tension of the droplet. The authors' argument is within the definition of θ_{min} and θ_{max} as traditionally these have been characterized by the receded and advanced contact angles, respectively. Therefore, the main objective of the authors' study was to determine if a relationship between the θ_{min}, θ_{max}, θ_R, and θ_A could be drawn.

The theoretical models during this study were derived using a relatively hydrophilic surface ($\theta = 30°$) and a relatively hydrophobic surface ($\theta = 110°$) using water ($\sigma = 73$ mN/m, $\rho = 1000$ kg/m^3). The first model presented the dependence of the slip angle (α) to the drop volume. As expected, in both the hydrophobic and hydrophilic case, the slip angle was sensitive to the drop volume, but counter-intuitively, the slip angle was more sensitive to the drop volume in the hydrophilic case than in the hydrophobic case. From the theoretical results, the minimum and maximum contact angle would differ from the receding and advancing contact angle,

but as the range of hysteresis decreased, θ_{min} would approach θ_R and θ_{max} would approach θ_A. The results show that in the hydrophobic case, θ_{max} was much smaller than θ_A, but θ_{min} was similar to θ_R. In the hydrophilic case, these results were reversed where the θ_{max} was similar to the θ_A, but θ_{min} was much higher than θ_R. Therefore, it was concluded that the minimum and maximum contact angle during the tilted plate experiment did not necessarily equal the receding and advancing contact angles, respectively. Consequently, determining the range of hysteresis by analyzing the shape of the droplet on an inclined plane was misleading.

4.0 Theory

4.1 Wind Tunnel

This section will describe the theory that deals with the Marine Icing Wind Tunnel (MIWT) measurements.

4.1.1 Blockage

4.1.1.1 Blockage Ratio

The blockage ratio is a ratio of the cross sectional area of the wind tunnel that the frontal area of the airfoil occupies. During this study, the blockage ratio was constrained to a value of approximately 10%, as advised by Barlow et al. (1999). The blockage ratio (BR) is determined from the projected frontal area of the airfoil ($A_{airfoil}$) compared to the cross sectional area of the test section (A_{wind}) as seen in Figure 1. The relationship can be described as follows:

$$BR = \frac{A_{airfoil}}{A_{wind}} \qquad [3]$$

As the airfoil spans the entire test section, the blockage ratio can be reduced to the ratio of the widths of the airfoil (w_a) to the test section (w_t). Using a 10% blockage ratio, the following relationship can be derived using simple trigonometry, to determine the maximum angle of attack (α) from the chord length (c) of the airfoil:

$$\alpha = \sin^{-1}\left[\frac{BR \cdot w_t}{c}\right] \qquad [4]$$

With a blockage ratio of 10%, a chord length of 20 cm, and a wind tunnel width of 50 cm, the maximum angle of attack is calculated to be 15°. For this study, a maximum angle of attack of 16° will be used, which relates to a blockage ratio of 11.0 %.

4.1.1.2 Tunnel Interference Effects

When conducting experiments in a closed section wind tunnel, the effects the walls have on the streamlines must be considered. An effect of the wall constraint is the suppression of the lateral expansion of the streamlines in the region of the model as seen in Figure 2. This suppression effect will produce an increase in the axial component of velocity along the airfoil. Thus, the influence the walls place on the experiment will be an increase in the axial wind speed at the location of the model airfoil. Therefore, a correction to the tunnel speed, the dynamic head and to Reynolds number must be made (Pankhurst, 1965).

The wind tunnel speed (U_T) is measured in an empty test section, where a blockage factor (ε_s) is applied and the corrected wind tunnel speed (U_F) at the location of the model is described by the following:

$$U_F = U_T(1+\varepsilon_s) \qquad [5]$$

The blockage factor from [5] has been determined from Lock (1929) to be of the order $(c/h)^2$ for 2 dimensional flow. Therefore the airfoil may be represented by doublets (at the same location as the airfoil) which create the identical velocity field around the airfoil. The walls of the wind tunnel are then represented by system of

images of the equivalent doublets. The blockage is then calculated by the velocity induced, at the position of the model, by the equivalent doublets. (Pankhurst, 1965)

The blockage factor is a function of the tunnel factor (τ), the thickness of the airfoil (t), the height of the wind tunnel (z), and the body factor (λ) based on the geometry of the airfoil profile. λ is a dependant on the geometry of the profile of the wing with the camber removed. The relation of these variables to the blockage factor is as shown (Lock, 1929):

$$\varepsilon_s = \tau\lambda\left[\frac{t}{z}\right] \qquad [6]$$

The tunnel factor from [6] is based on the geometry of the wind tunnel and the position of the model within the wind tunnel. For a closed loop system, Batchelor (1944) has determined the tunnel factor, τ can be determined by the following equation:

$$\tau = \frac{\pi^2}{12}\left[1+\frac{3\pi^2}{4}\frac{a^2}{z^2}\right] \qquad [7]$$

The model airfoil was placed along the tunnel axis at an equal distance from each side wall, therefore:

$$a = 0 \qquad [8]$$

By applying [8] to [7] the second term goes to zero and the tunnel factor can be reduced to:

$$\tau = \frac{\pi^2}{12} = 0.822 \qquad [9]$$

To determine the shape factor of the airfoil, the following relation that is used for an ellipse will be used to describe the airfoil:

$$\lambda = \frac{1}{2}\left(1+\frac{c}{t}\right) \qquad [\ 10\ ]$$

Combining [10] and [9] into [6], the blockage factor can be rewritten as:

$$\varepsilon_s = 0.822\left[\frac{t+c}{z}\right] \qquad [\ 11\ ]$$

Applying the blockage factor to [5], the corrected wind tunnel speed is shown as:

$$U_F = U_T\left[1+0.822\left(\frac{t+c}{z}\right)\right] \qquad [\ 12\ ]$$

Pope (1961) gave a relationship to the corrected Reynolds number (Re_F) from the measured Reynolds number (Re_T) using the blockage factor as:

$$\mathrm{Re}_F = \mathrm{Re}_T(1+\varepsilon_s) \qquad [\ 13\ ]$$

The effect that the tunnel interference has on the Reynolds number will be the same as the effect on the wind tunnel speed; an increase of 39.0% to the Reynolds number.

4.1.2 Velocity Measurement Using a Pitot Tube

The velocity profile of the MIWT is fully developed in the test section; therefore, the reading that was taken by the Pitot tube will be considered the centerline velocity.

The Pitot static tube measures the total pressure (P_T) at the tip of the Pitot tube and the static pressure (P_S) of the fluid flow at ports located downstream of the tip on the side of the Pitot tube. Figure 3 shows a Pitot static tube.

The static pressure and total pressure outlet ports are connected to a manometer where the difference between these two pressures is measured. The dynamic pressure, or velocity pressure, (P_V) is the difference between the total pressure and static pressure in the MIWT as shown in Equation [14].

$$\Delta P = P_V = P_T - P_S \qquad [\ 14\ ]$$

The readings from the inclined manometer were measured in units of length of gauge fluid with a specific gravity of 0.826. These units can be converted to a more practical form of pressure by using a simplified Bernoulli's Equation reduced to the hydrostatic pressure equation:

$$\Delta P = \rho_{gauge} g h\,, \qquad [\ 15\ ]$$

where the gravitational constant (g) and the density of water (ρ_{water}) is considered to be 9.81 m/s^2 and 1000 kg/m^3, respectively. The height of the fluid column (h) is measured directly off the inclined manometer.

To determine what the MIWT operating velocity is, a simplified Bernoulli's Equation, [16], is used. The Bernoulli's Equation is a reduction of the Navier-Stokes Equations along a streamline.

$$\Delta P = \frac{\rho_{air} U^2}{2} \qquad [\ 16\ ]$$

Rearranging [16], gives the MIWT air flow velocity in terms of the air density (ρ) and the pressure difference (ΔP).

$$U = \sqrt{\frac{2\Delta P}{\rho_{air}}} \qquad [\ 17\ ]$$

The air density (neglecting humidity) can be described by using the ideal gas law [18], where $R_u = 8315$ J/kmol·K and the molecular weight of air (M_{air}) is 28.97 kg/kmol, assuming a simplified air mixture of 79% N_2 and 21% O_2.

$$\rho_{air} = \frac{m}{V} = \frac{P}{RT} = \frac{P_{atm}}{\left(\frac{R_u}{M_{air}}\right)T} \qquad [18]$$

The corrected atmospheric pressure was determined before each day of testing from a barometer located on the third floor Mechanical Engineering Building. The temperature inside the MIWT test section was taken before each day of testing by a thermometer.

Once the MIWT operating temperature and the corrected atmospheric pressure were measured, MIWT air flow velocity could be determined using [17] and substituting in [15] and the density calculated in [18].

$$U = \sqrt{\frac{2(s.g.)\rho_{water}gh}{\rho_{air}}} \qquad [19]$$

4.1.3 Liquid Water Content

The liquid water content (*LWC*) is a parameter that relates the mass of water crossing a vertical plane at the wing to the volume of air flowing past the wing (Marchman et al. 1987). As noted by Bilanin (1985), water injection systems in experiments do not simulate the water droplet size and droplet scattering distributions or the mean distance between droplets well. Therefore, the LWC is a preferred method to denote the droplet laden cross-flow intensity at the wing as opposed to

droplet laden cross-flow rates. The liquid water content is a function of the injection rate of water ($\dot{m}_w$), the free stream velocity (U_o) and the cross sectional area spray area of the water injection system (A). [20] shows the relationship between these variables; LWC is typically presented in units of g/m^3.

$$LWC = \frac{\dot{m}_w}{U_o A} \qquad [20]$$

The water injection rate was kept constant to avoid surging in the simulated rainfall. Therefore, the LWC of the droplet laden cross-flow could not be kept uniform through the range of Reynolds number because of the non-linear dependence on the free stream velocity. From [20], it is easy to see that:

$$LWC \propto \frac{1}{U_o A} \qquad [21]$$

But the cross sectional area of the water injection spray is proportional to the free stream velocity to an undetermined exponent, n:

$$A \propto \frac{1}{U_o^n} \qquad [22]$$

By combining [22] and [21], it is easy to see that the LWC is proportional to the free stream velocity to some exponent m as shown in [23].

$$LWC \propto U_o^m \qquad [23]$$

From previous papers studied (Hansman et al. 1985, Marchman et al. 1987), the value of m would be negative as the LWC decreases as U_o increases.

4.2 Airfoil

4.2.1 Reynolds Number

When using a wind tunnel to conduct tests of a model to determine properties or effects of properties that will be used in a full scale application, several important parameters must be used in order to properly predict these scalable results. When dealing with aerodynamics, an important parameter is matching the Reynolds numbers of the model with the full scale model. A body moving in an immersed fluid will effect an inertial force around the body in the fluid in which it is immersed. The inertial force is a function of the density of the fluid in which it is immersed, ρ, the velocity of the body within the fluid, V, and the effective volume of fluid which is affected, kl^3; where k is a constant for the particular body shape and l is the characteristic length.

$$Inertia\ Force \sim \frac{\rho l^3 V}{t} \qquad [24]$$

Time, t, can be substituted as a ratio of velocity and distance as shown by:

$$Inertia\ Force \sim \frac{\rho l^3 V}{l/V} \sim \rho l^2 V^2 \qquad [25]$$

The body that is moving through the immersed fluid will experience a force that is due to the viscosity of the fluid and can be shown as:

$$Viscous\ Force \sim \mu V l \qquad [26]$$

The Reynolds number is a ratio between the inertia forces and the viscous forces, which is also a ratio between the pressure forces and the skin friction:

$$\mathrm{Re} \sim \frac{inertial\ forces}{viscous\ forces} \qquad [27]$$

Substituting [25] and [26] into [27] renders the following definition of Reynolds number:

$$\mathrm{Re} = \frac{\rho U l}{\mu} \qquad [28]$$

4.2.2 Boundary Layer Equations

The laminar boundary layer equation can be developed from the x component of a simplified Newton's second law.

$$\sum F_x = ma \qquad [29]$$

A free body diagram, see Figure 4, is used to show the forces acting on an element. The drag, D, can be described as a function of the shear force, τ_w, and the element area, A and is shown as:

$$D = -\int \tau_w dA \qquad [30]$$

Newton's second law [29] can then be applied to the free body diagram with the pressure forces, P acting on the element.

$$P_1 A_1 - P_2 A_2 - D = (\rho A \Delta x) \cdot \left(\frac{D\bar{v}}{Dt} \right) \qquad [31]$$

The total derivative of velocity, $\bar{v}$, can be expanded for the x component case, and [30] can be substituted into [31]. The equation can also be transformed by moving the mass term to the left hand side of the equation rendering the following:

$$\frac{P_1 - P_2}{\rho \Delta x} + \frac{\int \tau_w dA}{\rho A \Delta x} = \frac{\partial \bar{v}}{\partial t} + \bar{v} \frac{\partial \bar{v}}{\partial x} \qquad [32]$$

It is assumed that there is steady flow, therefore:

$$\frac{\partial \bar{v}}{\partial t} = 0 \qquad [33]$$

By implementing [33] into [32] and rewriting the form of the equation, the following can be shown:

$$\frac{-1}{\rho}\frac{\partial P}{\partial x} + \frac{1}{\rho}\frac{\partial \tau_w}{\partial x} = \bar{v}\frac{\partial \bar{v}}{\partial x} \qquad [34]$$

which can be written in the more general form:

$$\bar{v}\cdot\nabla\left(\bar{v}\right) = \frac{-1}{\rho}P + \frac{\mu}{\rho}\nabla^2\bar{v} \qquad [35]$$

This is the steady Navier Stokes uniform density equation where μ is the viscosity of the fluid. The boundary layer equations an approximation of the Navier Stokes equation near the wall. To calculate the boundary layer three assumptions are made:

1. $P = constant$ [36]
2. $v = 0$ [37]
3. $\frac{\delta}{\delta x} = 0$ [38]

The first assumption says that the pressure is constant, which also means that the separation point can not be calculated. The second assumption states that the velocity component normal to the surface (v) within the boundary layer is zero (the tangential component of velocity within the boundary layer is denoted by u). The third assumption states that the boundary layer changes faster in the normal direction than the y direction. Applying these assumptions, the following relations are made for the x component and y component:

$$u\frac{\partial u}{\partial x}+v\frac{\partial u}{\partial y}=\frac{-1}{\rho}\frac{\partial P}{\partial x}+\frac{\mu}{\rho}\left[\frac{\partial^2 u}{\partial x^2}+\frac{\partial^2 u}{\partial y^2}\right] \qquad [39]$$

$$u\frac{\partial v}{\partial x}+v\frac{\partial v}{\partial y}=\frac{-1}{\rho}\frac{\partial P}{\partial x}+\frac{\mu}{\rho}\left[\frac{\partial^2 v}{\partial x^2}+\frac{\partial^2 v}{\partial y^2}\right] \qquad [40]$$

Equation [39] reduces to the following momentum equation:

$$u\frac{\partial u}{\partial x}+v\frac{\partial u}{\partial y}=\frac{\mu}{\rho}\frac{\partial^2 u}{\partial y^2} \qquad [41]$$

Equation [40] renders a zero value on both the left hand side and the right hand side so therefore the continuity equation is used:

$$\frac{\partial u}{\partial x}+\frac{\partial v}{\partial y}=0 \qquad [42]$$

To solve [41] and [42], the Blasius Transformation is applied:

$$\eta=y\left[\frac{U}{\nu x}\right]^{1/2} \qquad [43]$$

where ν is the kinematic viscosity

and by defining the stream function as:

$$\psi=\sqrt{\nu x U}\cdot f(\eta) \qquad [44]$$

After applying the transformation and defining the stream function, an ordinary differential equation is obtained which is solved numerically. From this numerical solution, the edge of the boundary layer and the boundary layer thickness can be determined. The boundary layer edge is commonly solved using the δ_{99} method, which states that the boundary layer edge occurs at a location where the tangential component of velocity within the boundary layer is 99% of the free stream velocity:

$$u = 0.99U_{\infty} \qquad [45]$$

This has been solved numerically so that [43] is can be described as:

$$\eta = \delta\sqrt{\frac{U}{\nu x}} = 5 \qquad [46]$$

Rearranging [46] so it is a function of the dimensionless Reynolds number parameter as shown in [28] gives the following relation for the laminar boundary layer thickness:

$$\delta = \frac{5.0x}{\sqrt{\frac{\rho U x^2}{\mu x}}} = \frac{5.0x}{\mathrm{Re}_x^{1/2}} \qquad [47]$$

For turbulent flow, empirical data is required to determine the boundary layer equation. The Blasius one-seventh power law is often used to describe the velocity distribution as derived from pipe flow:

$$\frac{u_x}{U_o} = \left[\frac{y}{\delta}\right]^{1/7} \qquad [48]$$

The von Kármán Momentum Integral:

$$\frac{\tau_o}{\rho} = \frac{d}{dx}\int_0^{\delta} u_x\left(U_0 - u_x\right) dy \qquad [49]$$

is used in conjunction with [48] which renders:

$$\frac{\tau_o}{\rho} = \frac{d}{dx}\int_0^{\delta} U_o^2\left[\left(\frac{y}{\delta}\right)^{1/7} - \left(\frac{y}{\delta}\right)^{2/7}\right] \qquad [50]$$

The power law doesn't hold true at the wall as,

$y \to 0$,

so a Blasius correlation for shear stress at the wall for pipe flow is used:

$$\frac{\tau_o}{\rho U_o^2} = 0.023\left(\frac{\delta U_o \rho}{\mu}\right)^{-1/4} \qquad [51]$$

Integrating [50] and substituting [51] renders the following equation:

$$\frac{\delta}{x} = 0.376\left[\frac{\rho U_o x}{\mu}\right]^{-1/5}, \qquad [52]$$

which can be transformed to the final form of the turbulent boundary layer thickness equation:

$$\delta = \frac{0.376x}{\mathrm{Re}^{0.2}} \qquad [53]$$

4.2.3 Contact Angle

The contact angle (θ) is the characteristic angle at which a liquid rests on a surface (measured in the liquid), a quantitative measure of the wetting of a surface by a liquid. The contact angle is measured at a point where the liquid and the three phase boundary intersect. A tangential line is then drawn from the liquid/gas barrier through the aforementioned point. The three phase point forms the apex of the angle measured, with the reference arm running tangent to the liquid/solid barrier. This contact angle measurement technique is illustrated in Figure 5.

Simply measuring the contact angle of the liquid bead is not adequate. There are many different definitions of contact angles, but in the static case, the contact angle definitions that will be discussed are the 'advanced contact angle' and the 'receded contact angle'. The difference between these two contact angles is illustrated in Figure 6. The value of the contact angle is dependent on the history of

the fluid; if the drop volume has been expanded, the value will typically be close to the advanced contact angle, whereas if the drop volume has been reduced, the value of the contact angle will typically be close to the receded contact angle. The simple static measurement of a contact angle will fall between these two characteristic contact angles of the liquid. Even in the case of carefully placing an initial droplet on the surface, then adding an additional drop, the value of the contact angle measured may result in a value between the receded and advanced contact angle (Kwok et al. 1998). The difference between the receded and advanced contact angles is defined as the contact angle hysteresis. There are two thoughts that exist in the literature of contact angle hysteresis; contact angle hysteresis is viewed as a consequence of solid surface area, or it is the contact perimeter of the solid surface area which is viewed as important (McHale et al. 2004).

It is very important to determine which contact angle is being measured, and because of that, a standard method is used to ensure that the same definition of contact angle is used through all the experiments. The standard method is called Goniometry. Goniometry requires a light source, camera, and image capturing. A droplet is placed on a surface which then is tilted to a set angle to give the characteristic contact angles of the liquid bead. A photograph is taken with a camera and the image is captured. The advanced and receded contact angles are then directly determined by measuring the angle formed between the liquid/solid barrier and the tangent formed by the liquid/gas barrier which runs through the three phase boundary intersect.

Some liquids possess a slip/stick behavior on surfaces. A slip/stick behavior occurs when a liquid droplet sticks or clings to the surface which results in greatly exaggerated hydrophobic properties between the surface and liquid. The true advanced contact angle would not be measured. Kwok et al. (1998) noted that water does not display this slip/stick behavior.

4.2.4 Surface Wettability

The surface wettability is often expressed in terms of contact angle when working with liquids. The relationship between contact angle and surface wettability is shown in Figure 7. A completely wettable surface would theoretically have a contact angle of 0° where the liquid would sheen over the surface evenly. In this experiment, a wettable surface will be defined as having a contact angle less than 25°. A completely nonwettable surface would theoretically have a contact angle of 180° where the liquid would ball up and resist any spreading along the surface. In practice, a surface is said to be nonwettable when the contact angle is 90° or greater. For a partially (incompletely) wettable surface, the contact angle between the surface and the water droplet is between 0° and 90°. The contact angle is not a function of droplet volume as the droplet will spread across the surface to maintain the characteristic contact angle, but for a given volume of fluid, the droplet height will decrease with wettability and increase with contact angle.

Haines et al. (1983) postulated that on a fairly wettable airfoil, the waviness of the surface created by the sheen of water (water film) covering the airfoil will increase the drag and decrease the lift. Conversely, Marchman et al. (1987)

determined that for a nonwettable surface, the beads of water cause further deterioration of the wing performance as they collect in regions of flow separation effectively changing the shape of the airfoil and enhancing the separation process.

4.2.5 Weber Number

The Weber number is an ratio of the inertial force to the surface tension force acting on a fluid element:

$$We = \frac{\rho U^2 l}{\sigma} \qquad [54]$$

Weber number is a function of the droplet density (ρ), droplet velocity (U), the characteristic length (l) and the surface tension (σ). The Weber number is a tool used for analysis of thin film flows and the formation of droplets and bubbles. A low Weber number implies that the effects of surface tension are important.

Hansman et al. (1985) characterized four regions of an airfoil in simulated rainfall where two of the regions were based on Weber numbers of the water droplets. The forward runback region was dominated by a pushing effect of the water downstream of the airfoil by the air flow, thus a higher Weber number. In the aft runback zone, the water seemed to be stagnant as surface tension became greater than the force from the air flow pushing the water downstream, which would be represented by a low Weber number.

4.2.6 Strouhal Number

The Strouhal number is a dimensionless number describing oscillating flow mechanisms. It is the ratio of inertial forces due to unsteadiness of the flow to the inertial forces due to velocity change from one point to another in a flow field. Objects that are placed into fluid flow will create a series of alternating vortices on the trailing edge. Strouhal number is normally defined in the following form:

$$St = \frac{f \cdot L}{U_o}, \qquad [55]$$

where f is the frequency of vortices shed in a vortex street, L is the length scale, and U_o is the speed of fluid flow. For airfoils impinging on the stall angle, an unsteady flow oscillation exists which has a very low frequency where the Strouhal number is near the value of 0.2. The length scale for an airfoil is defined as:

$$L = c\sin\alpha, \qquad [56]$$

where c is the airfoil chord and α is the angle of attack. Combining [56] with [55], the Strouhal number for an airfoil can be defined as:

$$St = \frac{f \cdot c\sin\alpha}{U_o} \qquad [57]$$

Broeren et al. (1998) concluded that the flow oscillation involved quasiperiodic switching between stalled and unstalled states. The unsteady stall was related to the growth and bursting of a laminar separation bubble.

4.3 Instrumentation

4.3.1 Strain Gauges and Wheatstone Bridge

Strain gauges are commonly used devices to measure strain in industrial applications where a high level of accuracy in the measurement is necessary. Strain gauges are attached to a material that will be placed under stress. Resistance in an electrical resistance strain gauge changes proportionally to the amount of strain induced on the strain gauge. Using this principle, series of strain gauges can be used to accurately measure the strain induced on a body when an excitation voltage is applied by measuring the change in output voltage. During this study, the series of strain gauges were connected in a full Wheatstone bridge configuration. When a full Wheatstone bridge configuration is made, the measurements of strain are temperature compensated, meaning that strain due to thermal expansion of the airfoil was compensated for.

4.3.2 Determining the Lift and Drag from the Strain Gauge Output

The strain gauges were applied onto a cantilevered section of the airfoil to measure the strain induced by the free stream velocity in the normal and chord-wise direction. The strain gauges were then calibrated using calibration weights so that the output of the strain gauge could be converted into units of force. The strain gauges measured the normal and chord-wise forces induced on the airfoil by the free stream velocity of the MIWT. From the normal and chord-wise forces, the lift and drag forces can be determined. Figure 8 shows the relation of the lift and drag forces to

the normal and chord-wise forces. The lift and drag forces were calculated using the following equations:

$$Lift = N\cos(\alpha) - X\sin(\alpha) \quad \text{, and} \qquad [58]$$

$$Drag = N\sin(\alpha) + X\cos(\alpha) \quad , \qquad [59]$$

where N is the normal force, X is the chord-wise force and α is the angle of attack. The *Lift* and *Drag* forces in [58] and [59], can be described in their dimensionless forces; the coefficient of lift, C_l, and the coefficient of drag, C_d.

$$C_l = \frac{Lift}{\frac{1}{2}\rho_{air}U^2 A_p} \qquad [60]$$

$$C_d = \frac{Drag}{\frac{1}{2}\rho_{air}U^2 A_p} \qquad [61]$$

4.4 Standard Uncertainty Analysis

Uncertainty analysis is the estimation of error in a measurement or in a result, usually determined with a certain level of confidence (Wheeler et al. 2004). Uncertainty analysis is very important to any measurement system design in order to identify inaccuracies in measurements that affect the end result. The methods that were used to combine all sources of uncertainties for the velocity measurement and the data acquisition system are explained in the following section.

The propagation of uncertainties can be based by taking the data reduction equation. Consider that n amount of independent variables (x) measurements are made. The resultant, or dependent variable (y) is a function of the independent variables and a constant (C).

$$y = f(x_1, x_2, C, ..., x_n) \qquad [62]$$

Each measurement of the independent variables will have a certain degree, or amount, of uncertainty associated with it. This uncertainty (∂) corresponds to either precision uncertainty (imprecision of measurements) or a bias uncertainty (maximum fixed error). The Taylor method of uncertainty takes the partial derivative of the data reduction equation, [62], with respect to each independent variable:

$$\partial y = \partial x_1 \cdot \frac{\delta y}{\delta x_1} + \partial x_2 \cdot \frac{\delta y}{\delta x_2} + \partial C \cdot \frac{\delta y}{\delta C} + ... + \partial x_n \cdot \frac{\delta y}{\delta x_n} \qquad [63]$$

The uncertainty of the constant *(∂C)* would be zero, therefore [63] would be rewritten as:

$$\partial y = \partial x_1 \cdot \frac{\delta y}{\delta x_1} + \partial x_2 \cdot \frac{\delta y}{\delta x_2} + ... + \partial x_n \cdot \frac{\delta y}{\delta x_n} \qquad [64]$$

Each term in [64] will be forced positive by squaring each term, which will leave the general uncertainty equation:

$$\partial y^2 = \left(\partial x_1 \cdot \frac{\delta y}{\delta x_1} \right)^2 + \left(\partial x_2 \cdot \frac{\delta y}{\delta x_2} \right)^2 + ... + \left(\partial x_n \cdot \frac{\delta y}{\delta x_n} \right)^2 \qquad [65]$$

4.4.1 Velocity Measurement Uncertainty

When determining the free stream velocity (U) of the MIWT, recall that the free stream velocity [17], was composed of the pressure difference (ΔP), determined from the hydrostatic pressure [15], and the atmospheric density [18] as shown by the function below:

$$U = f(\Delta P, \rho_{air}) \qquad [66]$$

Recall that the dynamic pressure measurement was a function of the gauge oil density, the gravitational constant and the height of the manometer gauge fluid. Therefore, the dynamic pressure measurement can be described by the following function:

$$\Delta P = f(\rho_{gauge}, g, h) \qquad [67]$$

The air density within the MIWT test section was a function of the measured temperature, the measured corrected atmospheric pressure, the universal gas constant and the molecular weight of air. The air density can be described by the following function:

$$\rho_{air} = f(M, R_u, P_{atm}, T) \qquad [68]$$

The Taylor method of uncertainty was applied to [68] to determine the uncertainty in atmospheric air density result as shown in the following equation:

$$\partial\rho_{air}{}^2 = \left[\partial P_{atm}\frac{\delta\rho_{air}}{\delta P_{atm}}\right]^2 + \left[\partial R_u\frac{\delta\rho_{air}}{\delta R_u}\right]^2 + \left[\partial M\frac{\delta\rho_{air}}{\delta M}\right]^2 + \left[\partial T\frac{\delta\rho_{air}}{\delta T}\right]^2 \qquad [69]$$

The universal gas constant and the molecular weight of the air are considered to be constants, therefore [69] can be rewritten as:

$$\partial\rho_{air}{}^2 = \left[\partial P_{atm}\frac{\delta\rho_{air}}{\delta P_{atm}}\right]^2 + \left[\partial T\frac{\delta\rho_{air}}{\delta T}\right]^2 \qquad [70]$$

The partial derivatives of the air density with respect to the atmospheric pressure and temperature are shown in the following equations:

$$\frac{\delta\rho_{air}}{\delta P_{atm}} = \frac{1}{\frac{R_u}{M}T} \qquad [71]$$

$$\frac{\delta \rho_{air}}{\delta T} = \frac{-P_{atm}}{\frac{R_u}{M} T^2} \qquad [\,72\,]$$

Combining [70] with [71] and [72], gives the final uncertainty result for the density of air measurement. The uncertainty in the temperature and pressure measurements are 1° K and 0.25 kPa, respectively. These uncertainties are used in the following equation to find the uncertainty in the atmospheric air pressure measurement.

$$\partial \rho_{air}{}^2 = \left[\partial P_{atm} \left(\frac{1}{\frac{R_u}{M} T} \right) \right]^2 + \left[\partial T \left(\frac{-P_{atm}}{\frac{R_u}{M} T^2} \right) \right]^2 \qquad [\,73\,]$$

The effects of humidity on the atmospheric air density were neglected. Mease et al. (1992), noted that the effects of relative humidity in air density is minimal. The authors found at 90% relative humidity, the density of air changes by 1%.

Applying the Taylor method to [67] to determine the uncertainty in the dynamic pressure result renders the following equation:

$$(\partial \Delta P)^2 = \left[\partial \rho_{gauge} \cdot \frac{\delta \Delta P}{\delta \rho_{gauge}} \right]^2 + \left[\partial g \cdot \frac{\delta \Delta P}{\delta g} \right]^2 + \left[\partial h \cdot \frac{\delta \Delta P}{\delta h} \right]^2 \qquad [\,74\,]$$

The gauge fluid density term is considered to be constant, therefore, [74] can be rewritten if the following form:

$$(\partial \Delta P) = \left\| \left[\partial h \cdot \frac{\delta \Delta P}{\delta h} \right] \right\| \qquad [\,75\,]$$

Completing the partial derivative gives the final form of the uncertainty of the dynamic pressure. The uncertainty in the manometer reading (∂h) is 0.5 mm of gauge fluid, which was used in the following equation to determine the uncertainty of the dynamic pressure:

$$(\partial \Delta P) = \left\| \left[\partial h \cdot \frac{\delta \Delta P}{\delta h} \right] \right\| = \partial h \cdot \rho_{gauge} g \qquad [76]$$

The Taylor method is then applied to [66] to determine the resultant uncertainty in the free stream velocity result.

$$\partial U^2 = \left[\partial \Delta P \frac{\delta U}{\delta \Delta P} \right]^2 + \left[\partial \rho_{air} \frac{\delta U}{\delta \rho_{air}} \right]^2 \qquad [77]$$

The partial derivatives of the free stream velocity with respect to the dynamic pressure and atmospheric air density are shown in the following equations:

$$\frac{\delta U}{\delta \Delta P} = \sqrt{\frac{2}{\rho_{air}}} \left(\frac{1}{2\sqrt{\Delta P}} \right) \qquad [78]$$

$$\frac{\delta U}{\delta \rho_{air}} = \frac{-1}{2} \sqrt{2\Delta P} \left(\rho_{air}^{-3/2} \right) \qquad [79]$$

Combining [77] with [78] and [79], gives the final uncertainty result for the free stream velocity of the MIWT measurement.

$$\partial U^2 = \left[\partial \Delta P \left(\sqrt{\frac{2}{\rho}} \left(\frac{1}{2\sqrt{\Delta P}} \right) \right) \right]^2 + \left[\partial \rho_{air} \left(\frac{-1}{2} \sqrt{2\Delta P} \left(\rho^{-3/2} \right) \right) \right]^2 \qquad [80]$$

Recall from [73] and [76], the terms that would be inserted into [80] to determine the final uncertainty result for the free stream velocity of the MIWT.

4.4.2 Coefficient of Lift and Drag Uncertainty

To determine the uncertainty associated with the coefficient of lift and drag, the uncertainty in lift and drag also have to be calculated. The Taylor method of uncertainty was applied to [58] and [59] to determine the uncertainty in both lift and drag which resulted in the following equations:

$$(\partial Lift)^2 = [\partial N \cos\alpha]^2 + [\partial X \sin\alpha]^2 + [\partial\alpha(-N\sin\alpha - X\cos\alpha)]^2 \quad [81]$$

$$(\partial Drag)^2 = [\partial N \sin\alpha]^2 + [\partial X \cos\alpha]^2 + [\partial\alpha(N\cos\alpha - X\sin\alpha)]^2 \quad [82]$$

The uncertainty associated with the angle of attack (α) is 1° and the uncertainty in the normal and chord wise component of force measurements were both determined to be 5% from the accuracy of the data acquisition system.

The uncertainty of the coefficient of lift and drag can then be determined using the Taylor method and applying it to [60] and [61]. This renders the following equations:

$$(\partial C_l)^2 = \left[\partial Lift\left(\frac{1}{0.5\rho_{air}U^2A_p}\right)\right]^2 + \left[\partial\rho_{air}\left(\frac{-Lift}{0.5\rho_{air}^2U^2A_p}\right)\right]^2 + \left[\partial U\left(\frac{-2\cdot Lift}{0.5\rho_{air}^2U^3A_p}\right)\right]^2 + \left[\partial A_p\left(\frac{-Lift}{0.5\rho_{air}U^2A_p^2}\right)\right]^2 \quad [83]$$

$$(\partial C_d)^2 = \left[\partial Drag\left(\frac{1}{0.5\rho_{air}U^2A_p}\right)\right]^2 + \left[\partial\rho_{air}\left(\frac{-Drag}{0.5\rho_{air}^2U^2A_p}\right)\right]^2 + \left[\partial U\left(\frac{-2\cdot Drag}{0.5\rho_{air}^2U^3A_p}\right)\right]^2 + \left[\partial A_p\left(\frac{-Drag}{0.5\rho_{air}U^2A_p^2}\right)\right]^2 \quad [84]$$

The uncertainty associated with Lift and Drag were determined in [81] and [82], respectively. The uncertainty associated with the air density and the wind tunnel velocity were determined in [73] and [80], respectively. The planform area uncertainty is 1 mm^2.

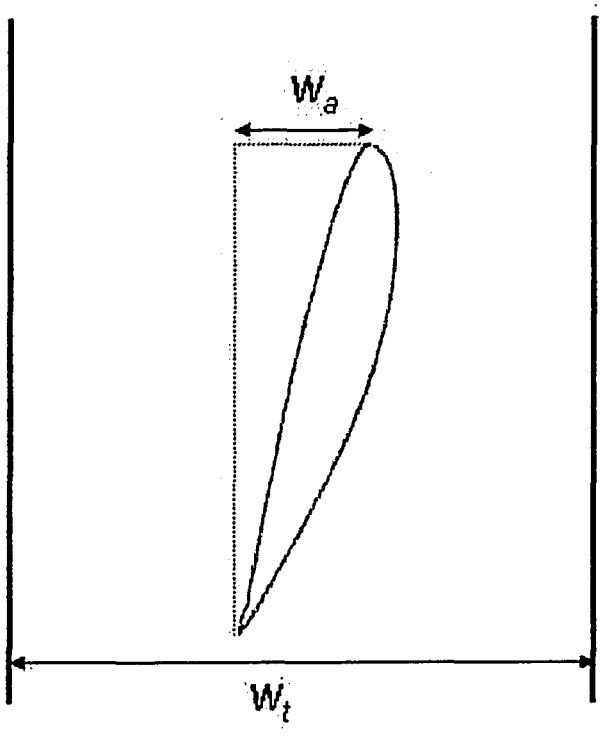

Figure 1: The projected frontal area of the airfoil to the wind tunnel. The dark lines on the side are the wind tunnel walls.

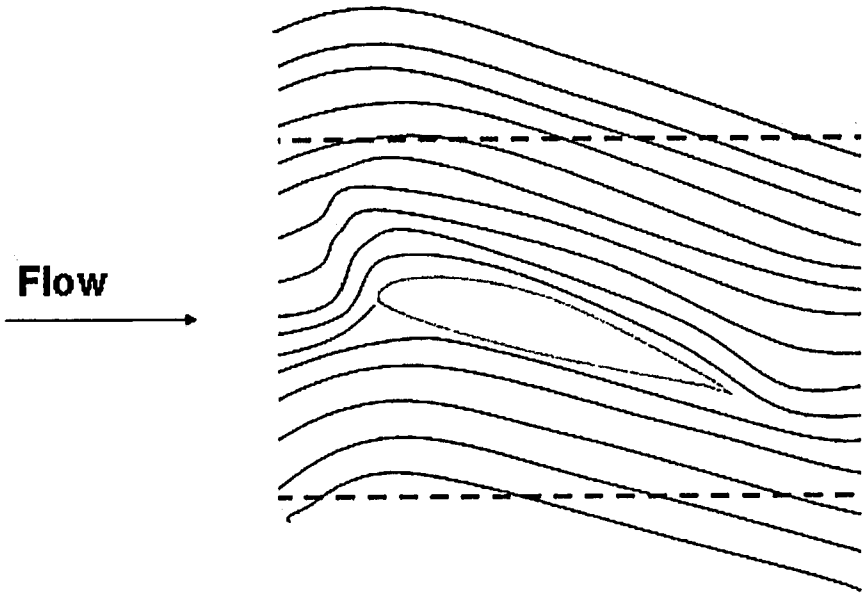

Figure 2: Wind tunnel wall effects. The dashed lines are the wind tunnel walls. The wall suppresses the lateral expansions of the streamlines.

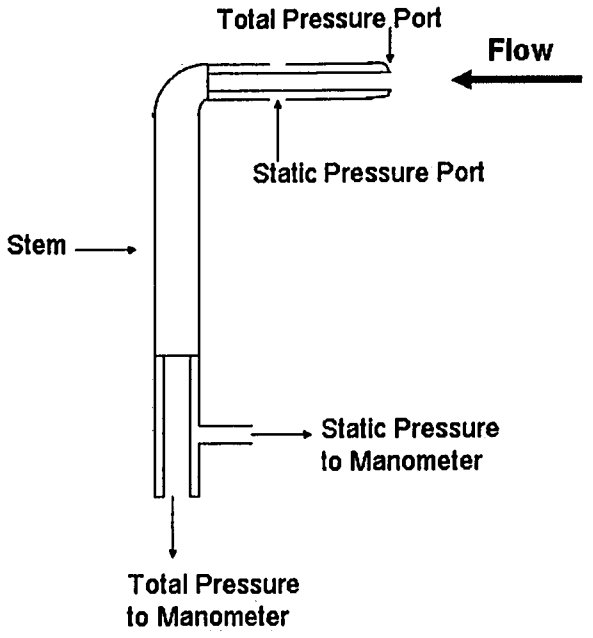

Figure 3: Pitot static tube. The Pitot tube that was used during the experiment was a Pitot static tube.

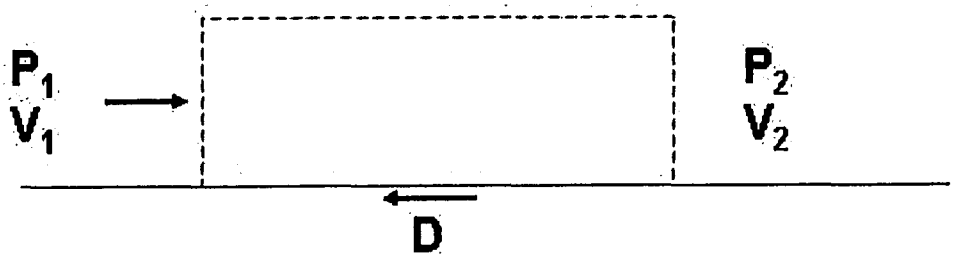

Figure 4: Free body diagram used to derive the boundary layer equation.

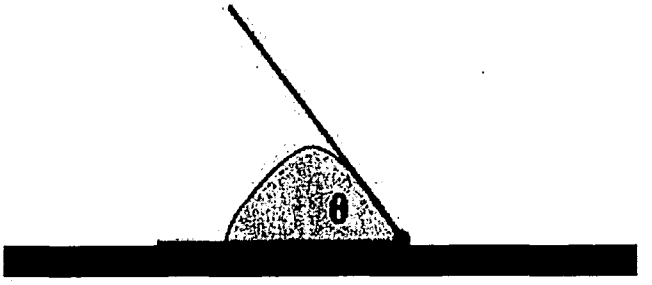

Figure 5: Contact angle measurement technique. The apex of the angle is formed at the three phase boundary. A line is drawn tangential to the liquid/gas barrier, and a reference arm is drawn tangential to the liquid/solid barrier.

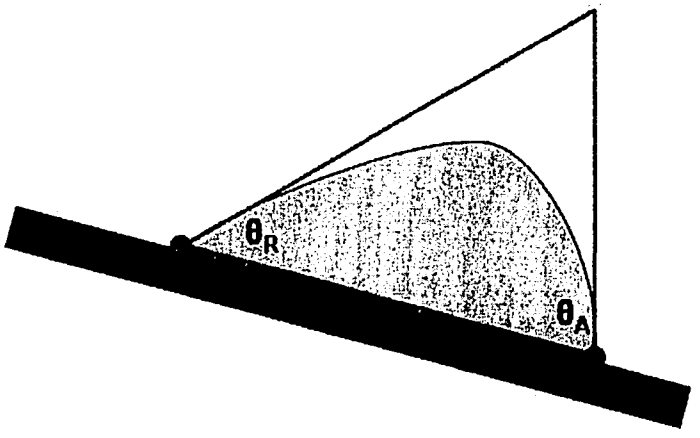

Figure 6: Tilting of the water bead to show the two characteristic contact angles; receded contact angle (θ_R), and the advanced contact angle (θ_A). A typical measured contact angle will fall in between these two characteristic angles.

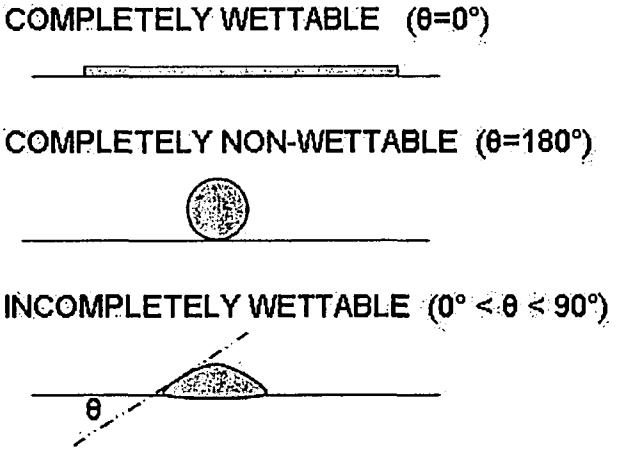

Figure 7: The relationship between surface wettability and the droplet-surface contact angle.

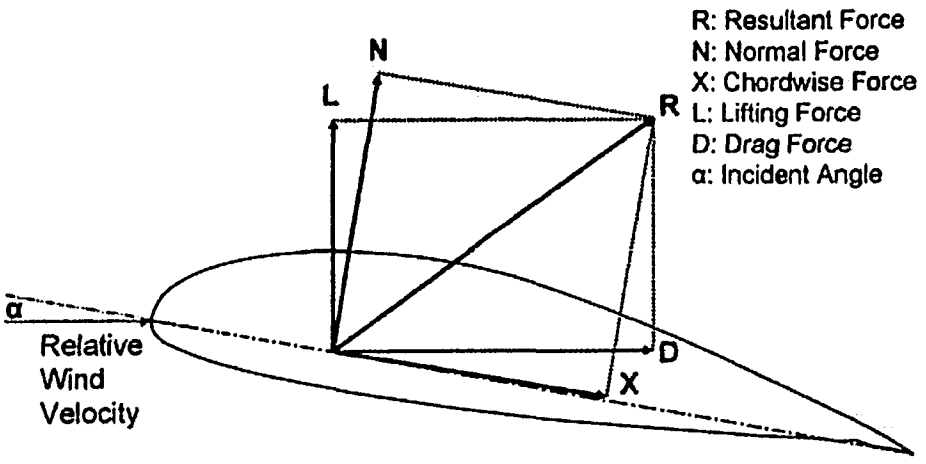

Figure 8: The components of force on the airfoil. The normal and chord-wise force are measured from the strain gauges. The lift and drag of the airfoil are the forces that are necessary to determine.

5.0 Experimental Set-Up

5.1 Wind Tunnel

The Marine Icing Wind Tunnel (MIWT) on the 5th floor of the Mechanical Engineering Building at the University of Alberta was originally designed and constructed by a M. Sc. candidate in 1988, Chris E. Foy, under the direct supervision of Dr. E.M. Gates and Dr. E.P. Lozowski. The MIWT also operates as a 2 phase low speed wind tunnel by allowing the injection of a uniform spray of droplets upstream of the test section.

5.1.1 Design

The MIWT is a vertical closed loop system constructed from stainless steel ductwork with a square cross-section, which varies in cross sectional area from 4 m^2 at the low speed regions to 1/4 m^2 at the test section. Turning vanes are located at each 90° corner to reduce the flow losses and recirculation effects of the airflow around the corners. The wind tunnel has a vertical height of 8 meters and a running length of 13 meters and has a local width and height ranging from 2 meters to 0.5 meters, respectively. Figure 9 illustrates the characteristics of the MIWT.

A spreader bar with nozzles attached is located in a low speed region before the 16:1 contraction to the test section of the wind tunnel. A settling chamber consisting of baffle plates is situated beyond the test section to separate the water from the 2 phase flow which is then ejected from the wind tunnel via a drainage pipe.

The air is then accelerated by a centrifugal axial flow fan where it passes through two 90° bends with an 8 meter rise in elevation, and then travels 13 meters before reaching the low speed region before the contraction to the test section. The flow direction is down (in the direction of gravity) through the test section.

5.1.2 Air Velocity Control and Measurement

After the water droplets are removed, the filtered air is then fed into a centrifugal axial flow fan which circulates the air through the wind tunnel. The centrifugal axial flow fan has an impeller diameter of 0.905 m which is belt driven by a variable speed 37 kW direct current motor. The velocity of the air circulating in the MIWT is controlled by two switches on the control panel which regulate the rotational velocity of the axial flow fan.

During the experiment, the air velocity was measured using a Pitot-static tube coupled with a Dwyer inclined manometer which had a resolution of 0.01 inch of gauge oil, which is equivalent to 2.0 Pa. The Pitot tube was inserted through a cut out section in the test section wall far enough from the wall to ensure that the wind velocity measurements were not taken within the boundary layer or in the partially developed flow regime. 2 meters of thin surgical tubing provided inertial dampening between the inclined manometer and the Pitot-static tube. The Dwyer inclined manometer used red gauge oil with a specific gravity of 0.826; its output was in inches of gauge oil. Calculations could then be performed to convert the pressure readings to velocity readings. At Reynolds numbers of 1.0×10^5 and 3.0×10^5; the resolution in terms of velocity was 0.2 m/s and 0.1 m/s, respectively. The Pitot tube

method of measuring velocity was used for the duration of the experiment due to the sensitivity of the experiment with respect to air velocity.

5.1.3 Test Section

The test section is constructed from 10 mm walled clear polycarbonate and has a 50 cm by 50 cm cross section with a vertical length of 80 cm. The airfoil is firmly attached to the side walls with fasteners that are built into the wall. There is also a mechanism built the walls that fasten the airfoil so that the angle of attack of the airfoil can be changed from -30° to +30° in 1° increments. Figure 10 shows the mechanism which allows the operator to vary the angle of attack while the airfoil is firmly attached. The two walls that are not used for fastening the airfoil have two removable windows in each wall as shown in Figure 11. These removable windows are used for accessing the airfoil as well as for span-wise viewing of the airfoil.

Immediately upstream of the test section is a 16:1 gradual contraction from the low velocity region.

5.1.4 Spray System

The MIWT originally used a brine injection system. After 15 years of intermittent use, many of the original components of the brine injection system were corroded. It was necessary to replace all the components of the MIWT with new components. A new building water injection system was designed and constructed in its place.

A 20 gallon hot water tank with a maximum allowable working pressure of 150 psi was used as a holding tank for the building water injection. The holding tank was pressurized using building compressed air supply to 60 psi, and regulated by a variable pressure regulator. Check valves were placed on the inlet compressed air and building water supply lines entering the holding tank. Plastic 1/4 inch tubing was used to supply the building compressed air supply to the inlet of the pressure regulator and from the pressure regulator to the holding tank. The building water was directly fed into the holding tank using 3/8 inch plastic tubing. The water in the holding tank was then left to settle for 3 days to ensure that the temperature of the water reached room temperature. Air pressure was then used to push the building water from the holding tank to the water injection control panel using 3/8 inch plastic tubing. Figure 12 shows the schematics of the building water injection system.

The pressurized building water is then routed into the lower flow manifold, which is located in the control panel. The lower manifold splits the inlet supply line into three lines. Each line has a Whitey valve to control and vary the injection rate which is displayed on the flow rate indicators. The three lines are then routed into the upper flow manifold where a single outlet leaves the control panel and supplies the spreader bar. A solenoid valve is located above the spreader bar to start or stop building water injection into the wind tunnel. In order to simulate heavy rainfall, Danfoss nozzles rated to 12.5 kg/hr were attached onto the spreader bar located in the low speed region of the wind tunnel before the contraction to the test section. The water is injected 2 meters above the test section with constant pressure to maintain the desired injection rate without perturbations in the flow. The average droplet size has

been determined from a previous experiment (Foy 1985) to be 90 ± 10 μm. The water spray was contained to a region of 20 cm by 20 cm in the test section by configuring the nozzles on the spreader bar.

5.1.5 Performance

The performance of the MIWT was determined by extensive tests using custom designed equipment. Five tests were conducted over several days and used the same detailed procedure to ensure that the variance between tests were minimized. The velocity profile of the test section was the main characteristic that was being determined during these tests. Determining the velocity profile of the MIWT is extremely important in this experiment as a constant distribution of airflow is necessary to simulate the effect of quiescent air being met by a moving airfoil.

The measurements were taken in a multi-step process using custom built equipment and equipment that was supplied by the Department of Mechanical Engineering. In order to measure the velocity profile a 36 tube rake (as seen in Figure 13) with equally spaced Pitot tubes along the rake was used. The Pitot tubes had an outer diameter of 1 mm and an inner diameter of 0.5 mm, and were spaced at a distance of 5 mm apart to ensure that flow characteristics that were being measured were not affected by closely packed Pitot tubes.

The Pitot tubes were connected to an inclined multi-tube manometer using several feet of surgical tubing to act as an inertial damper for ease of reading the manometer. The inclined multi-tube manometer was manufactured by Dwyer Instruments and used red manometer gauge oil with a specific gravity of 0.862. The

adjustable inclined multi-tube manometer was set to an angle of 35° off horizontal which resulted in a resolution of 0.23 m/s at a Reynolds number of 1.0×10^5 and a resolution of 0.08 m/s at a Reynolds number of 3.0×10^5.

A traversing mount was designed and constructed that enabled the Pitot tube array to move along the test section that would be occupied by the airfoil. The test section of the MIWT was divided into 8 regions that were individually measured by the Pitot tube array. The Pitot tube array samples were taken in two rows of 4 sections spaced 12.5 cm apart. Figure 14 shows the positioning of the Pitot tube array within the wind tunnel.

A hot wire anemometer was used to determine the centerline velocity of the wind tunnel during a test which was used as a baseline. The centerline wind speed was measured to be 6.5 m/s. The Pitot tube array was then mounted onto the traversing rig and velocity measurements were taken. The pressure measurements were recorded by hand from the inclined multi-tube manometer and converted into velocity. The resulting velocity measurements were then plotted on a 3 dimensional chart to display the velocity profile. Figure 15 shows the velocity profile of the wind tunnel.

The velocity profiles were rather non consistent throughout the wind tunnel. The step wise increases in the velocity profile seem systematic and may be attributed to a number of factors.

1) The resolution of the incline multi-tube manometer.
2) Some of the tubes in the 36 tube rake may have had foreign materials present in the tubes or some of the tubes may have been crimped.

3) The low speed region of the velocity profile may be due to air flow recirculation around the corner of the wind tunnel.

The average wind speed measured was 6.4 m/s.

5.2 Airfoil

5.2.1 Skin Design

The low Reynolds number high lift airfoil was designed by ARV Development Corporation. The custom designed airfoil coordinates were scaled for x values between 0 and 1. The airfoil coordinates are listed in Appendix A. The airfoil profile is shown in Figure 16.

The airfoil wingspan is 50 cm, which allows the airfoil to be fixed to both sides of the test section of the MIWT. The airfoil characteristics (as seen in Figure 17) of the ARV Development Corporation airfoil are shown in Table 1.

The airfoil coordinates were then entered into a 3D modeling program that would allow construction of the custom designed airfoil to proceed in the machine shop in the Department of Mechanical Engineering. The skin of the airfoil was constructed out of stainless steel using the Department of Mechanical Engineering's C&C Machine in the machine shop. The airfoil was hand polished until the surface was extremely smooth.

The airfoil skin is composed of three sections that span 500 mm. A span view of the airfoil is shown in Figure 18. A tool was manufactured in order to equally space the gap between the end sections and middle section. The gap between the end

plates and middle section is 1 mm. The middle section of the airfoil is 2.54 mm wide. Figure 19 shows the components of the airfoil skin.

5.2.2 Inner Airfoil Components

The cantilever section is constructed from a solid aluminum round bar with two machined smooth flat sections 90° out of phase with each other. The cantilever section is fixed to one of the end sections of the airfoil. The middle section of the airfoil is connected to the cantilever section which allows the middle section to 'float' between the two end sections. As air flows past the airfoil, the whole airfoil is subject to lift and drag forces, but only the middle section has the ability to move. This movement was small, under 0.1mm for this work, and thus had negligible effect on the overall flow over this apparatus. This movement of the middle section induces a strain on the cantilever beam. Based on the orientation of the cantilever beam to the middle section, the flat section near the end had a strain induced by the chord-wise force and the flat section in the middle of the cantilever had a strain induced by the normal force. Figure 20 shows the cantilevered section.

5.3 Instrumentation

There are several methods of measuring strain; the method used in this experiment was with a strain gauge. A strain gauge's electrical resistance varies in proportion to the amount of strain in the device. The type of strain gauge that was

used in this experiment was the bonded metallic strain gauge also known as a foil gauge.

The foil strain gauge consists of a metallic foil arranged in a grid pattern. The grid is bonded to a thin backing, called the carrier, which was attached directly to the airfoil's cantilever section. In this configuration, the strain that is induced on the airfoil's cantilever section is transferred directly to the strain gauge. The electrical resistance of the foil type strain gauge is directly proportional with the amount of strain induced on the strain gauge. The strain gauges were used to measure the strain induced by the normal and chord-wise forces on the flat sections of the airfoil's cantilever section. The properties of the strain gauges are shown in Table 2.

Four strain gauges were carefully mounted onto each flat surface of the test section, two on each side. The normal and chord-wise forces were measured by attaching four strain gauges (two on either side) of each flat surface as shown in Figure 21.

5.4 Data Acquisition System

During this experiment, there were three phases of data collection. In the first phase, the strain gauges were connected to a strain gauge meter to measure the induced normal and chord-wise strain. An oscilloscope was also used to measure the fluctuation frequency of the loads, which were assumed to be associated with the shedding frequency of the airfoil. A data acquisition system was developed for the second and third phase of the experiment. This data acquisition system enabled 100 samples per second to be taken in the second phase and 1000 samples per second to

be taken in the third phase. These data were recorded on the computer for more detailed analysis of the results.

5.4.1 First Phase of Data Collection

In the first phase of data collection, the strain gauge wires were connected directly to a Portable Strain Indicator Vishay Model P3500 in a full Wheatstone bridge configuration. A Tektronix 1012 Digital Oscilloscope was connected to the Portable Strain Indicator Vishay Model P3500 to measure the natural frequency. The strain and frequency measurements were recorded by hand. The accuracy of the Portable Strain Indicator Vishay Model P3500 is ± 0.5% up to ± 3 micro-strain with a resolution of ± 1 micro-strain. The power was supplied to the strain gauges by the Portable Strain Indicator Vishay Model P3500. Figure 22 illustrates the data collection system that was implemented.

The Portable Strain Indicator Vishay Model P3500 was extremely susceptible to external vibrations and noise.

5.4.2 Second and Third Phase of Data Collection

In order to increase the validity of the measurements, a second phase of data collection was implemented. A data acquisition system was developed. The data acquisition system consisted of 5 individual components: a Pentium III 450 MHz desktop computer with 512 Mb of RAM with Windows 2000 operating system; a signal conditioning unit that was developed by the electrical technician in the Department of Mechanical Engineering; a National Instrument SCB-68 Connector

Block; a National Instrument 6052E data acquisition card; and a program created using National Instrument Labview 7.0 to acquire and analyze the data. The data acquisition software was calibrated to record 100 samples a second. In order to perform Discrete Fourier Transforms to determine shedding frequencies that are above 50 Hz, a third phase of data collection was done. The data acquisition software was set to sample data at a rate of 1000 samples a second. Both the second and third phases used the same data acquisition system. A schematic drawing of the data acquisition system is shown in Figure 23.

5.4.2.1 Signal Conditioning Unit

An "in-house" strain gauge conditioner that was part of the data acquisition system is shown in Figure 24. The strain gauge conditioner takes the raw voltages from the strain gauges that are attached to the airfoils cantilever section. The wires of the strain gauges are connected to the strain gauge conditioner in a full Wheatstone bridge configuration which can then be balanced by the ten turn 75,000 Ω potentiometer. The gain for each output conditioned voltage can be set up to 2000. The strain gauge conditioner also has a power supply to supply the strain gauges on the airfoil's cantilevered section with a steady 5 volts.

5.4.2.2 Connector Block

The strain gauge conditioner's outputs for each strain (normal and chord-wise) are from a positive and negative terminal. The input for the data acquisition card is a 68 pin serial connection port. In order for the data acquisition card to interpret the

data, a connector block is used. The connector block used for this experiment was a National Instrument SCB 68 shielded I/O Connector Block. The terminal wires for each strain from the strain gauge conditioner are connected to the connector block in a differential configuration. The connector block then transmits the differential conditioned voltages to the data acquisition card via a shielded 68 pin serial connection cable.

5.4.2.3 Data Acquisition Card

The type of data acquisition card that was used for this experiment was National Instrument 6052E which was mounted onto a Pentium III computer chassis.

Table 3 shows the characteristics of the data acquisition card used.

The data acquisition card collected the conditioned signal from the connector block which was interpreted by the data acquisition software.

5.4.2.4 Data Acquisition Software

In order to interpret the input conditioned voltage from the data acquisition card, data acquisition software is necessary. For this experiment, National Instrument Labview 7.0 was used. The software is built on a graphical user interface (GUI) in which the framework of the program can be created using blocks. Figure 25 shows the block diagram created using National Instrument's Labview 7.0.

The block diagram is broken down into 11 components (A through K):

- A: Takes the input data from the data acquisition card. Scales the normal voltage to a 0-5 volts and the chord-wise scale from 0-1 volts. The sample rate is also changed in this block. For phase two, the sample rate was set to 100 samples/second and for phase three, the sample rate was set to 1000 samples/second.
- B: Separates the normal and chord-wise voltages in order to be analyzed separately.
- C: Displays the raw data on the Labview front panel.
- D: Analyses the raw voltage data and determines the frequency.
- E: Applies a scaling factor to the raw voltage data in the form $Y = mX + b$. The m and b variables were determined during calibration of the strain gauges.
- F: Saves the frequency of the raw voltage in a table.
- G: Saves the scaled voltage in a table.
- H: Combines the frequency and scaled voltage into one file.
- I: Combines the normal and chord-wise data into one file.
- J: Enables the data to be written into a file.
- K: Saves the file to a spreadsheet on the computer's hard drive.

The data was saved as a Microsoft Excel spreadsheet and a text file. More data analysis techniques could then be applied to the data in these files.

Table 1: Airfoil dimensions of the ARV Development Corporation designed low Reynolds number high lift airfoil.

Airfoil Dimensions		
Chord Length	200	mm
Thickness	37.2	mm
Camber	9.8	mm

Table 2: Strain gauge properties

Strain Gauge Properties	
Manufacturer	Vishay Micro-Measurements
Resistance	350 Ω ± 0.3 %
Gauge Factor	2.135 ± 0.5 %
Traverse Sensitivity	+ 0.6 ± 0.2 %
Gauge Type	Foil Gauges

Table 3: Data acquisition card properties

Data Acquisition Card Properties	
Manufacturer	National Instruments
Model	6052E
Resolution	16 bit
Maximum Sampling Rate	333 kS/s
Number of Channels	16 or 8 Differential

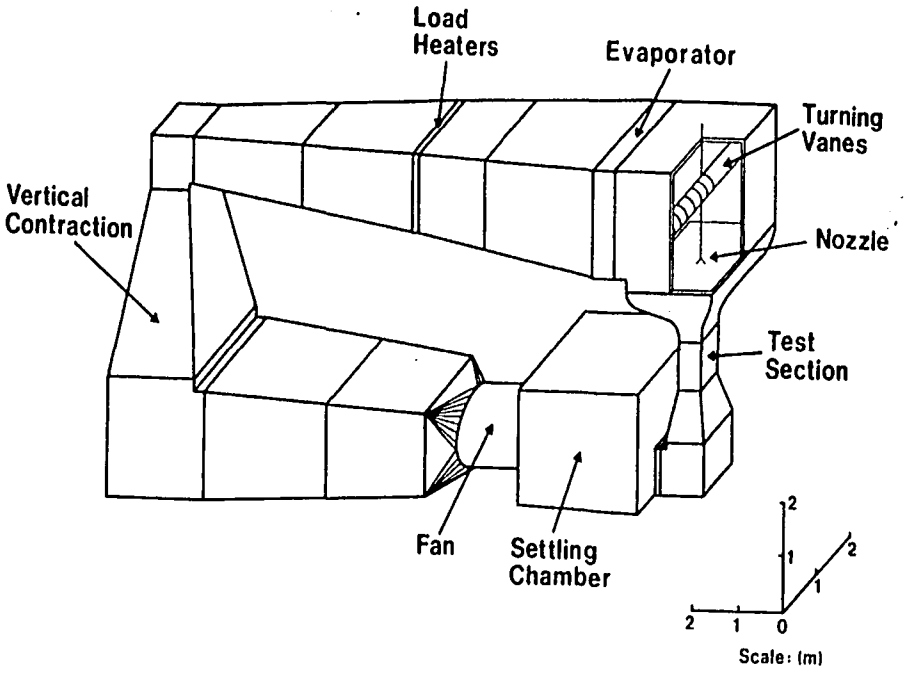

Figure 9: Oblique view of the MIWT. Located at the University of Alberta's Department of Mechanical Engineering. (Foy, 1988).

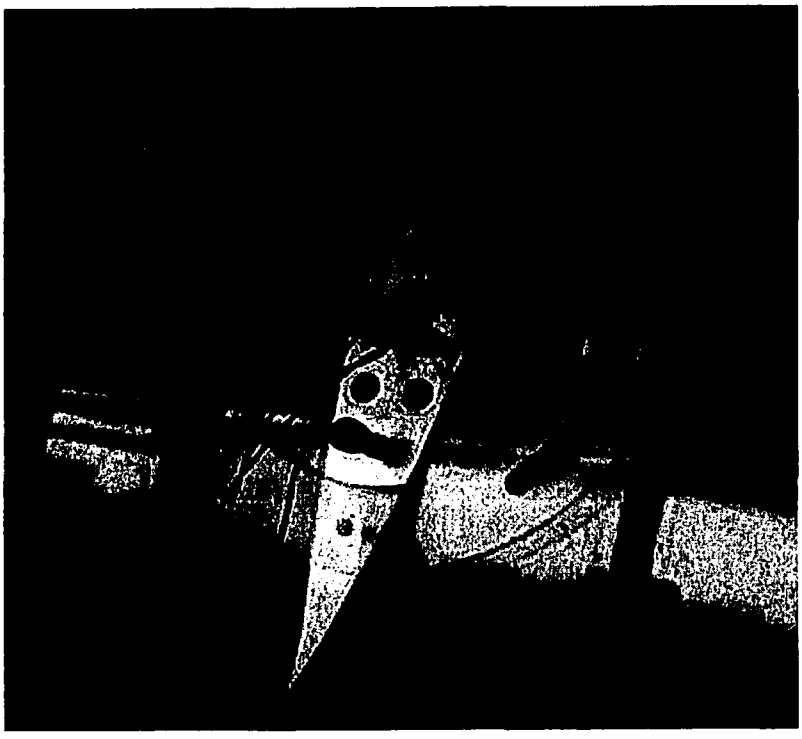

Figure 10: Attachment of the ARV Development Corporation custom designed airfoil to the side wall of the test section.

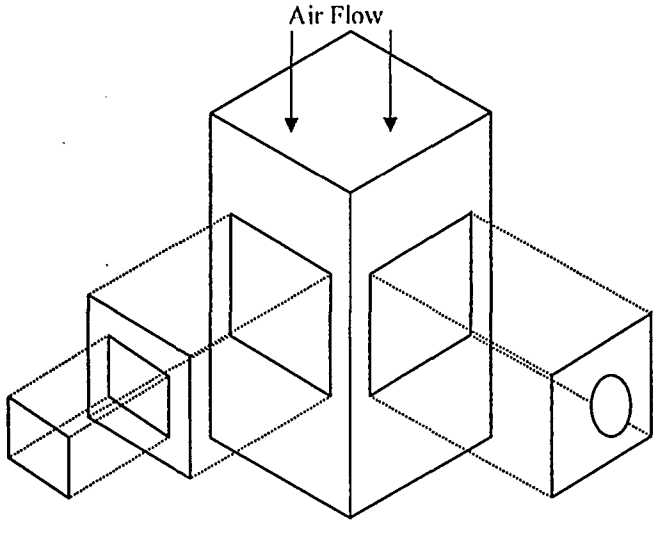

Figure 11: Components of the MIWT test section. This shows the removable windows where the contents of the test section can be accessed. The oval is the articulated mechanism which fastens the airfoil to the wall as well as allow the operator to change the angle of attack.

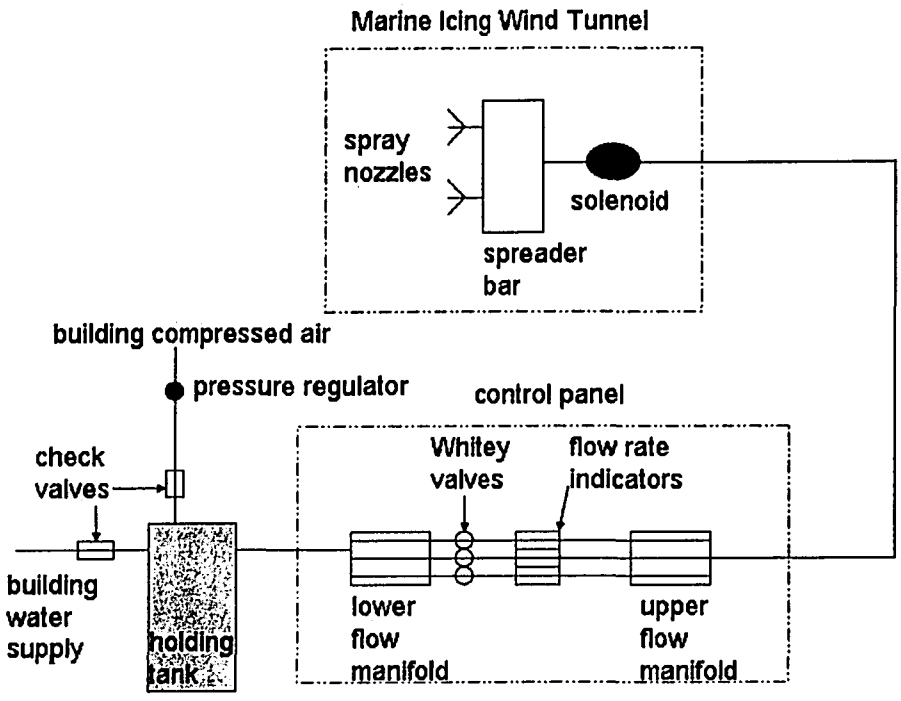

Figure 12: Single line drawing of the new building water injection system. The previous water injection system used brine water which corroded all the components over 15 years.

Figure 13: The rake of Pitot tubes that was used to determine the velocity profile of the MIWT. The 36 Pitot tubes are equally spaced at 5 mm apart.

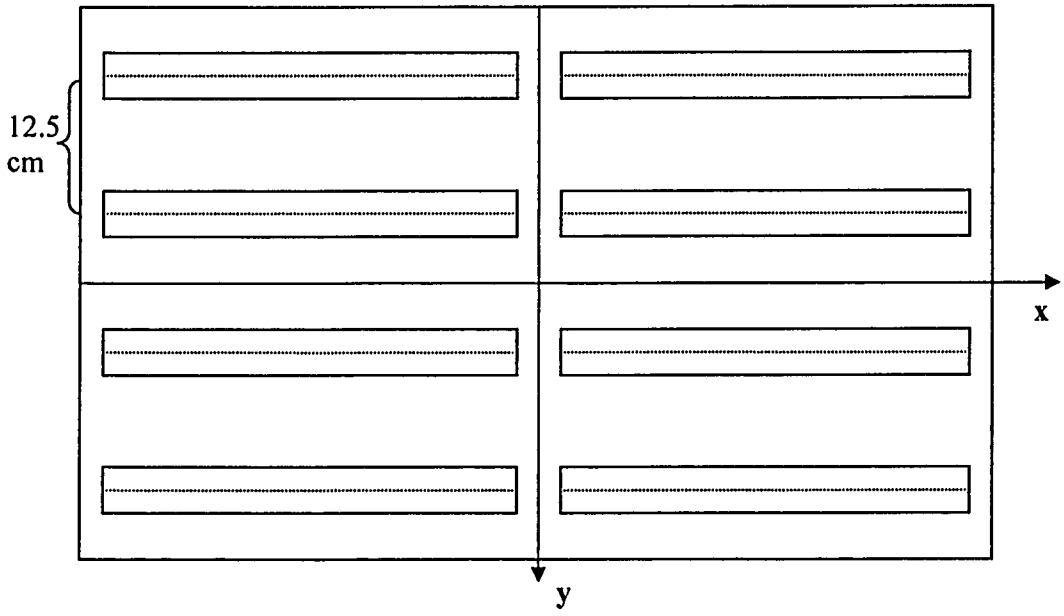

Figure 14: Pitot tube array positioning within the test section of the MIWT. The spacing is shown to be 12.5 cm between array samples in both the x and y position.

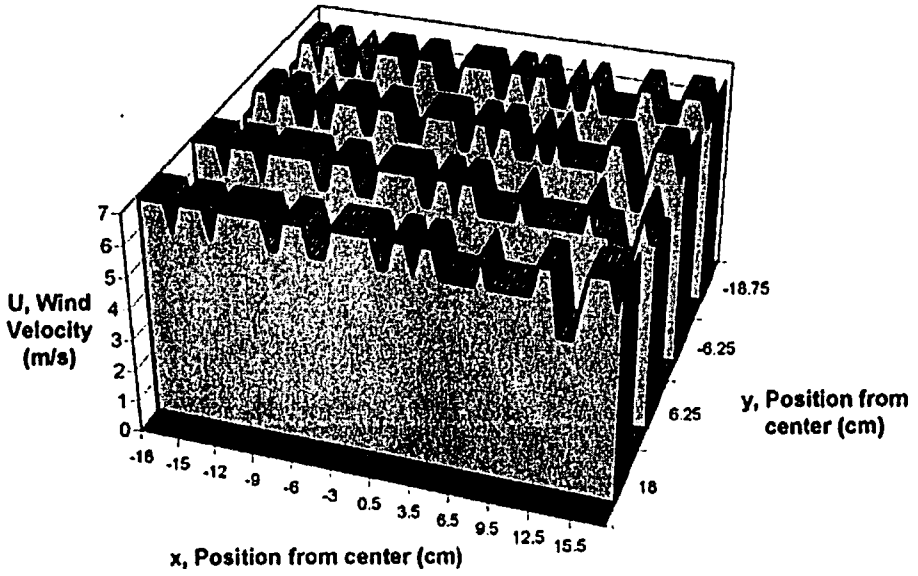

Figure 15: Velocity profile of the MIWT as measured by the custom traversing rig.

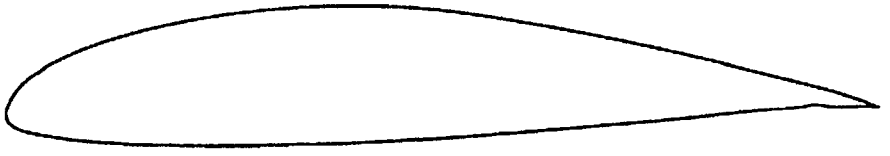

Figure 16: Chord-wise profile of the low Reynolds number high lift airfoil that was designed by ARV Development Corporation.

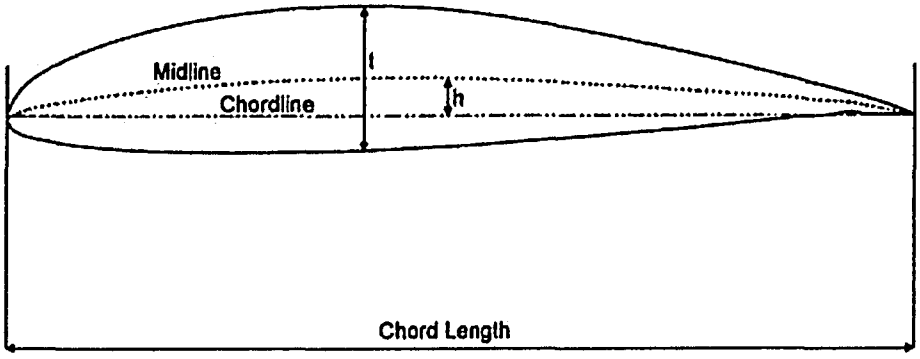

Figure 17: Chord-wise profile illustrating the airfoil characteristics of the low Reynolds number high lift airfoil.

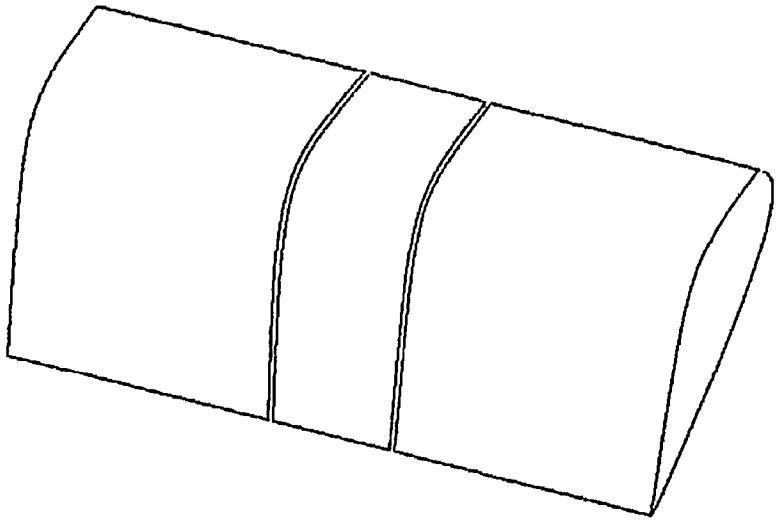

Figure 18: Span wise view of the airfoil. The middle section was allowed to move during experiments. A special tool was constructed in order to create an equally spaced gap in between the two end sections.

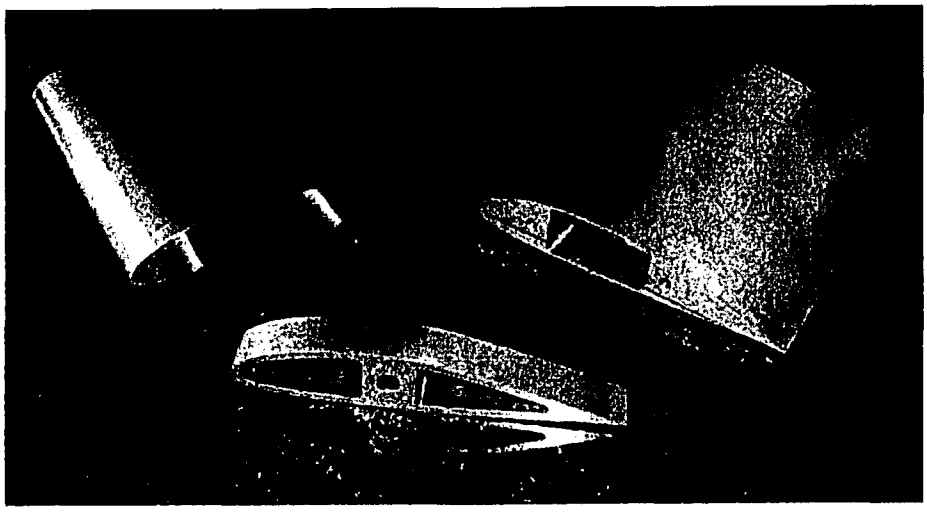

Figure 19: Components of the airfoil skin. The middle section (shown forward) is attached to the cantilevered section of the airfoil. The two end sections are solid stainless steel and are firmly attached to MIWT walls during experiments).

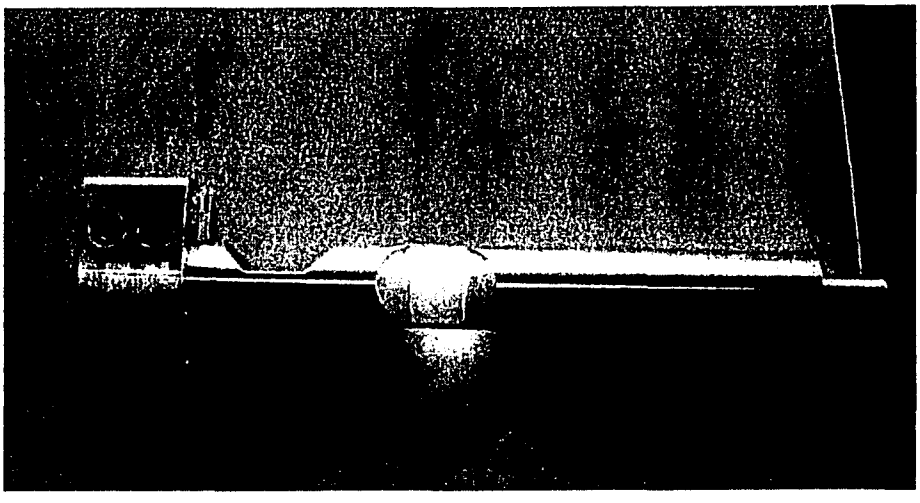

Figure 20: Cantilevered section of the airfoil. The cantilever is attached to a mounting bracket (pictured on the left side) which is then inserted into the end section of the airfoil (as seen in Figure 19 pictured on the right side). The middle section of the airfoil is aligned and attached to the opposing end (pictured on the right side). This allows the middle section to 'float' in between the two end sections.

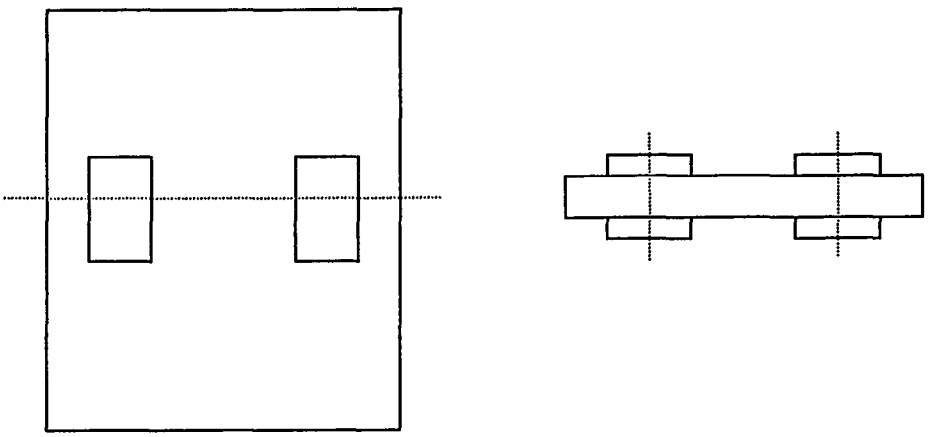

Figure 21: Strain gauge positioning on the airfoil's flat portion of the cantilever section. The strain gauges were carefully mounted onto the cantilever so that the horizontal and vertical axis for the strain gauges line up in order to be temperature and torsionally compensated. The input voltage required for the strain gauges is 5 volts.

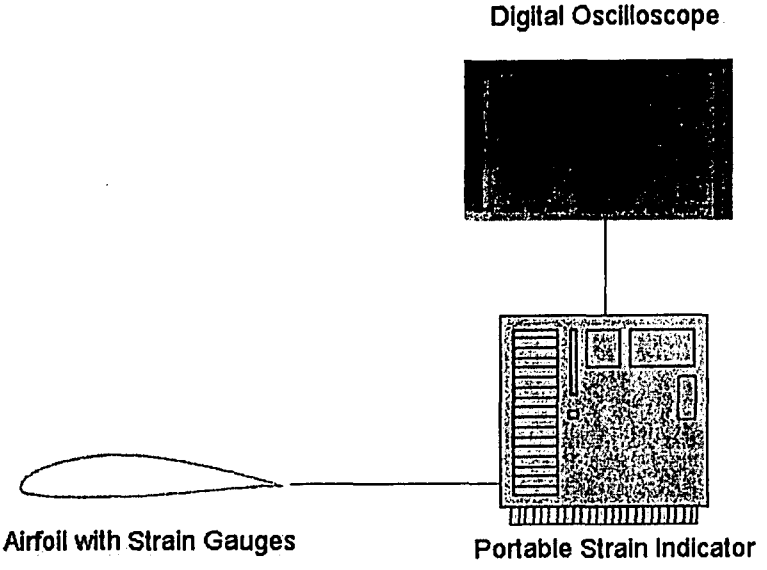

Figure 22: Experimental set-up for phase 1 data collection. The output voltages from the strain gauges are connected to the portable strain indicator in a full Wheatstone bridge configuration. The resultant strain is displayed on a digital LCD display. A digital oscilloscope is connected to the portable strain indicator to measure the shedding frequency of the airfoil.

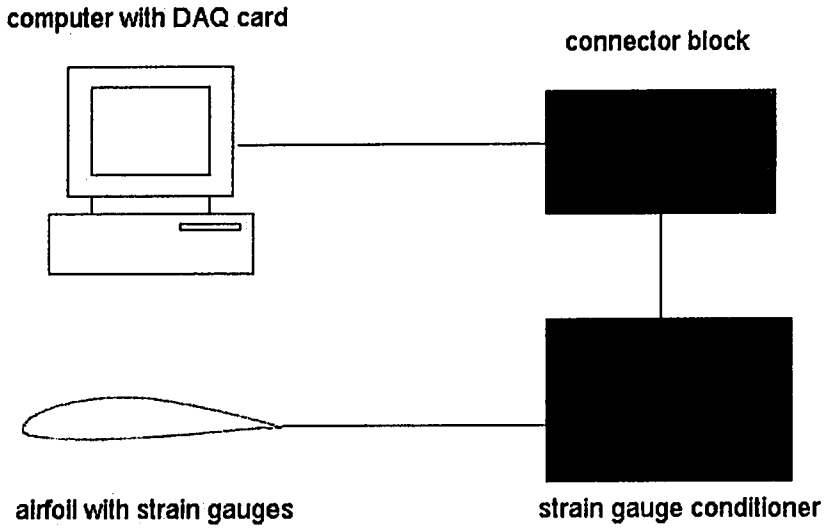

Figure 23: Data acquisition system schematic. The output voltages from the strain gauges are conditioned by the strain gauge conditioner. The SCB 68 connector then combines the conditioned signals into a format the data acquisition card can interpret.

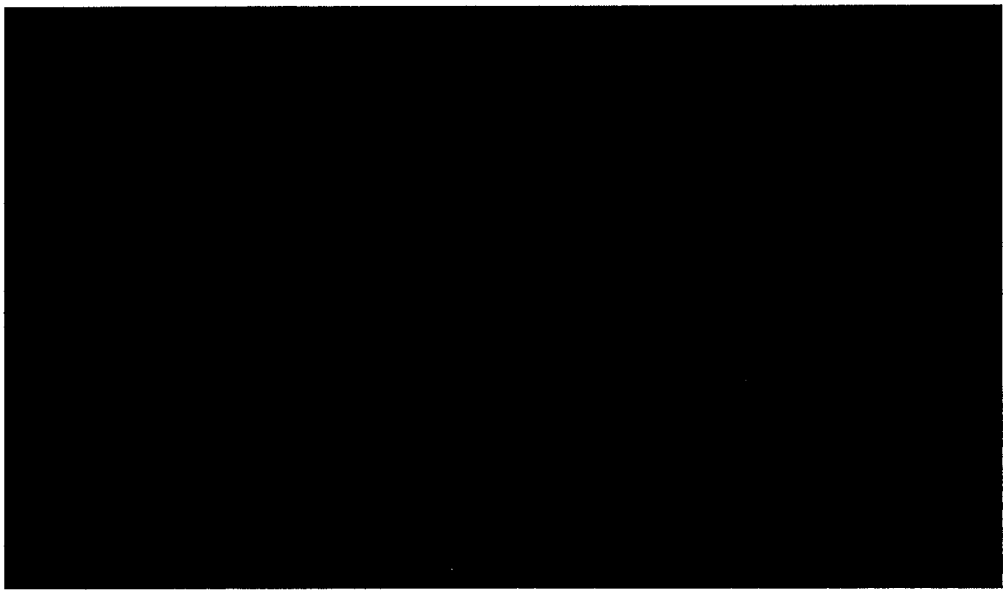

Figure 24: The stain gauge conditioner that was used to condition the raw voltages from the airfoil strain gauges. The full Wheatstone bridge configuration could be balanced by the ten turn 75,000 ohm potentiometer. The output conditioned voltages can be amplified by a gain of up to 2000.

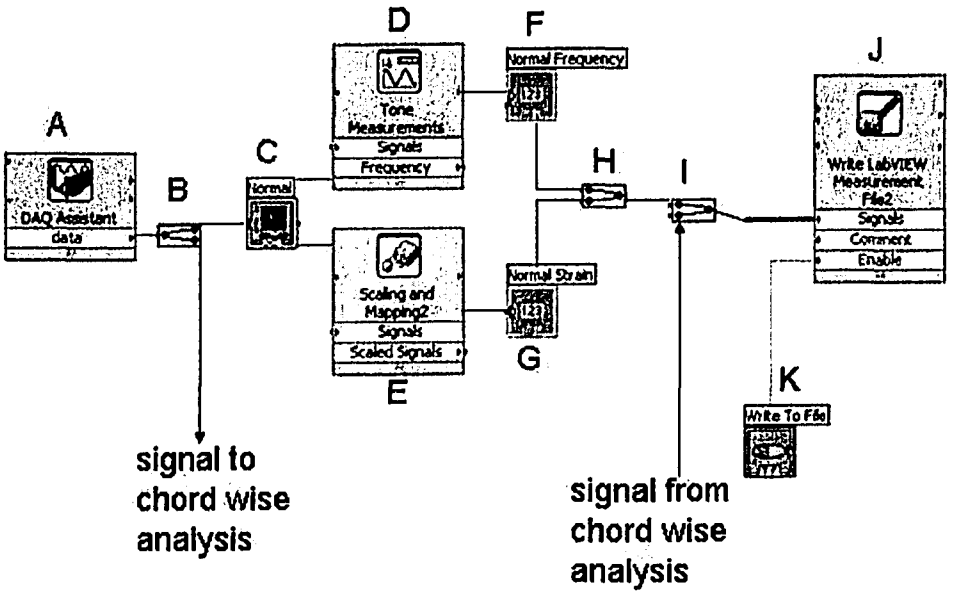

Figure 25: Schematic drawing of the block diagram created in Labview 7.0. Only the normal component of the data analysis is shown. The chord-wise analysis is a mirror image of the normal component.

6.0 Methodology

The following section deals with the experimental procedure followed during the test phase of the experiment. There were three phases of testing, all of which will be described in detail.

6.1 Phase 1

Phase 1 was completed using a Portable Strain Indicator Vishay Model P3500 which was coupled with a Tektronix TDS 1012 Digital Oscilloscope. Before the experiments were run and data were collected, calibration of the data collection system was necessary. Section 6.1.1 will discuss the calibration process and results of the portable strain indicator. After the calibration of the Portable Strain Indicator Vishay Model P3500, the airfoil was placed into the test section of the Marine Icing Wind Tunnel (MIWT), where it was mounted on the articulated mechanism (as shown in Figure 10) with four 2 inch bolts. The water injection spreader bar was placed in the low speed region of the wind tunnel during these tests, thus, any effects the water injection system imposes on the experimental data were present in all tests as noted by Marchman et al. (1987). The motor of the centrifugal axial blower fan was turned on and was warmed up for a period of 5 minutes. After the motor was warmed up, the power on the control panel which enabled the motor to be operated remotely from the control panel was switched on. The MIWT airflow was then set to a speed of 15 ± 5 m/s as indicated on the analog output of the control panel for a

period of 10 minutes. This would ensure that no foreign material would be present in the system that could potentially damage the airfoil.

In order to determine the velocity of air flow in the MIWT, the operating pressure was measured using a Pitot tube coupled with a Dwyer Inclined Manometer. A chart relating the Reynolds number to the MIWT air velocity to the operating pressure reading on the Dwyer Inclined Manometer was placed on the control panel. A copy of this chart can be found in Appendix G.

A test matrix of the data points necessary is shown in Table 4.

The parameters that were changed in Phase 1 of testing were the angle of attack and the Reynolds number. The angle of attack of the airfoil was set using the articulated mechanism and the airfoil was locked into place. The MIWT air velocity was then brought to the proper Reynolds number set point as specified in the test matrix. The induced strain from the lift and drag were manually recorded from the portable strain indicator's digital LCD. A Tektronix TDS 1012 Digital Oscilloscope was connected to the portable strain indicator where the shedding frequency was manually recorded as well. The MIWT air velocity was then brought to the other corresponding Reynolds number and the induced strain was manually recorded. After the three data points were taken for the angle of attack, the articulated mechanism was then unlocked and the airfoil was set to the next desired angle of attack. After each angle of attack was set, a non-zero strain reading was displayed on the portable strain indicator LCD display. The portable strain indictor LCD display was adjusted to read zero using the shunt resistor built into the portable strain indicator. The data

collection procedure was then repeated for each Reynolds number, and each angle of attack until the test matrix was completed.

Two trials were taken; if a data point from the second trial was more than 10% off the first, then a third trial for that data point was taken. The mean of the three trials was recorded as that data point. There were 27 data points recorded for Phase 1 of the experiment, which were grouped into three categories based on the Reynolds numbers.

6.1.1 Calibration of the Portable Strain Indicator Vishay Model P3500

The Portable Strain Indicator Vishay Model P3500 was calibrated after the strain gauges wires were attached to the strain indicator, and the proper settings gauge factor and bridge configuration were chosen. Calibration was done by hanging calibration weights from a nylon thread that was wrapped around the middle section of the airfoil. Table 5 shows the resultant induced strains when known forces were applied to the airfoil.

A relationship between the induced strain and the applied force was determined from Figure 26. The strain readings from the portable strain indicator were then converted to force using the linear relationship between the induced strain and the force determined from the calibration curve.

6.2 Phase 2 and Phase 3

The following section will discuss the test procedure for both Phase 2 and Phase 3. The same test procedure was followed for both phases; however, the test matrix of data points was different.

6.2.1 Phase 2 Test Matrix

The test matrix that was used for the second phase of experiments is shown in Table 6.

The test matrix was followed from the left column to the right column. The first test in the test sequence would be an airfoil with clean surface, in dry conditions, with a 0° angle of attack at a Reynolds number of 1.0×10^5. The second test would change the Reynolds number to 1.5×10^5. The Reynolds number set point would increase in each subsequent test until the last Reynolds number set point was reached. After that, the angle of attack was increased to the next set point and the Reynolds number sequence would be repeated. When all the angle of attack set points were fulfilled, the water injection system was then engaged and the test sequence was repeated. Two trials were taken; if a data point from the second trial was more than 10% off the first, then a third trial for that data point was taken. The mean of the three trials was recorded as that data point. The dry and wet testing procedure that was followed will be discussed in Section 6.2.3.1 and Section 6.2.3.3, respectively.

After the data points were recorded for the dry and wet test for the clean airfoil surface, the next surface coating would be applied on the airfoil. The procedure that was followed when coating the airfoil with a compound to change the

airfoil surface condition is described in Section 6.4. The same aforementioned sequence for each airfoil surface coating was followed.

There was a total of 270 data points recorded in the second phase of testing.

6.2.2 Phase 3 Test Matrix

The test matrix that was used for the third phase of experiments is shown in Table 7.

The phase 3 test matrix follows the same test sequence as the phase 2 test sequence with the exception that only one Reynolds number was tested. There was a total of 54 data points recorded in the third phase of testing.

6.2.3 Test Procedure

Phase 2 and 3 testing used a data acquisition system as described in Section 5.4.2. Before the experiments were run and data was collected, calibration of the data acquisition system was necessary. Section 6.2.4 will discuss the calibration process and results of the data acquisition system. The calibration results of the data acquisition system were used for both Phase 2 and 3 of the experiments.

6.2.3.1 Dry Test Procedure

The dry test procedure for the second and third phase of testing follows the same steps as noted in Section 6.1, with the exception that the data acquisition system was used to measure the induced strain as opposed to the portable strain indicators.

6.2.3.3 Wet Test Procedure

In order to simulate rainfall, the water injection system was enabled by the following steps:

1. The 20 gallon water tank was filled using the building water supply line and left to settle for a couple days to ensure the water reached room temperature.
2. The building compressed air supply was turned on.
3. The air regulator on the control panel was adjusted to 60 psi.
4. The flow rate indicators were 100% opened.
5. The solenoid valve above the spreader bar was switched to the on position from the control valve.
6. The water was run for a settling period of approximately 30 minutes for each airfoil surface condition to ensure a stable film thickness and to guarantee that no air pockets were in the water injection lines. Any air pockets in the water injection line would cause surging of the simulated rain that would affect the readings due to a change in droplet momentum. When there was an absence of air bubbles in the flow rate indicators, the water injection system was deemed ready to begin to test sequence.

After the water injection system was ready and the water film was stable the same procedure as set in the dry test procedure as described in Section 6.2.3.1 was followed.

6.2.4 Calibration of the Data Acquisition System

After the data acquisition system was physically set up, two variables had to be determined to input into the data acquisition system; the gain selection for chord-wise and normal force, and the scaling factor to convert raw voltage to applied force. Calibration weights were used to add a known force onto the airfoil by hanging the weights from a nylon thread. The gain settings were chosen so that the output voltage would be approximately 5 volts when a 2.5 kg weight was hung from the airfoil in the normal force orientation, and 2 volts when a 500 gram weight was hung from the airfoil in the chord-wise volts orientation. A nylon string was placed around the middle section of the airfoil and calibration weights were hung to determine the relationship between force applied and voltage.

Table 8 shows the calibration procedure to determine the scaling factor for the force applied in the normal direction; for each run, the data was taken for 10 seconds at a sampling rate of 100 samples/second. Table 9 shows the calibration procedure for the force applied in the chord-wise direction, which was taken over 10 seconds for each run at a sampling rate of 100 samples/second.

The calibration curves of the data acquisition system for the normal and chord-wise components of force are shown in Figure 27 and Figure 28, respectively. The calibration curve for both cases is linear with an R^2 value of 1.0. This shows exceptional agreement between the linear regression equation and the data points. The equations of the lines were then entered into the data acquisition software to relate the raw voltage input to an applied normal and chord-wise force.

Table 10 is a summary of the results from the calibration of the data acquisition system. The gain settings were applied to the signal conditioner. The output voltage, and scaling factors (*m and b*) were entered into the data acquisition system software.

6.3 Measurement Techniques

6.3.1 Liquid Content of Water

The water injection rate was kept constant to minimize surging, therefore a uniform liquid content of water could not be maintained as the cross section of the plume of droplets would decrease as the wind tunnel air flow velocity increased. In order to determine the liquid content of the water within the droplet laden cross flow, the diameter of the plume of droplets at the location of the airfoil was determined. In order to determine this spray diameter, a marker sheet was placed immediately upstream of the airfoil, which then would be wetted by the droplet laden cross flow. The marker paper was removed and the spray diameter was measured. This process was repeated five times for each Reynolds number set point in which the mean spray diameter was recorded. The mean spray diameter was used to determine the cross sectional area of the spray for Equation [20].

6.3.2 Contact Angle Measurements

A procedure was developed to ensure that a consistent contact angle was measured. The type of contact angle that was measured was the 'advanced contact

angle' as defined in Section 4: Theory. The airfoil was taken out of the MIWT test section during the contact angle measurement. A water droplet with a volume of 2 mL was placed on the airfoil using a 50 mL water filled syringe which produced single droplets of 1 mL. An initial water droplet was placed on the airfoil, then a second water droplet was carefully added to the existing water droplet. The airfoil was then tilted by 6° to give the water bead an advanced and receded contact angle. A photograph of the water bead on the airfoil was taken by a Nikon D70 digital camera with a resolution of 3008 x 2000 pixels with a black and white setting and no flash. The camera was placed on a tripod which was tilted at 5° to add perspective to the water drop. A print of the photograph was used to determine the advanced contact angle of the water drop. The advanced contact angle was used as the definition of the contact angle for the experiment.

6.4 Coating Application

The three airfoil surface conditions that were tested during the experiment were: a clean airfoil surface with no coatings applied, a surface with hydrophilic coating, and a surface with a hydrophobic coating. The following section discusses how the surface conditions were prepared.

6.4.1 Clean Airfoil

The airfoil was thoroughly and carefully cleaned using pure acetone everyday before testing to clean the particulate matter off the airfoil. After the tests which

required coating were finished, the airfoil was cleaned with acetone again to remove any coating residue.

6.4.2 Hydrophilic Coating

The hydrophilic compound that was applied to the airfoil was Rain-X. Rain-X is a commercially available coating that is used on car windshields to increase driver visibility during rain. The compound was applied in three coatings to ensure the airfoil was properly coated. The first coating was simply to pour the compound on a rag and liberally apply the compound on the airfoil. The compound was left to dry for 2 hours, then was wiped with a micro-fiber rag. This process was repeated for the next two coatings.

6.4.3 Hydrophobic Coating

The hydrophobic compound that was applied to the airfoil surface was Vaseline White Petroleum Jelly U.S.P. The compound was applied to the airfoil surface using a wide nozzle pressurized spray gun. The hydrophobic compound was applied in two light coatings so as not to drastically change the airfoil characteristics. From a visual inspection, the hydrophobic coating seemed to be uniform.

Table 4: Test matrix for phase 1 testing. There was a total of 27 data points recorded in the first phase.

Surface Coating	Condition	Angle of Attack	Reynolds Number
Clean	Dry	0	150000
		2	200000
		4	250000
		6	
		8	
		10	
		12	
		14	
		16	

Table 5: Calibration of the Portable Strain Indicator Vishay Model P3500.

Force Applied (N)	Induced Strain (micro-strain)
0.10	5
0.20	9
0.49	19
0.98	33
1.96	65
4.91	160
9.81	340

Table 6: Test matrix for phase 2 testing. There was a total of 270 data points recorded in the second phase.

Surface Coating	Condition	Angle of Attack	Reynolds Number
Clean	Dry	0	100000
Hydrophilic	Wet	2	150000
Hydrophobic		4	200000
		6	250000
		8	300000
		10	
		12	
		14	
		16	

Table 7: Test matrix for phase 3 testing. There was a total of 54 data points recorded in the third phase.

Surface Coating	Condition	Angle of Attack	Reynolds Number
Clean	Dry	0	300000
Hydrophilic	Wet	2	
Hydrophobic		4	
		6	
		8	
		10	
		12	
		14	
		16	

Table 8: Calibration procedure of the data acquisition system for measurement of the normal component of force. Each test run was sampled at a rate of 100 samples/second for a total of 1000 samples.

Test Run	Mass (grams)
1	0
2	50
3	100
4	200
5	300
6	400
7	500

Table 9: Calibration procedure of the data acquisition system for measurement of the chord-wise component of force. Each test run was sampled at a rate of 100 samples/second for a total of 1000 samples.

Test Run	Mass (grams)
1	0
2	50
3	70
4	100
5	150
6	200

Table 10: Variables determined from the calibration of the data acquisition system.

Force Component	Normal	Chord-wise
Output Voltage	0 - 5	0 - 1
Gain Setting	900	1600
m	5.1558	2.237
b	0	0

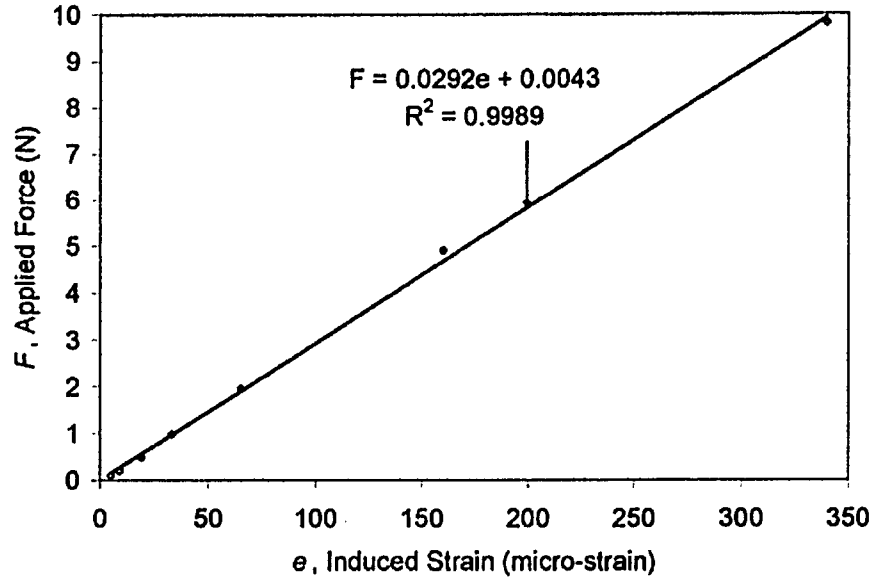

Figure 26: Calibration results from the Portable Strain Indicator Vishay Model P3500.

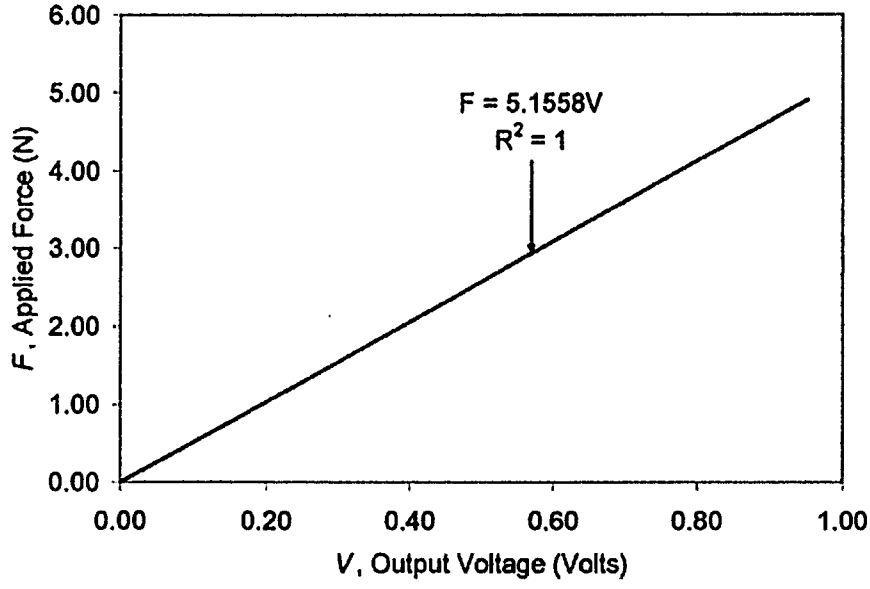

Figure 27: The scaling factor to convert the raw voltage to an induced normal force as determined from the calibration of the data acquisition system.

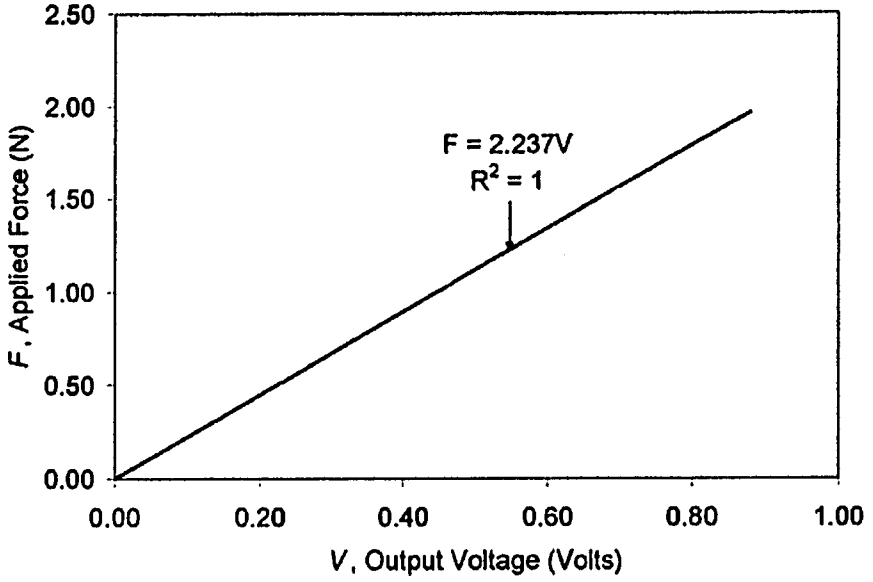

Figure 28: The scaling factor to convert the raw voltage to an induced chord-wise force as determined from the calibration of the data acquisition system.

7.0 Experimental Results

The naturally laminar flow airfoil test was completed in the Marine Icing Wind Tunnel (MIWT) over a range of Reynolds numbers spanning from 1.0×10^5 to 3.0×10^5. A water injection system was used to simulate rainfall to determine the effects of rain on the coefficient of lift and drag for the airfoil. After the airfoil was tested in the dry and wet MIWT conditions, two distinct coatings that caused the airfoil surface to have either hydrophobic or hydrophilic properties were applied. The droplet surface interaction effects on the lift and drag of the airfoil were analyzed on the hydrophobic and hydrophilic surface coatings. The coating that was used for the hydrophobic case was Vaseline Petroleum Jelly U.S.P., which is commercially available. The hydrophilic coating that was applied was Rain-X, a commercially available compound that is used on windshields to aid in visibility in rain.

7.1 Effects of Reynolds Number

The effects of increasing the Reynolds number on the coefficient of lift (C_l) and the coefficient of drag (C_d) on a clean airfoil surface in dry conditions are shown in Figure 29 and Figure 30.

In both the C_l and C_d curves, a wave type behavior at the lower Reynolds number is seen until a Reynolds number of 2.0×10^5 is reached. This behavior may be attributed to fluctuations in the MIWT motor power at low outputs. These fluctuations in the motor power may have caused perturbations in the free stream

velocity which would be detrimental in determining the lift and drag. For the rest of the study, all figures will be at a Reynolds number of 3.0×10^5.

7.2 *Contact Angle and Surface Wettability*

Compounds were applied to the airfoil skin to make the surface of the airfoil either hydrophobic or hydrophilic. The airfoil skin was also cleaned thoroughly to provide a baseline for the other two surfaces. Water droplets were placed on the three airfoil surfaces to determine the contact angle (θ) between the droplet and the surface of the airfoil.

The interaction between the droplet and the clean airfoil surface can be seen in Figure 31. The contact angle for the clean airfoil surface was determined to be $60 \pm 1°$.

A photograph of the water drop on the hydrophilic airfoil surface, which was used to determine the contact angle, is shown in Figure 32. The contact angle for the hydrophilic surface was determined to be $22 \pm 1°$.

The contact angle for the hydrophobic surface was determined by a photograph of the droplet surface interaction, as shown in Figure 33. The contact angle for the hydrophobic surface was measured to be $90 \pm 1°$.

7.3 *Comparison of Experimental Results to Theoretical Results*

The experimental results from the MIWT testing were compared with some initial potential flow estimates for the coefficient of lift and drag. The theoretical

values were computed using the software program PANDA (Program for Analysis and Design of Airfoils), which was developed by Desktop Aeronautics. PANDA takes in input text file of the airfoil dimensions and calculates the inviscid pressure distribution using a method of superposition of sources and vortices to determine the velocities where the pressure coefficient (C_p) is then calculated from the Bernoulli relation:

$$C_p = 1 - \frac{U^2}{U_\infty^2} \qquad [85]$$

The C_p values are calculated using this method over a range of angles of attack from 0° to 16°.

7.3.1 Coefficient of Lift

From the inviscid pressure distribution, the coefficient of lift is calculated by integrating the upper and lower pressure coefficients, $C_{P_{upper}}$ and $C_{P_{lower}}$, respectively, from the leading edge (*LE*) to the trailing edge (*TE*).

$$C_l = \frac{1}{c_{ref}} \int_{LE}^{TE} (C_{P_{lower}} - C_{P_{upper}}) dx \qquad [86]$$

The results of the C_l curves for the three airfoil surfaces in dry conditions compared to the theoretical C_l curve as computed by PANDA are shown in Figure 34.

From the graph, it appears as though there are three regions of angles of attack where the C_l have distinct characteristics: 0° - 6°, 6° - 10°, and angles of attack greater than 10°.

In the first region ($0° < \alpha < 6°$), the C_l curve for the clean airfoil is within 16.5% of the theoretical C_l curve in this region. The hydrophilic and hydrophobic coated airfoils C_l curves are within 7.2% and 14.2%, respectively, of the theoretical value of the C_l through this region. Within the first region, the difference between the C_l curves for the hydrophilic coated airfoil and the clean surface airfoil is within 11.8%, whereas the difference between the C_l curves for hydrophobic coated airfoil to the clean surface airfoil is 9.9%.

The second region ($6° < \alpha < 10°$), the C_l curves for all three surface conditions are within 8.8% of the theoretical C_l curve. The C_l curves for the hydrophilic and hydrophobic coated airfoils are within 7.1% and 7.0%, respectively, of the C_l curve for the clean surface airfoil condition.

In the third region of angles of attack ($\alpha > 10°$), the hydrophilic coated airfoil has a greater C_l than the clean surface airfoil by 6.7%, whereas the hydrophobic coated airfoil has a lower C_l than the clean surface airfoil by 8.5%.

7.3.2 Coefficient of Drag

The theoretical coefficient of drag is calculated by PANDA by determining the boundary layer conditions by using "so-called integral methods" (Kroo, PANDA User Guide); the total drag is then computed using the Squire-Young formula. The C_d curves for three airfoil surface conditions are compared to the theoretical C_d curves as computed by PANDA, which are shown in Figure 35. PANDA could not compute the coefficient of drag at an angle of attack greater than 12°, which is reflected in Figure 35 by the sudden stop.

Similar to the coefficient of lift case, it appears as though there are three regions of angles of attack where the C_d have distinct characteristics: 0° - 6°, 6° - 10°, and angles of attack greater than 10°.

In the first region ($0° < \alpha < 6°$), the C_d curve for the clean airfoil surface decreases whereas the hydrophilic and hydrophobic coating, the C_d curves are increasing. The differences between the C_d curves for the theoretical value and the three other surface coatings are between 64.0% and 82.6%.

In the second region ($6° > \alpha > 10°$), the differences between the theoretical C_d curves compared to the C_d curves of all three coatings range between 20.3% and 146%. The difference between the C_d curves for the hydrophilic coated airfoil and the clean surface airfoil is within 42.2%, whereas the difference between the C_d curves for the hydrophobic coated airfoil and the clean surface airfoil is a 24.6% difference.

In the third region ($\alpha > 10°$), the differences between the hydrophilic and hydrophobic coated airfoil C_d curves and the clean surface airfoil C_d curve are 15.4% and 7.6%, respectively.

7.4 Liquid Water Content

The water injection system was used to simulate rainfall within the Marine Icing Wind Tunnel (MIWT). With an increase in the MIWT free stream velocity, the cross section of the plume of droplets would decrease. Figure 36 shows the

relationship between the liquid water content (LWC), the spray diameter and the Reynolds number.

As the free stream velocity of the air within the MIWT increases, the spray diameter will decrease, and the liquid water content also decreases. The LWC of the simulated rainfall was 10.78 g/m^3 at a Reynolds number of 1.0 x 10^5 and it decreases to a LWC of 5.37 g/m^3 when the Reynolds number is increased to 3.0 x 10^5. The spray diameter of the MIWT decreases from 0.22 m to 0.18 m when the Reynolds number is increased from 1.0 x 10^5 to 3.0 x 10^5.

7.5 Simulated Rainfall Results

After the water injection system was enabled, a settling time of 30 minutes was used to ensure a stable film thickness. The airfoil was placed in the simulated rain within the MIWT under all three different surface conditions.

7.5.1 Coefficient of Lift

The coefficient of lift of all three surface conditions was determined from the data collected in the simulated rainfall within the MIWT and compared against the coefficient of lift for the clean surface airfoil in dry conditions. The comparison of the data is shown in Figure 37.

As in the case with the dry wind tunnel conditions, there appear to be three regions that characterize the C_l curves. The three regions are angles of attack that fall within: 0° - 6°, 6° - 10° and angles of attack greater than 10°.

In the first region ($0° < \alpha < 6°$), the C_l decreases by 13.6% between the clean surface airfoil in the wet condition as opposed to the dry condition. The hydrophilic coated airfoil however, experiences a decrease in lift of 3.6%, whereas, the lift for the hydrophobic coated airfoil is reduced by 26.0%.

In the second region ($6° < \alpha < 10°$), the clean surface airfoil experiences a 15.8% loss in lift during this region due to the simulated rainfall. The hydrophobic coated airfoil loses 27.8% in lift in the second region, whereas the hydrophilic coated airfoil only loses 2.2% of lift.

The third region ($\alpha > 10°$), where the slope of the C_l curves are close to zero, the clean surface airfoil experiences a 17.7% loss in lift. The hydrophilic coated airfoil loses 1.7% lift. The hydrophobic coated airfoil has a loss of lift of 25.4%.

Over the entire range of angles of attack, the clean airfoil surface loses on average 14.5% lift in simulated rain conditions. The hydrophilic and hydrophobic coated airfoils lose on average 2.0% and 25.2%, respectively.

7.5.2 Coefficient of Drag

The coefficient of drag of all three surface conditions was determined from the data collected in the simulated rainfall within the MIWT and compared against the coefficient of drag for the clean airfoil in dry conditions. The C_d curves are shown in Figure 38.

Similar to the coefficient of lift case, it appears as though there are three regions of angles of attack where the C_d have distinct characteristics: 0° - 6°, 6° - 10°, and angles of attack greater than 10°.

In the first region ($0° < \alpha < 6°$), the slope of all the C_d curves appear to be similar and close to zero. The values for the coefficient of drag however, are vastly different. The clean surface airfoil drag increases by a factor of 5, the result is the same for the hydrophobic coated airfoil case. The hydrophilic coated airfoil has a coefficient of drag increase of 79.6%.

In the second region ($6° < \alpha < 10°$), the coefficient of drag of the clean surface airfoil increases by a factor of 11.5 in the simulated rainfall as compared to the dry conditions. The hydrophilic coated airfoil experiences an increase in drag by a factor of 4, whereas the hydrophobic coated airfoil has an increase in drag by a factor of 12.5.

The third region ($\alpha > 10°$), the clean surface airfoil experiences a 94.8% increase in drag from the dry condition case. The hydrophilic and hydrophobic coated airfoils have an increase in the coefficient of drag in the simulated rainfall of 62.3% and 143.3%, respectively.

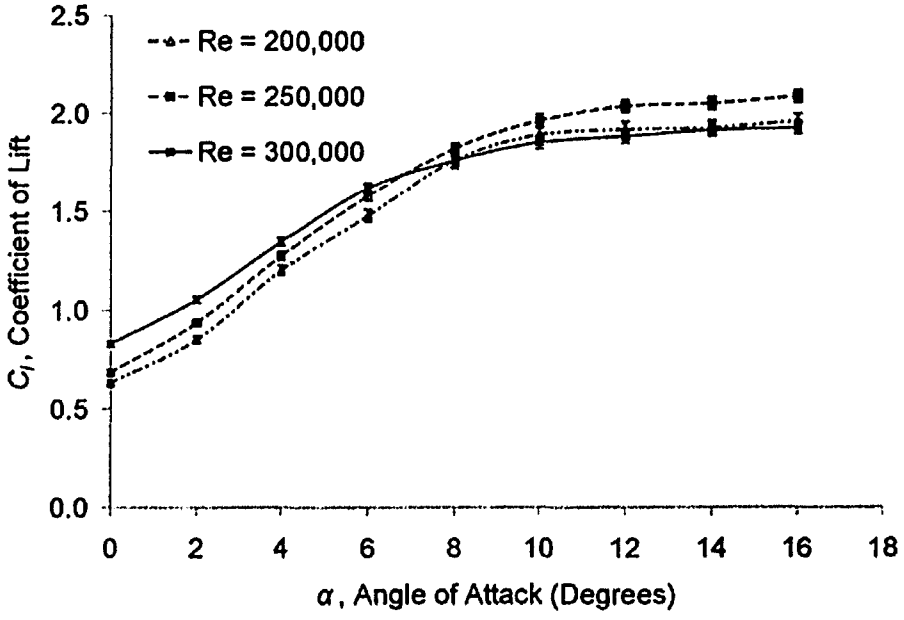

Figure 29: Coefficient of lift curves for various Reynolds numbers of a clean airfoil surface in dry conditions.

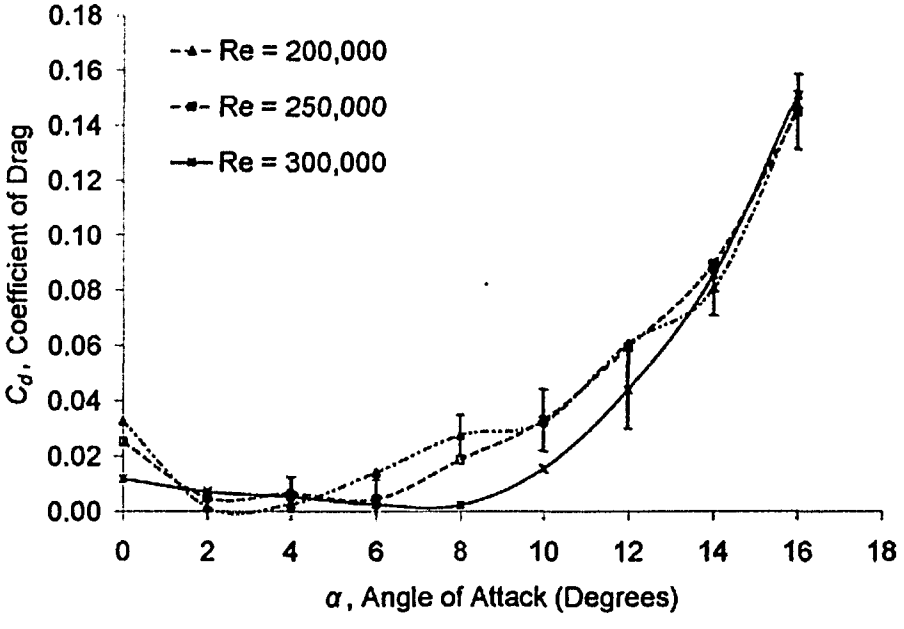

Figure 30: Coefficient of drag curves for various Reynolds numbers of a clean airfoil surface in dry conditions.

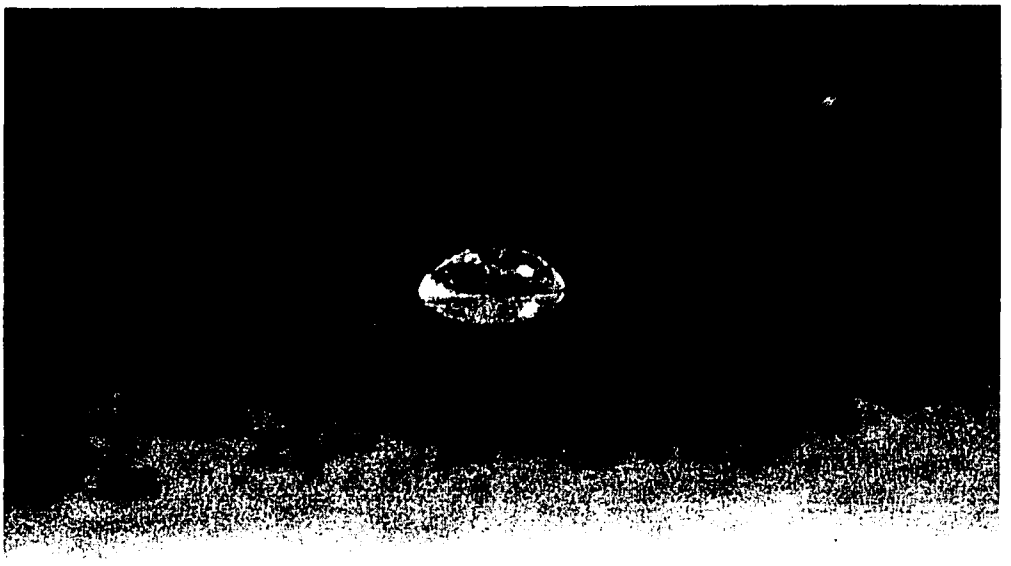

Figure 31: Water droplet on the clean airfoil surface. This picture was used to determine the contact angle (θ) for the clean airfoil surface. The contact angle was determined to be 60 ± 1°.

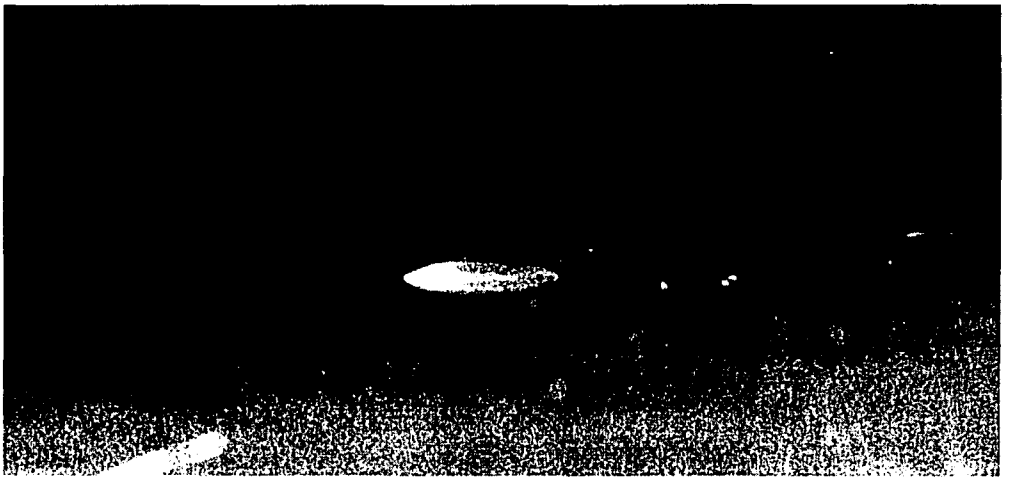

Figure 32: Water droplet on the hydrophilic airfoil surface. This picture was used to determine the contact angle (θ) for the hydrophilic airfoil surface. The contact angle was determined to be 22 ± 1°.

Figure 33: Water droplet on the hydrophobic airfoil surface. This picture was used to determine the contact angle (θ) for the hydrophobic airfoil surface. The contact angle was determined to be 90 ± 1°.

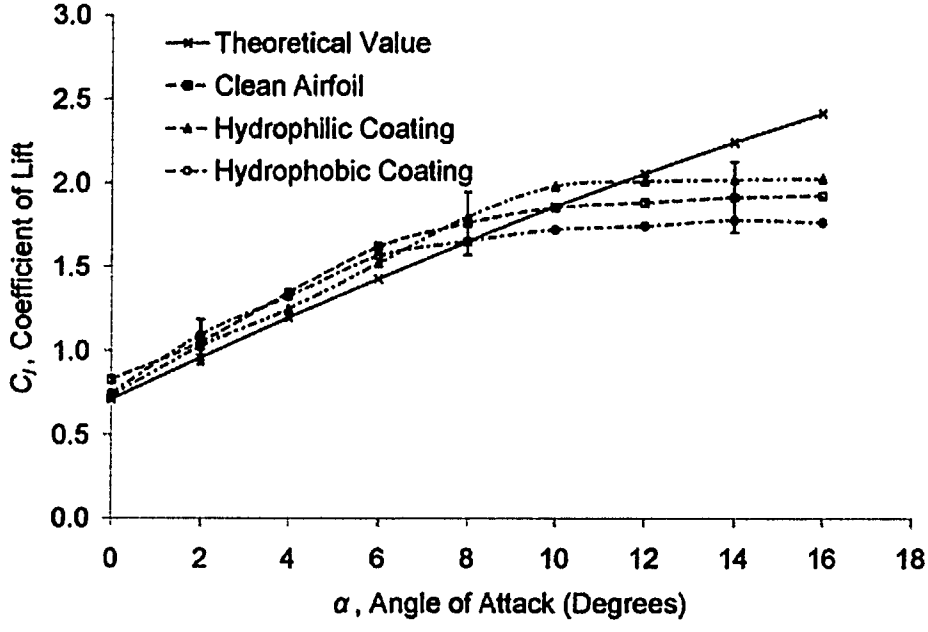

Figure 34: The coefficient of lift curves for the three surface conditions compared to the theoretical lift determined from PANDA. These curves were taken at a sampling rate of 100 samples/second in dry conditions.

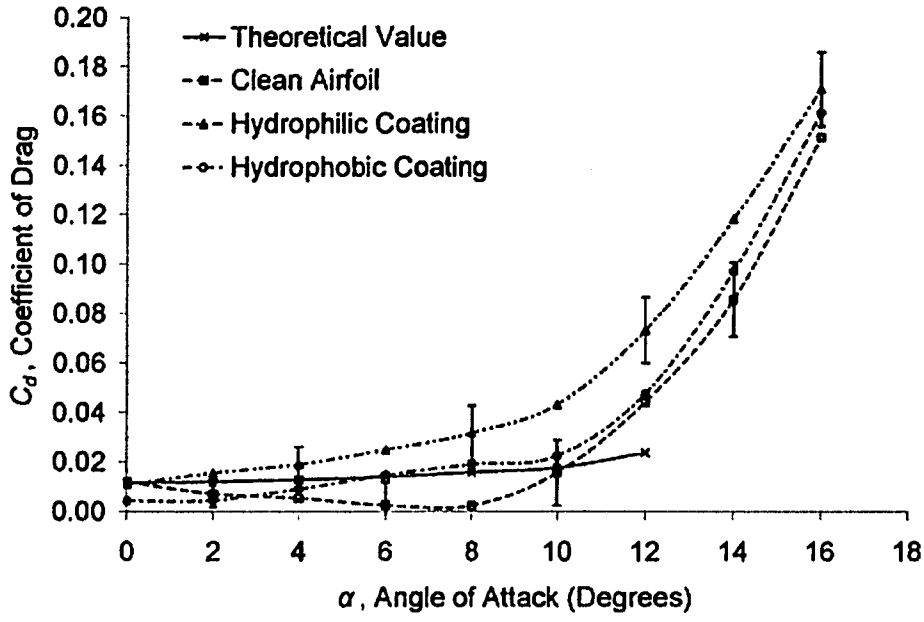

Figure 35: The coefficient of drag curves for the three surface conditions compared to the theoretical drag determined from PANDA. These curves were taken at a sampling rate of 100 samples/second in dry conditions.

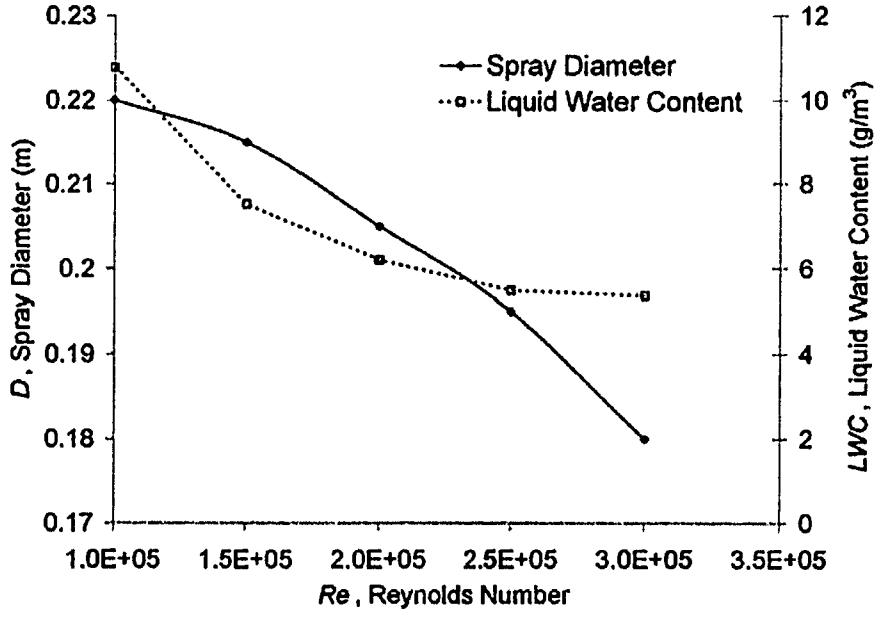

Figure 36: The water injection system spray diameter and liquid water content during simulated rainfall within the MIWT.

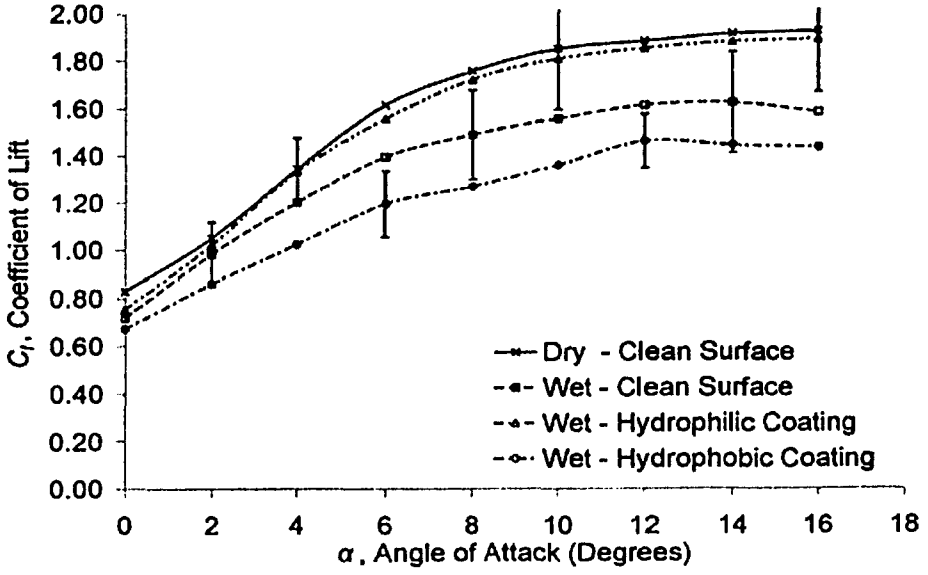

Figure 37: The coefficient of lift curves for the three surface conditions in simulated rainfall compared to the clean surface in dry condition. These curves were taken at a sampling rate of 1000 samples/second. The liquid water content (LWC) of the simulated rainfall was 5.37 g/m^3.

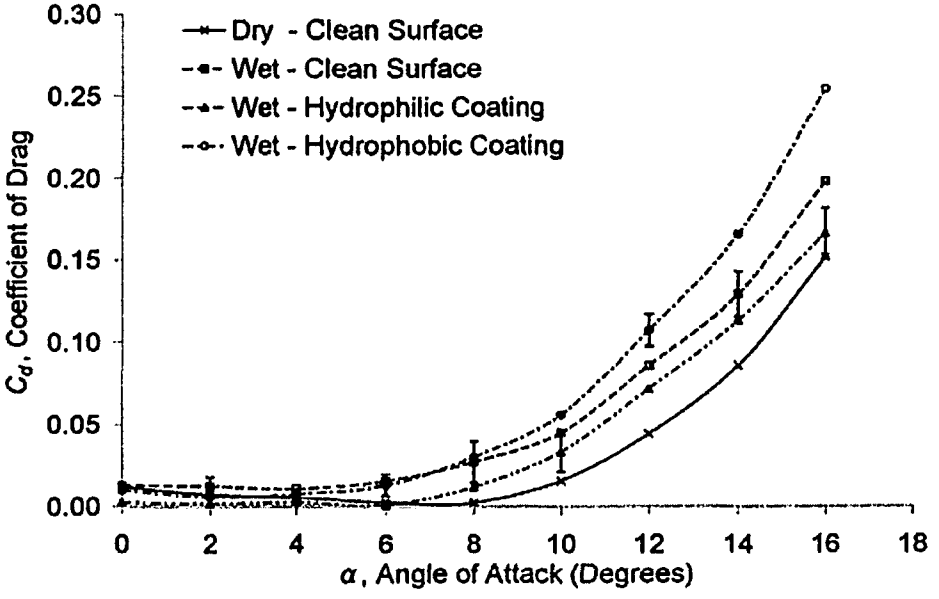

Figure 38: The coefficient of drag curves for the three surface conditions in simulated rainfall compared to the clean surface in dry condition. These curves were taken at a sampling rate of 1000 samples/second. The liquid water content (LWC) of the simulated rainfall was 5.37 g/m^3.

8.0 Discussion of Results

8.1 Effects of Reynolds Numbers

The effects of Reynolds numbers on the coefficient of lift and drag were analyzed from the results collected. Both the coefficient of lift and drag behaved in a wavy type pattern until a Reynolds number of 2.0×10^5 was reached. This behavior may be attributed to fluctuations in the MIWT motor power at low outputs. These fluctuations in the motor power may have caused perturbations in the free stream velocity which would be detrimental in determining the lift and drag due to the momentum constantly changing. It seems the MIWT motor output stabilized at a Reynolds number of 3.0×10^5, as the waviness type patterns in the C_l and C_d curves dissipated and became smooth curves.

8.2 Contact Angle and Surface Wettability

Droplets were placed on the three different surface conditions of the airfoil and are seen in Figure 31 for the clean surface airfoil, Figure 32 for the hydrophilic coated airfoil and Figure 33 for the hydrophobic coated airfoil. The droplet volume for each airfoil surface was the same (2 mL), but the droplet surface interaction was completely different. The clean surface airfoil had a contact angle of $60 \pm 1°$, which is defined as an incompletely wettable surface. The hydrophilic coated surface is also defined as an incompletely wettable surface, but as is evident from the photograph of the droplet, the contact angle is less, $22 \pm 1°$. This results in a lower droplet height and a greater droplet surface contact area than clean surface airfoil. On the contrary,

the hydrophobic droplet has the greatest contact angle, 90 ± 1°, a contact angle which is defined as a completely non-wettable surface. It has a greater droplet height than the clean surface airfoil. The greater droplet height reduces the droplet surface contact area.

8.3 Comparison of Experimental to Theoretical Data

The software used for determining the theoretical values for the coefficients of lift and drag was PANDA, developed by Desktop Aeronautics. These coefficients were determined using a Reynolds number of 3.0×10^5 and varying the angles of attack from 0° to 16°.

The theoretical coefficient of lift curve in Figure 34 appears to be a straight line with a C_l of approximately 0.75 at 0° angle of attack and increasing to approximately 2.5 at 16° angle of attack. The experimental data is not a straight line and it seems like there are three regions of angles of attack in which the characteristics of the C_l curve can be categorized:

1. A relatively straight portion with a constant positive slope which occurs between 0° - 6° angles of attack.
2. A transition section where the line deviates from the constant positive slope which occurs between 6° - 10° angles of attack,
3. A horizontal section of the curve which occurs when the angle of attack exceeds 10°

In the first region ($0° < \alpha < 6°$), the coefficient of lift curve for all three surface conditions seems to follow the same constant slope as the theoretical, albeit a slightly

greater value of C_l. The three surface coatings are fairly close to each other; where the C_l difference between the hydrophilic coated and clean airfoil is within 11.8%, whereas the hydrophobic coated airfoil C_l values are slightly closer to the clean airfoil at 10.0%.

In the second region ($6° < \alpha < 10°$), there is a transition where the slope of the C_l curves for all three surface conditions deviates from the theoretical slope. The hydrophobic coated and clean surface airfoil have a gradual transition to a near constant value of C_l over the entire transition region. The hydrophilic coated airfoil has a more abrupt transition that occurs at an angle of attack of 10°. The hydrophilic coated airfoil has a greater maximum C_l than the clean airfoil during this region. The hydrophilic and hydrophobic coated surfaces still have C_l values that are close to the clean airfoil surface as they are within 7.1%.

In the third region of angles of attack ($\alpha > 10°$), the slope of the C_l curves for all three surface conditions seem to be zero. The hydrophilic coating has a greater coefficient of lift than the clean airfoil by 6.7% whereas the hydrophobic coating has a lower coefficient of lift then the clean airfoil by 8.5%.

For all the regions, the coefficient of lift values of the hydrophobic and hydrophilic coatings were within 14.2% of the clean airfoil values. This suggests that the coatings did not affect the C_l values in the dry conditions, and that the coatings were applied correctly and uniformly.

PANDA could not compute the theoretical coefficient of drag past an angle of attack of 12° which is reflected in Figure 35 as the abrupt stop. It appears that the C_d

curves for the three airfoil surface conditions are not as close together as the C_l curves.

Between the angles of attack of 0° and 8°, the hydrophobic and hydrophilic coated airfoils have a completely different slope then the clean surface airfoil. The two coated surfaces have an increasing C_d curve whereas the clean surface airfoil is actually experiencing a reduction in the C_d values.

After the angle of attack has reached 10°, all three experimental C_d curves appear to be converging together. The difference in the C_d curves may suggest that although the coatings were applied correctly and uniformly, they increased the surface roughness of the airfoil.

8.4 Liquid Water Content

An increasing MIWT free stream velocity changes the spray diameter of the mist captured in the free stream velocity. The amount of water being injected into the system is not changing, only the cross sectional area of the plume of droplets and the volume of air in which the droplet laden cross flow is contained in. Both these variables contribute to the non-linear inversely proportional relationship between the Reynolds number and the liquid water content (LWC). The LWC of the simulated rainfall at a Reynolds number of 1×10^5 was 10.78 g/m^3 and decreases to a LWC of 5.37 g/m^3 at a Reynolds number of 3.0×10^5. The spray diameter of the injected water stream decreases from 0.22 m to 0.18 m when the Reynolds number was increased from 1.0×10^5 to 3.0×10^5.

The liquid water content (LWC) of the flow varied inversely with the Reynolds number, due to a constant water injection rate. The LWC of the injection spray was high enough to thoroughly coat the airfoil with droplets, so this event was not taken as a detrimental factor in this study.

8.5 Simulated Rainfall Results

The coefficient of lift of all three surface conditions in the simulated rainfall is compared against the coefficient of lift for the clean airfoil in dry conditions and is shown in Figure 37.

All the C_l curves seem to follow the same general shape of the clean surface airfoil in dry conditions. The clean surface airfoil has approximately a 15% loss of lift under the simulated rainfall, which was also found in the study performed by Thompson et al. (1995). The hydrophilic coated airfoil loses on average 2.0% lift through the entire range of angles of attack studied. Therefore, it seems like the hydrophilic coating on the surface of the airfoil has minimized the degradation of the aerodynamic property of lift. This is in contradiction to previous studies performed by Marchman et al. (1987) and Hansman et al. (1985), where the authors found that the C_l loss of a hydrophilic coated airfoil was greater than the loss experienced with a clean surface airfoil. There are many possible reasons for this discrepancy between these previous studies and this study's conclusions:

1. May be attributed to the type of hydrophilic coating that was applied in both the previous studies. A soap coating was used as the hydrophilic coating that would wash away during the study, therefore a stable film thickness was not

developed before the tests started. The hydrophilic coating used during this experiment was able to resist being washed off during tests in the simulated rainfall, therefore a stable film could develop which would provide an explanation of the different results.

2. The airfoils used in the studies by Marchman et al. (1987) and Hansman et al. (1985) may have had different aerodynamic properties when the hydrophilic coating was applied.
3. The degree of surface wettability as measured by the contact angle was not performed in the Marchman et al. (1987) study and could not be determined in the study by Hansman et al. (1985). Therefore, a direct correlation can not be construed between the hydrophilic coatings.

Of all these reasons listed, the most probable is the first explanation which was also mentioned by Hansman et al. (1985) as a possible source of error. The soap being washed away may have increased the surface roughness.

The hydrophobic coated surface experienced a degradation in the coefficient of lift on average by 25.2%. The loss in lift for a waxed airfoil was also observed by Marchman et al. (1987) and Hansman et al. (1985).

The coefficient of drag for the three surface conditions in simulated rainfall was also compared with the coefficient of drag for the clean surface airfoil and is shown in Figure 38. The C_d curves for all three surface types follow the same general shape as the C_d curve for the clean airfoil surface in dry conditions. The values of C_d for each case are very different though. The C_d increased by a factor of

approximately 11.5 due to the simulated rainfall. During the experiment, it seemed like the water droplets were collecting in an area of the airfoil where the flow stagnated. This phenomenon was amplified by the use of a hydrophobic surface coating. For the waxed surface, the C_d increased by a factor of 12.5, largely due it seemed, to the amount and size of water beads collecting in the stagnated flow areas of the airfoil, thus altering the aerodynamic profile of the airfoil and overall roughness. This was also noted in the study by Thompson et al. (1995). This increase in the C_d may also be due to an increase in the form drag of the airfoil from the resultant change in the effective profile. Also, the free stream velocity may have to expend energy to tear these water beads off the trailing edge of the airfoil, therefore increasing the skin drag of the airfoil.

The increase in C_d due to the rain was minimized with the hydrophilic coating, albeit the increase was still approximately 80%. This is far less than the drastic increase of approximately 1150% in the case with no surface coating. It appears that the height of the water beads being dragged down the airfoil by the free stream velocity was greatly reduced by the increase in surface wettability, thus reducing both the form and skin drag of the airfoil in comparison with the non coated airfoil.

9.0 Conclusions

The refurbished Marine Icing Wind Tunnel (MIWT) provides an excellent tool for experiments to simulate various meteorological conditions. The velocity profiles were rather non consistent throughout the wind tunnel. The step wise increases in the velocity profile seem systematic and may be attributed to a number of factors.

1) The resolution of the incline multi-tube manometer.
2) Some of the tubes in the 36 tube rake may have had foreign materials present in the tubes or some of the tubes may have been crimped.
3) The low speed region of the velocity profile may be due to air flow recirculation around the corner of the wind tunnel.

The water injection system provides a constant stream of mist to be caught in the free stream velocity to simulate rainfall. The MIWT may need to be kept above flow rates of 10 m/s in order to avoid fluctuations in the flow rate caused by the motor that will affect readings that might be sensitive to these perturbations.

The procedure that was developed in this study to test airfoils provided an excellent baseline to follow when testing other airfoils or other surface conditions of the same airfoil. This procedure can be followed for all tests within the MIWT that require water injection or a controlled air flow rate in low Reynolds number flight. Though the liquid-water content (LWC) of the flow varied inversely with Reynolds number, due to a constant water injection rate, the LWC of the injection spray was

high enough to thoroughly coat the airfoil with droplets, so this event was not taken as a detrimental factor in this study.

Experiments have been conducted to quantify the performance degradation of naturally laminar flow airfoil in moderate rain (72 – 137 mm/hr). In addition, the surface wettability effects were observed. At a Reynolds number of 3.0×10^5 with a moderate rainfall of 5.37 g/m^3, a 15% reduction in the lift was observed. The loss of lift was amplified by the hydrophobic coating where there was a 25% reduction of lift. The hydrophilic case however, minimized the loss of lift of the airfoil to an average loss of only 2%. This implies that surface wettability plays a key role for lift in rain. The greater the surface wettability, which is characterized by the contact angle (θ), the less degradation of aerodynamic performance of lift in moderate to heavy rainfall will be observed. This may be attributed to the greater surface area of the droplet, which is reflected in a lower droplet height, thus minimizing the adverse pressure gradients along the airfoil.

The experimental data are in contradiction to previous studies performed by Marchman et al. (1987) and Hansman et al. (1985), where the authors found that the coefficient of lift loss of a hydrophilic coating were greater than the loss experienced with no coating application. The reason for the contradiction can be attributed to the type of hydrophilic coating that was applied in both the previous studies. Soap coatings were used by the previous authors as the hydrophilic coating, which would wash away during the study, therefore a stable film thickness was not developed before the authors started testing. The hydrophilic coating used during the present

experiment was able to resist washing off during tests in the simulated rainfall, therefore a stable film was employed and more accurate data could be collected.

The loss of lift paled in comparison to the increase of drag. The C_d increased by a factor of approximately 11.5 due to the simulated rainfall. During the experiment, it seemed like the water droplets were collecting in an area of the airfoil where the flow stagnated. This phenomenon was amplified by the use of a hydrophobic surface coating. For the waxed surface, the C_d increased by a factor of 12.5, largely due it seemed, to the amount and size of water beads collecting in the stagnated flow areas of the airfoil, thus altering the aerodynamic profile of the airfoil and overall roughness. This increase in the C_d may be due to an increase in the form drag (i.e. pressure drag) of the airfoil from the resultant change in the effective profile. Also, the free stream velocity may have to expend energy to tear these water beads off the trailing edge of the airfoil, therefore increasing the skin drag of the airfoil.

The increase in C_d due to the rain was minimized with the hydrophilic coating, although the increase was still approximately 80%. This is far less than the drastic increase of approximately 1150% in the case with no surface coating. It appears that the height of the water beads being dragged down the airfoil by the free stream velocity was greatly reduced by the increase in surface wettability, thus reducing the skin drag of the airfoil in comparison with the non coated airfoil.

The use of hydrophilic coatings on laminar flow airfoils should be looked to as a viable safety procedure in aviation. The minimal detrimental effects of performance of a hydrophilic surface coating in dry conditions can be offset by the

drastic improvement in the degradation of airfoil performance in rainfall. By contrast, waxed surfaces should not be used as a measure to reduce the effects of rainfall on naturally laminar flow airfoils. These conclusions may also be applied to axial flow airfoils in industrial applications such as wind turbine generation, but to know, more research would be necessary.

10.0 Recommendations for Future Work

Despite the successful completion of the objectives, the results of this study lead to many other interesting questions. This study laid the foundation for future work and experimentation using the Marine Icing Wind Tunnel which will be a powerful tool in the Department of Mechanical Engineering for those who would like to study the meteorological effects on surfaces. It is my hope that some one else will be able to continue the research that I have done. The areas within the study that I have conducted that may warrant further research would be:

1. Determine the effects that various droplet surface interactions have on the shedding frequency of a naturally laminar flight airfoil. Broeren et al. (1998) conducted research on low frequency flowfield unsteadiness during airfoil stall, but that was restricted to one surface type. Stalwell et al (2000) and Stalwell et al. (2001) conducted frequency analysis on airfoils at extremely high angles of attack. Brookfield et al. (1996) conducted a study on the effects of freestream swirl, but this was done on a rotating airfoil, not a stationary one with various degrees of surface roughness.
2. Unfortunately, due to the restriction on the blockage ratio within the wind tunnel, the airfoil could not achieve an angle of attack past the stall point. Further research into comparing the shedding frequencies past the stall point to the surface roughness may be useful in the aviation industry. Brookfield et al. (1996) conducted a study to determine the wake decay, but this was done on a rotating blade.

My recommendations to improve the current Marine Icing Wind Tunnel would be to:

1) Determine the whether the non-uniformities in the velocity distribution can be minimized using flow straighteners.
2) Modify or replace the current motor so there are no flow perturbations at low wind speeds.
3) Mount a Phase Doppler Anemometer (PDA) to the test section to measure the droplet size distribution and velocity.

11.0 Bibliography

A. Pope (1961), Wind Tunnel Calibration Techniques, North Atlantic Treaty Organization, Advisory Group for Aeronautical Research and Development, 1961.

A.J. Bilanin (1985), "Scaling Laws for Testing of High Lift Airfoils Under Heavy Rainfall", AIAA Paper 85-0257, 1985.

A.J. Wheeler, A.R. Ganji (2004) Introduction to Engineering Experimentation, 2nd Edition, Pearson Prentice Hall, 2004.

A.P. Broeren, M.B. Bragg (1998), "Low-Frequency Flowfield Unsteadiness During Airfoil Stall", AIAA Paper A98-32418, 1998.

A. Rohde, V.V. Golubev, C. Lessiau (2003), "Direct Simulation of Sound Generated by Viscous Flow Over a Cyclinder Using a TVD Method", AIAA Paper 2003-3239, 2003.

B. Lansberg (2004), "2003 Nall Report, Accidents Trends and Factors for 2002", AOPA Air Safety Foundation, 2004.

B. Krasovitski, A. Marmur (2005), "Drops Down the Hill: Theoretical Study of Limiting Contact Angles and the Hysteresis Range on a Tilted Plate", Langmuir 21 (2005) pp. 3881 – 3885.

B.E. Thompson, J. Jang, J.L. Dion (1995), "Wing Performance in Moderate Rain", Journal of Aircraft 32 (1995), pp. 1034 – 1039.

C.E. Foy (1988), The Design Instrumentation and Performance of a Refrigerated Marine Icing Wind Tunnel, M.Sc. Thesis, Department of Mechanical Engineering, University of Alberta, 1988.

C.N.H. Lock (1929), "The Interference of a Wind Tunnel on a Symmetrical Body", R. & M. 1275 (1929).

D.Y. Kwok, C.N.C. Lam, A. Li, A. Leung, R. Wu, E. Mok, A.W. Neumann (1998), "Measuring and interpreting contact angles: a complex issue" Colloids Surfaces A: Physicochemical and Engineering Aspects 142 (1998), pp. 219 – 235.

E. Ower, R.C. Pankhurst (1977), The Measurements of Air Flow, 5th Edition, Oxford, 1977.

F. White (1999), Fluid Mechanics, 4th Edition, McGraw-Hill Companies Inc., 1999.

G. Bouchard, J.L. Laforte, P. Louchez (1995), "Wind Tunnel Study of Lift Reduction on a Wing Section Covered with Anti-icing Fluid in Supercooled Precipitation", Canadian Aeronautics and Space Journal 41 (1995), pp. 185 – 192.

G.K. Batchelor (1944), "Interference on Wings, Bodies and Airscrews in a Closed Tunnel of Octagonal Section", A.C.A. 5 (1944).

G. McHale, N.J. Shirtcliffe, M.I. Newton (2004), "Contact-Angle Hysteresis on Super-Hydrophobic Surfaces", Langmuir 20 (2004), pp. 10146 – 10149.

I. Kroo, PANDA's User Guide, Desktop Aeronautics.

J.B. Barlow, W.H. Rae, A. Pope (1999), Low Speed Wind Tunnel Testing, 3rd Edition, Wiley, 1999.

J.F. Marchman III, E.A. Robertson, H.T. Emsley (1987), "Rain Effects at Low Reynolds Number", Journal of Aircraft 24 (1987), pp. 638 – 644.

J.K. Luers (1983), "Heavy Rain Effects on Aircraft", AIAA Paper 83-0206, 1983.

J.K. Luers, P.A. Haines (1983), "Experimental Measurements of Rain Effects on Aircraft Aerodynamics", AIAA Paper 83-0275, 1983.

J.M. Brookfield, I.A. Waitz, J. Sell (1996), "Wake Decay: Effect of Freestream Swirl", ASME Paper 98-GT-495, 1996.

J. Stewart (1995), Calculus: Early Transcendentals, 3rd Edition, Brooks/Cole Publishing Company, 1995.

K.E. Swalwell, J. Sheridan, W.H. Melbourne (2000), "Frequency Analysis of Surface Pressures on an Airfoil After Stall", American Institute of Aeronautics and Astronautics, 2000.

K.E. Swalwell, J. Sheridan, W.H. Melbourne (2001), "The Effect of Turbulent Intensity on Stall of the NACA 0021 Aerofoil" 14th Australasian Fluid Mechanics Conference, 2001.

N.E. Mease, W.G. Cleveland, G.E. Mattingly, J.M. Hall (1992), "Air Speed Calibrations At The National Institute Of Standards And Technology", NIST Paper, 1992.

P.A. Haines, J.K. Luers (1983), "Aerodynamic Penalties of Heavy Rain on Landing Airplanes", Journal of Aircraft 20 (1983), pp. 111 – 119.

P.A. Lyon, W. Fuerst (1998) Introductory Digital Signal Processing with Computer Applications, 2nd Edition, Wiley, 1998.

R.C. Pankhurst (1965), Wind-tunnel technique; an account of experimental methods in low and high speed wind tunnels, London, 1965.

R.L. Daugherty, J.B. Franzini and E.J. Finnemore (1985), Fluid Mechanics with Engineering Applications, 8th Edition, McGraw-Hill Book Company, 1985.

R.J. Hansman Jr., M.F. Barsotti (1985), "Surface Wetting Effects on a Laminar Flow Airfoil in Simulated Heavy Rain", Journal of Aircraft 22 (1985), pp. 1049 – 1053.

Z. Hongliang, M. Fanjuan, C. Zuoyi (1998), "A Numerical Investigation of the Effect on Airfoil Lift-Drag Ratio of Locally Enhanced Surface Roughness", Wind Engineering 22 (1998), pp. 143 – 148.

Appendix A

Contents:

1) Airfoil Coordinates

Table A1: Airfoil Profile Data that was supplied by ARV Development Corp. for the custom designed naturally laminar flow airfoil that was used during this study.

x	y upper	y lower	camber line	center line	thickness (mm)	height (mm)
0	0	0	0	0	0	0
0.001541	0.006606	-0.00994	-0.0016665	0	0.3309	-0.03333
0.006156	0.018123	-0.01733	0.000399	0	0.70896	0.00798
0.013815	0.031871	-0.0228	0.004535	0	1.09344	0.0907
0.024472	0.044452	-0.02702	0.008715	0	1.42948	0.1743
0.03806	0.055545	-0.03058	0.012482	0	1.72252	0.24964
0.054497	0.066798	-0.034	0.0163995	0	2.01594	0.32799
0.07368	0.077503	-0.03745	0.020025	0	2.29912	0.4005
0.095491	0.087845	-0.04019	0.0238275	0	2.5607	0.47655
0.119797	0.097535	-0.04246	0.0275365	0	2.79994	0.55073
0.146447	0.106528	-0.04446	0.0310345	0	3.01974	0.62069
0.175276	0.11474	-0.0456	0.0345715	0	3.20674	0.69143
0.206107	0.122025	-0.04644	0.0377905	0	3.36938	0.75581
0.238751	0.128329	-0.04703	0.040651	0	3.50712	0.81302
0.273005	0.13354	-0.047	0.0432715	0	3.61074	0.86543
0.308658	0.137559	-0.04651	0.0455255	0	3.68134	0.91051
0.345491	0.140305	-0.0456	0.047354	0	3.71804	0.94708
0.383277	0.141514	-0.04455	0.0484805	0	3.72134	0.96961
0.421783	0.141091	-0.04282	0.049134	0	3.67828	0.98268
0.46077	0.138902	-0.04065	0.0491275	0	3.59098	0.98255
0.5	0.134648	-0.0383	0.0481725	0	3.45902	0.96345
0.539229	0.128654	-0.03536	0.0466485	0	3.28022	0.93297
0.578217	0.121315	-0.03191	0.044704	0	3.06444	0.89408
0.616723	0.113208	-0.02862	0.0422935	0	2.83658	0.84587
0.654508	0.104598	-0.0252	0.0396995	0	2.59594	0.79399
0.691342	0.095665	-0.02165	0.037009	0	2.34624	0.74018
0.726995	0.086653	-0.01832	0.034167	0	2.09944	0.68334
0.761249	0.077629	-0.01495	0.031338	0	1.85164	0.62676
0.793893	0.068579	-0.01124	0.02867	0	1.59636	0.5734
0.824724	0.059886	-0.00754	0.0261725	0	1.34854	0.52345
0.853553	0.051478	-0.00411	0.0236855	0	1.1117	0.47371
0.880203	0.043502	-0.00126	0.0211205	0	0.89526	0.42241
0.904508	0.036169	0.000192	0.0181805	0	0.71954	0.36361
0.92632	0.02938	0.004365	0.0168725	0	0.5003	0.33745
0.945503	0.023064	0.001585	0.0123245	0	0.42958	0.24649
0.96194	0.017012	0.001141	0.0090765	0	0.31742	0.18153
0.975528	0.011456	0.001554	0.006505	0	0.19804	0.1301
0.986185	0.006712	0.001414	0.004063	0	0.10596	0.08126
0.993844	0.003073	0.000843	0.001958	0	0.0446	0.03916
0.998459	0.000782	0.000247	0.0005145	0	0.0107	0.01029
1	0	0	0	0	0	0

Appendix B

Contents:

1) Marine Icing Wind Tunnel Performance Data

Table B1: Data collected during the performance test of the MIWT. This data was used to determine the velocity profile of the test section. The velocity measurements were taken at 4 positions length-wise in 12 cm increments. The measurements were taken with a 36 Pitot tube rake with spacing at 5 mm apart.

Position from Center (cm)	Velocity (m/s)			
	- 18 cm	-6 cm	6 cm	18 cm
-18	6.907096	6.907096	5.98172	5.98172
-17.5	6.907096	6.907096	5.98172	5.98172
-17	6.907096	6.907096	6.907096	6.907096
-16.5	6.907096	6.907096	6.907096	6.907096
-16	6.907096	6.907096	6.907096	6.907096
-15.5	5.98172	5.98172	5.98172	5.98172
-15	6.907096	6.907096	6.907096	6.907096
-14.5	6.907096	6.907096	6.907096	6.907096
-14	6.907096	6.907096	6.907096	6.907096
-13.5	6.907096	6.907096	5.98172	5.98172
-13	6.907096	6.907096	5.98172	5.98172
-12.5	5.98172	5.98172	5.98172	5.98172
-12	6.907096	6.907096	6.907096	6.907096
-11.5	6.907096	6.907096	5.98172	5.98172
-11	6.907096	6.907096	5.98172	5.98172
-10.5	6.907096	6.907096	6.907096	6.907096
-10	6.907096	6.907096	6.907096	6.907096
-9.5	6.907096	6.907096	6.907096	6.907096
-9	6.907096	6.907096	6.907096	6.907096
-8.5	6.907096	6.907096	6.907096	6.907096
-8	5.98172	5.98172	5.98172	5.98172
-7.5	5.98172	5.98172	5.98172	5.98172
-7	6.907096	6.907096	6.907096	6.907096
-6.5	6.907096	6.907096	6.907096	6.907096
-6	6.907096	6.907096	6.907096	6.907096
-5.5	6.907096	6.907096	6.907096	6.907096
-5	5.98172	5.98172	5.98172	5.98172
-4.5	5.98172	5.98172	5.98172	5.98172
-4	5.98172	5.98172	5.98172	5.98172
-3.5	6.907096	6.907096	5.98172	5.98172
-3	6.907096	6.907096	6.907096	6.907096
-2.5	6.907096	6.907096	6.907096	6.907096
-2	6.907096	6.907096	6.907096	6.907096
-1.5	6.907096	6.907096	6.907096	6.907096
-1	6.907096	6.907096	6.907096	6.907096
-0.5	6.907096	6.907096	6.907096	6.907096

0.5	5.98172	5.98172	5.98172	5.98172
1	5.98172	5.98172	5.98172	5.98172
1.5	6.907096	6.907096	6.907096	6.907096
2	6.907096	6.907096	6.907096	6.907096
2.5	6.907096	6.907096	6.907096	6.907096
3	5.98172	5.98172	5.98172	5.98172
3.5	6.907096	6.907096	6.907096	6.907096
4	6.907096	6.907096	6.907096	6.907096
4.5	6.907096	6.907096	6.907096	6.907096
5	5.98172	5.98172	5.98172	5.98172
5.5	5.98172	5.98172	5.98172	5.98172
6	5.98172	5.98172	5.98172	5.98172
6.5	5.98172	5.98172	6.907096	6.907096
7	5.98172	5.98172	5.98172	5.98172
7.5	5.98172	5.98172	5.98172	5.98172
8	6.907096	6.907096	6.907096	6.907096
8.5	5.98172	5.98172	5.98172	6.907096
9	5.98172	5.98172	5.98172	5.98172
9.5	5.98172	5.98172	5.98172	5.98172
10	5.98172	5.98172	5.98172	5.98172
10.5	5.98172	5.98172	5.98172	5.98172
11	5.98172	5.98172	5.98172	5.98172
11.5	5.98172	5.98172	5.98172	5.98172
12	6.907096	5.98172	6.907096	6.907096
12.5	6.907096	5.98172	6.907096	6.907096
13	6.907096	6.907096	6.907096	6.907096
13.5	4.884054	5.98172	5.98172	5.98172
14	4.884054	5.98172	4.884054	5.98172
14.5	4.884054	5.98172	4.884054	5.98172
15	5.98172	4.884054	5.98172	5.98172
15.5	6.907096	4.884054	6.907096	6.907096
16	6.907096	4.884054	6.907096	6.907096
16.5	6.907096	5.98172	6.907096	6.907096
17	6.907096	6.907096	6.907096	6.907096
17.5	5.98172	5.98172	5.98172	5.98172
18	6.907096	5.98172	6.907096	6.907096

Appendix C

Contents:

Calibration of the Airfoil Data Acquisition System Results for the:

1) Portable Strain Indicator Vishay Model P3500

Table C1: Calibration results for the portable strain indicator when a force was applied to the airfoil in the normal direction.

Mass (grams)	Force Applied (N)	Induced Strain (microstrain)
10	0.10	5
20	0.20	9
50	0.49	19
100	0.98	33
200	1.96	65
500	4.91	160
1000	9.81	340

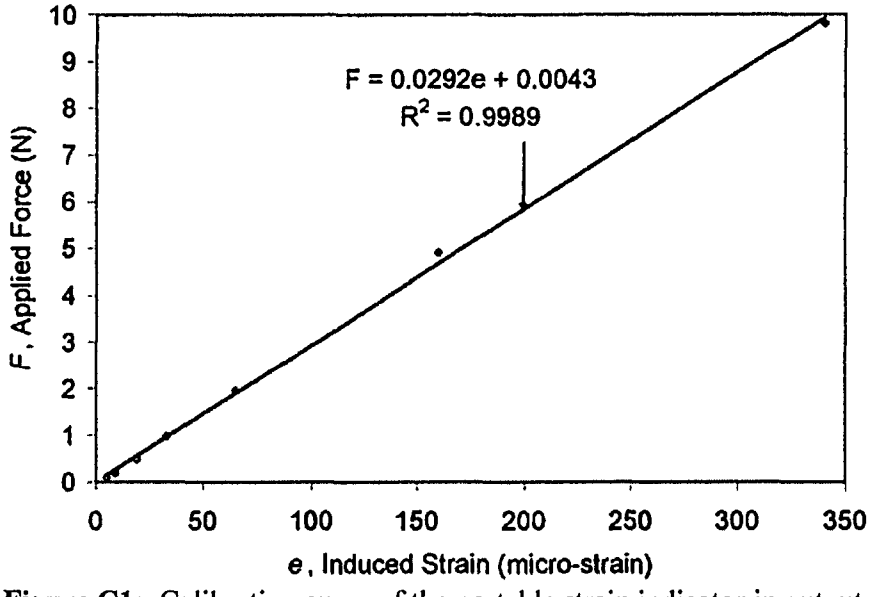

Figure C1: Calibration curve of the portable strain indicator in output micro-strain when a force was applied to the airfoil.

2) National Instruments 6052E DAQ Card

Table C2: Calibration results for the data acquisition system when a force was applied to the airfoil in the normal direction. The results are the normal and chord-wise component of output voltage.

Mass (grams)	Force (N)	Normal (Volts)	Chord-wise (Volts)
0	0.0000	0.00000	0.00000
50	0.4905	0.09544	-0.01258
100	0.9810	0.19018	-0.02341
200	1.9620	0.38067	-0.04371
300	2.9430	0.57125	-0.06354
400	3.9240	0.76188	-0.08369
500	4.9050	0.95038	-0.10326

Table C3: Calibration results for the Data Acquisition system when a force was applied to the airfoil in the chord-wise direction. The results are the normal and chord-wise component of output voltage.

Mass (grams)	Force (N)	Normal (Volts)	Chord-wise (Volts)
0	0.0000	0.00000	0.00000
50	0.4905	0.00302	0.21813
70	0.6867	0.00527	0.30704
100	0.9810	0.00629	0.43706
150	1.4715	0.00945	0.65768
200	1.9620	0.01348	0.87813

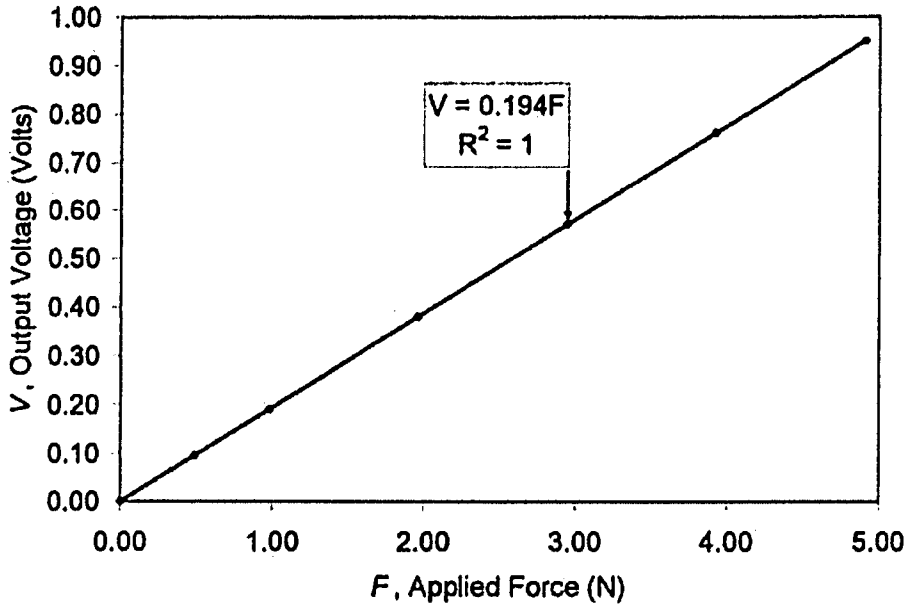

Figure C2: The calibration curve of the normal component of output voltage when a force along the normal axis of the airfoil is applied.

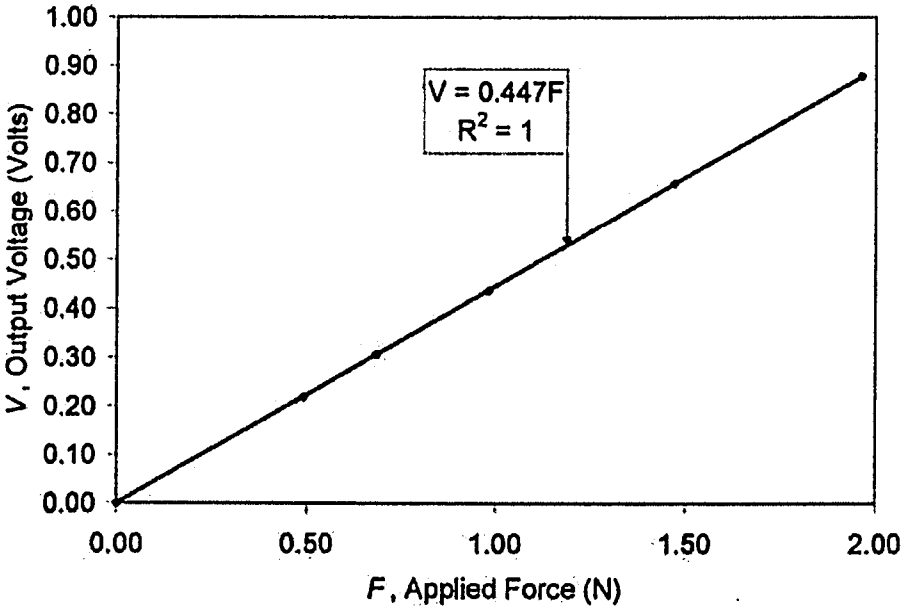

Figure C4: The calibration curve of the chord-wise component of output voltage when a force along the chord-wise axis of the airfoil is applied.

Appendix D

Contents:

Design Calculations

1) Strain Gauges and Wheatstone Bridge Output Resolution

For a full Wheatstone bridge circuit using a 5 Volt excitation, the maximum strain that can be measured is:

$$4\varepsilon = \frac{V_0(R_2 + R_3)^2}{V_s(GF)R_2R_3} \qquad [D1]$$

where:

V_o	=	Output Voltage	(0.05 Volts)
V_s	=	Excitation Voltage	(5 Volts)
GF	=	Gauge Factor	(2.135)
R_2	=	Resistance	(350 Ohm)
R_3	=	Resistance	(350 Ohm)
ε	=	Strain	(μS)

$$4\varepsilon = \frac{(0.05V)\cdot(350\Omega + 350\Omega)^2}{(5V)\cdot(2.135)\cdot 350\Omega\cdot 350\Omega} \qquad [D2]$$

$$4\varepsilon = 18732 \qquad [D3]$$

$$\varepsilon = 4683\,\mu S \qquad [D4]$$

The DAQ card is 16 bit therefore the resolution is:

$$resolution = \frac{\varepsilon}{2^{bits} - 1} \qquad [D5]$$

$$resolution = \frac{4683\,\mu S}{2^{16} - 1} \qquad [D6]$$

$$resolution = 0.29\,\mu S \qquad [D7]$$

From the Portable Strain Indicator Vishay Model P3500 calibration in Appendix C, the resolution can be converted from micro-strain (μS) to a corresponding Voltage.

$$resolution_{(N)} = resolution_{(\mu S)} \cdot \frac{applied\ force}{induced\ strain} \qquad [D8]$$

The $resolution_{(N)}$ is the resolution of the data acquisition system in units of force instead of the resolution in units of micro-strain, ($resolution_{(\mu S)}$).

$$resolution_{(N)} = 0.29\mu S \cdot \frac{1.962N}{65\mu S} \qquad [D9]$$

Therefore the output resolution of the data acquisition system is:

$$resolution_{(N)} = 0.009N \qquad [D10]$$

2) Tunnel Interference Factor

When conducting experiments in a closed section wind tunnel, the effects the walls have on the streamlines must be considered. An effect of the wall constraint is the suppression of the lateral expansion of the streamlines in the region of the model. This suppression effect will produce an increase the axial component of velocity along the airfoil. Thus, the influence the walls place on the experiment will be an increase in the wind tunnel speed at the location of the model airfoil.

Equation [12] in the Theory section is the correction factor for the influence of the walls on the experiment.

$$U_F = U_T\left[1+0.822\left(\frac{t+c}{h}\right)\right] \qquad [D11]$$

where:	U_F	=	Corrected Tunnel Speed	(m/s)
	U_T	=	Measured Tunnel Speed	(m/s)
	t	=	Airfoil Thickness	(0.0372 m)
	c	=	Airfoil Chord Length	(0.200 m)
	h	=	Height of Wind Tunnel	(0.500 m)

$$U_F = U_T\left[1+0.822\left(\frac{0.0372m+0.200m}{0.500m}\right)\right] \qquad [D12]$$

$$U_F = U_T(1.390) \qquad [D13]$$

Therefore the wind tunnel speed, U_T, is multiplied by a factor of 1.390 in order to get the corrected wind speed, U_F.

3) Wind Tunnel Velocity

The velocity profile of the MIWT is fully developed in the test section, therefore, the reading that was taken by the Pitot tube will be considered the centerline velocity. As the velocity measurement is a function of the air density, ρ, the air density must be calculated. The atmospheric pressure, P_{atm}, was determined by reading a barometric gauge and applying correction factors.

The density of the air, ρ, is determined by the ideal gas law as shown in the Theory section as Equation [18].

$$\rho = \frac{m}{V} = \frac{P}{RT} = \frac{P_{atm}}{\left(\frac{R_u}{M_{air}}\right)T} \qquad [D14]$$

where: P_{atm} = Atmospheric Pressure (92000 Pa)
R_u = Universal Gas Constant (8315 J/kmol K)
M_{air} = Molecular Weight of Air (28.97 kmol/kg)
T = Atmospheric Temperature (298.65 K)
ρ = Air Density (kg/m^3)

$$\rho = \frac{92000\ Pa}{\left(\frac{8315\ J/kmol\ K}{28.97\ kmol/kg}\right)298.65\ K} \qquad [D15]$$

$$\rho = 1.07\ kg/m^3 \qquad [D14]$$

Using the density of air, the wind tunnel velocity, U, was calculated using Equation [19].

$$U = \sqrt{\frac{2\rho_{gauge}gh}{\rho}} \qquad [D15]$$

where: ρ_{gauge} = Density of Fluid ($826\ kg/m^3$)
g = Gravitational Constant ($9.81\ m/s^2$)
h = Manometer Fluid Height (0.023 m)
ρ = Density of Air ($1.07\ kg/m^3$)
U = Wind Tunnel Velocity (m/s)

$$U = \sqrt{\frac{2\cdot(826\ kg/m^3)(9.81\ m/s^2)(0.023\ m)}{1.07 kg/m^3}} \qquad [D16]$$

$$U = 18.47\ {}^{m}/_{s} \qquad [D17]$$

The tunnel correction factor from [D13] is then applied to the measured wind tunnel velocity. Therefore:

$$U_F = \left(18.47\ {}^{m}/_{s}\right) \cdot (1.390) \qquad [D18]$$

$$U_F = 25.68\ {}^{m}/_{s} \qquad [D19]$$

4) Wind Tunnel Velocity Measurement Uncertainty

In order to determine the uncertainty in the wind tunnel velocity measurements, an uncertainty analysis was completed. The uncertainty in the measurement of air density calculated from Equation [73]:

$$\partial\rho_{air}{}^{2} = \left[\partial P_{atm}\left(\frac{1}{\frac{R_u}{M}T}\right)\right]^2 + \left[\partial T\left(\frac{-P_{atm}}{\frac{R_u}{M}T^2}\right)\right]^2 \qquad [D20]$$

where:

P_{atm}	=	Atmospheric Pressure	(92000 Pa)
∂P_{atm}	=	Uncertainty in Pressure	(133 Pa)
R_u	=	Universal Gas Constant	(8315 J/kmol K)
M_{air}	=	Molecular Weight of Air	(28.97 kmol/kg)
T	=	Atmospheric Temperature	(298.65 K)
∂T	=	Uncertainty in Temperature	(0.5 K)
$\partial\rho_{air}$	=	Air Density Uncertainty	(kg/m^3)

$$\partial\rho_{air}^{\,2} = \left[133\ Pa\left(\frac{1}{\frac{8315\ {}^{J}/_{kmol\ K}}{28.97\ {}^{kmol}/_{kg}}\cdot(298.65\ K)}\right)\right]^2 + \left[0.5\ K\left(\frac{-92000\ Pa}{\frac{8315\ {}^{J}/_{kmol\ K}}{28.97\ {}^{kmol}/_{kg}}\cdot(298.65\ K)^2}\right)\right]^2 \qquad [D21]$$

$$\partial\rho_{air}^{\,2} = [0.00155]^2 + [0.00359]^2 \qquad [D22]$$

$$\partial\rho_{air} = 0.004\ {}^{kg}/_{m^3} \qquad [D23]$$

The uncertainty in the measurement of pressure difference calculated from Equation [76]:

$$\partial\Delta P = \partial h \cdot \rho_{gauge} g \qquad [D24]$$

where: ∂h = Uncertainty in Height (0.0003 m)
$\partial\Delta P$ = Uncertainty in Pressure (Pa)

$$\partial\Delta P = 0.0003\ m \cdot \left(862\ {}^{kg}/_{m^3}\right) \cdot 9.81\ {}^{m}/_{s^2} \qquad [D25]$$

$$\partial\Delta P = 2.11\ Pa \qquad [D26]$$

The uncertainty in the pressure difference and the air pressure can be entered into Equation [80] to find the uncertainty in the wind tunnel velocity measurement:

$$\partial U^2 = \left[\partial\Delta P\left(\sqrt{\frac{2}{\rho_{air}}}\left(\frac{1}{2\sqrt{\Delta P}}\right)\right)\right]^2 + \left[\partial\rho_{air}\left(\frac{-1}{2}\sqrt{2\Delta P}\left(\rho_{air}^{-3/2}\right)\right)\right]^2 \quad [D27]$$

where:

ΔP	=	Pressure Difference	(183.18 Pa)
$\partial\Delta P$	=	Uncertainty in Pressure	(2.11 Pa)
ρ_{air}	=	Air Density	(1.07 kg/m^3)
$\partial\rho_{air}$	=	Air Density Uncertainty	(0.004 kg/m^3)
∂U	=	Uncertainty in Velocity	(m/s)

$$\partial U^2 = \left[2.11\ Pa\left(\sqrt{\frac{2}{1.07\ kg/m^3}}\left(\frac{1}{2\sqrt{183.18\ Pa}}\right)\right)\right]^2 + \left[0.004\ kg/m^3 \cdot \left(\frac{-1}{2}\sqrt{2\cdot 183.18\ Pa}\left(\left(1.07\ kg/m^3\right)^{-3/2}\right)\right)\right]^2 \quad [D28]$$

$$\partial U^2 = [0.15]^2 + [0.03]^2 \quad [D29]$$

$$\partial U = 0.15\ m/s \quad [D30]$$

5) Reynolds Number

The derivation of the Reynolds number was shown in the Theory section at Equation [28] in the general form:

$$\mathrm{Re} = \frac{\rho U l}{\mu} \quad [D31]$$

where:

ρ	=	ρ_{air}	Density of Air	(1.07 kg/m^3)
U	=	U_F	Corrected Wind Velocity	(25.69 m/s)
l	=	c	Airfoil Chord Length	(0.200 m)
μ	=	μ_{air}	Dynamic Viscosity of Air	(1.83 x 10^{-5} Ns/m^2)

$$\mathrm{Re} = \frac{\left(1.07\ {}^{kg}/_{m^3}\right)\cdot\left(25.69\ {}^{m}/_{s}\right)\cdot(0.200\ m)}{0.0000183\ {}^{N\cdot s}/_{m^2}} \qquad [D32]$$

$$\mathrm{Re} = 300418 \qquad [D33]$$

6) Reynolds Number Uncertainty

Following the general uncertainty equation as derived in the Theory section and shown by Equation [65].

$$\partial y^2 = \left(\partial x_1 \cdot \frac{\delta y}{\delta x_1}\right)^2 + \left(\partial x_2 \cdot \frac{\delta y}{\delta x_2}\right)^2 + \ldots + \left(\partial x_n \cdot \frac{\delta y}{\delta x_n}\right)^2 \qquad [D34]$$

The uncertainty of the Reynolds number can be determined.

$$(\partial \mathrm{Re})^2 = \left[\partial \rho_{air} \frac{\delta \mathrm{Re}}{\delta \rho_{air}}\right]^2 + \left[\partial U_F \frac{\delta \mathrm{Re}}{\delta U_F}\right]^2 + \left[\partial c \frac{\delta \mathrm{Re}}{\delta c}\right]^2 + \left[\partial \mu \frac{\delta \mathrm{Re}}{\delta \mu}\right]^2 \qquad [D35]$$

The uncertainty of the dynamic viscosity is assumed to be zero because it was not measured, therefore:

$$(\partial \mathrm{Re})^2 = \left[\partial \rho_{air} \frac{U_F \cdot c}{\mu}\right]^2 + \left[\partial U_F \frac{\rho_{air} \cdot c}{\mu}\right]^2 + \left[\partial c \frac{U_F \cdot \rho_{air}}{\mu}\right]^2 + 0 \qquad [D36]$$

Entering the values that have been previously determined in this section render the following:

$$(\partial \mathrm{Re})^2 = [112.36]^2 + [1754.10]^2 + [1502.10]^2 + 0 \qquad [D37]$$

$$\partial \mathrm{Re} = 2312.10 \qquad [D38]$$

7) Liquid Water Content

The liquid water content is a parameter that relates the mass of water crossing a vertical plane at the wing to the volume of air flowing past the wing (Marchman et al. 1987). As noted by Bilanin (1985), water injection systems in experiments do not simulate the water droplet size and droplet scattering distributions or the mean distance between droplets well. Therefore, the LWC is a preferred method to denote the rainfall intensity at the wing as opposed to rain rates. The liquid water content was shown in Equation [20] in the Theory section.

$$LWC = \frac{\dot{m}_w}{U_o \cdot A} \qquad [D39]$$

where: $\dot{m}_w$ = Water Mass Flow Rate (12.5 kg/hr)
U_o = Free Stream Velocity (25.69 m/s)
A = Area of Spray Diameter (0.025 m^2)

LWC is typically presented in units of g/m^3, therefore conversion factors are necessary:

$$LWC = \frac{\left(12.5\ {}^{kg}/_{hr}\right)\cdot\left(1000\ {}^{g}/_{kg}\right)}{\left(25.69\ {}^{m}/_{s}\right)\cdot\left(3600\ {}^{s}/_{hr}\right)\cdot\left(0.025\ m^2\right)} \qquad [D40]$$

$$LWC = 5.37\ {}^{g}/_{m^3} \qquad [D41]$$

8) Lift and Drag Conversions

After the data acquisition system was calibrated, the output voltage from the strain gauges were converted into a normal and chord-wise component of force. To convert the normal and chord-wise components of force into the lift and drag of the airfoil, Equation [58] and [59] were used, respectively.

$$Lift = N\cos(\alpha) - X\sin(\alpha) \qquad [D42]$$

$$Drag = N\sin(\alpha) + X\cos(\alpha) \qquad [D43]$$

where: N = Normal Component of Force (2.721 N)
X = Chord-wise Component of Force (-0.283 N)
α = Angle of Attack (6°)
Lift = Lifting Force of Airfoil (N)
Drag = Dragging Force of Airfoil (N)

$$Lift = (2.721\,N)\cos(6°) - (-0.283\,N)\sin(6°) \quad [D44]$$

$$Lift = 2.736\,N \quad [D45]$$

$$Drag = (2.721\,N)\sin(6°) + (-0.283\,N)\cos(6°) \quad [D46]$$

$$Drag = 0.027\,N \quad [D47]$$

From the Lift and Drag, the coefficient of lift, C_l, and the coefficient of Drag, C_d, were calculated using Equations [60] and [61], respectively.

$$C_l = \frac{Lift}{\frac{1}{2}\rho_{air}U^2 A_p} \quad [D48]$$

$$C_d = \frac{Drag}{\frac{1}{2}\rho_{air}U^2 A_p} \quad [D49]$$

where: A_p = Planform Area of Airfoil (0.00508 m^2)
C_l = Coefficient of Lift (dimensionless)
C_d = Coefficient of Drag (dimensionless)

$$C_l = \frac{2.736\,N}{\frac{1}{2}\left(1.07\,{}^{kg}/_{m^3}\right)\cdot\left(18.50\,{}^{m}/_{s}\right)^2\left(0.00508\,m^2\right)} \quad [D50]$$

$$C_l = 2.941 \quad [D51]$$

$$C_d = \frac{0.027\,N}{\frac{1}{2}\left(1.07\,{}^{kg}/_{m^3}\right)\cdot\left(18.5\,{}^{m}/_{s}\right)^2\left(0.00508\,m^2\right)} \quad [D52]$$

$$C_d = 0.029 \quad [D53]$$

9) Coefficient of Lift and Drag Uncertainties

The uncertainty associated with the coefficient of lift and drag are determined from using the measured lift and drag and the uncertainty associated with the angle of attack as determined in [81] and [82].

$$(\partial Lift)^2 = [\partial N\cos\alpha]^2 + [\partial X\sin\alpha]^2 + [\partial\alpha(-N\sin\alpha - X\cos\alpha)]^2 \quad [D54]$$

$$(\partial Drag)^2 = [\partial N \sin\alpha]^2 + [\partial X \cos\alpha]^2 + [\partial\alpha(N\cos\alpha - X\sin\alpha)]^2 \quad [D55]$$

The uncertainty of the angle of attack (α) was 1° and the uncertainty of the measured normal and chord wise force were determined to be 5% from the accuracy of the data acquisition system. These assumptions gives the following uncertainties:

$$\begin{aligned}(\partial Lift)^2 &= [(0.05\cdot 2.721\ N)\cos(0.070\ rads)]^2 \\ &+ [(0.05\cdot -0.283\ N)\sin(0.070\ rads)]^2 \\ &+ [0.0175\ rads(-2.271\ N\sin(0.070\ rads) + 0.283\ N\cos(0.070\ rads)]^2\end{aligned} \quad [D56]$$

$$\partial Lift = 0.135\ N \quad [D57]$$

$$\begin{aligned}(\partial Drag)^2 &= [(0.05\cdot 2.721\ N)\sin(0.070\ rads)]^2 \\ &+ [(0.05\cdot -0.283\ N)\cos(0.070\ rads)]^2 \\ &+ [0.0175\ rads(2.721\ N\cos(0.070\ rads) + 0.283\ N\sin(0.070\ rads)]^2\end{aligned} \quad [D58]$$

$$\partial Drag = 0.052\ N \quad [D59]$$

The uncertainty in the measurements in the lift and drag are then used to determine the uncertainty in the coefficient of lift and drag. Equations [81] and [82] were used to determine the uncertainty in lift and drag respectively.

$$\begin{aligned}(\partial C_l)^2 &= \left[\partial Lift\left(\frac{1}{0.5\rho_{air}U^2A_p}\right)\right]^2 + \left[\partial\rho_{air}\left(\frac{-Lift}{0.5\rho_{air}^2U^2A_p}\right)\right]^2 \\ &+ \left[\partial U\left(\frac{-2\cdot Lift}{0.5\rho_{air}^2U^3A_p}\right)\right]^2 + \left[\partial A_p\left(\frac{-Lift}{0.5\rho_{air}U^2A_p^2}\right)\right]^2\end{aligned} \quad [D60]$$

$$\begin{aligned}(\partial C_d)^2 &= \left[\partial Drag\left(\frac{1}{0.5\rho_{air}U^2A_p}\right)\right]^2 + \left[\partial\rho_{air}\left(\frac{-Drag}{0.5\rho_{air}^2U^2A_p}\right)\right]^2 \\ &+ \left[\partial U\left(\frac{-2\cdot Drag}{0.5\rho_{air}^2U^3A_p}\right)\right]^2 + \left[\partial A_p\left(\frac{-Drag}{0.5\rho_{air}U^2A_p^2}\right)\right]^2\end{aligned} \quad [D61]$$

$$(\partial C_l)^2 = \left[0.135\,N\left(\frac{1}{0.5\cdot(1.07\,{}^{kg}/_{m^3})\cdot(18.5\,m/s)^2\cdot(0.00508\,m^2)}\right)\right]^2 +$$
$$\left[0.004\,{}^{kg}/_{m^3}\left(\frac{-2.736\,N}{0.5\cdot(1.07\,{}^{kg}/_{m^3})^2\cdot(18.5\,m/s)^2\cdot(0.00508\,m^2)}\right)\right]^2$$
$$+\left[0.15\,m/s\left(\frac{-2\cdot 2.736\,N}{0.5\cdot(1.07\,{}^{kg}/_{m^3})\cdot(18.5\,m/s)^3\cdot(0.00508\,m^2)}\right)\right]^2$$
$$+\left[0.000001\,m^2\left(\frac{-2.736\,N}{0.5\cdot(1.07\,{}^{kg}/_{m^3})\cdot(18.5\,m/s)^2\cdot(0.00508\,m^2)^2}\right)\right]^2 \qquad [D62]$$

$$\partial C_l = 0.027 \qquad [D63]$$

$$(\partial C_d)^2 = \left[0.135\,N\left(\frac{1}{0.5\cdot(1.07\,{}^{kg}/_{m^3})\cdot(18.5\,m/s)^2\cdot(0.00508\,m^2)}\right)\right]^2 +$$
$$\left[0.004\,{}^{kg}/_{m^3}\left(\frac{-0.027\,N\,N}{0.5\cdot(1.07\,{}^{kg}/_{m^3})^2\cdot(18.5\,m/s)^2\cdot(0.00508\,m^2)}\right)\right]^2$$
$$+\left[0.15\,m/s\left(\frac{-2\cdot 0.027\,N}{0.5\cdot(1.07\,{}^{kg}/_{m^3})\cdot(18.5\,m/s)^3\cdot(0.00508\,m^2)}\right)\right]^2$$
$$+\left[0.000001\,m^2\left(\frac{-0.027\,N}{0.5\cdot(1.07\,{}^{kg}/_{m^3})\cdot(18.5\,m/s)^2\cdot(0.00508\,m^2)^2}\right)\right]^2 \qquad [D64]$$

$$\partial C_d = 0.009 \qquad [D65]$$

Appendix E

Contents:

Lift and Drag Data

1) Dry Conditions – Clean Surface Airfoil

Re 100,000

Angle of Attack (deg)	Cl	Cd
0	0.465	0.156
2	0.402	0.049
4	0.883	0.119
6	0.934	0.093
8	1.598	0.138
10	2.015	0.106
12	1.985	0.154
14	2.042	0.163
16	2.152	0.313

Re 150,000

Angle of Attack (deg)	Cl	Cd
0	0.613	0.059
2	0.807	0.017
4	1.275	0.022
6	1.464	0.019
8	1.896	0.052
10	1.968	0.062
12	2.046	0.106
14	2.003	0.104
16	2.076	0.179

Re 200,000

Angle of Attack (deg)	Cl	Cd
0	0.631	0.033
2	0.848	0.001
4	1.200	0.003
6	1.475	0.014
8	1.757	0.028
10	1.888	0.032
12	1.914	0.061
14	1.924	0.081
16	1.955	0.146

Re 250,000

Angle of Attack (deg)	Cl	Cd
0	0.682	0.025
2	0.934	0.005
4	1.274	0.006
6	1.577	0.004
8	1.817	0.019
10	1.960	0.033
12	2.033	0.059
14	2.047	0.090
16	2.081	0.145

Re 300,000

Angle of Attack (deg)	Cl	Cd
0	0.829	0.012
2	1.051	0.007
4	1.344	0.005
6	1.616	0.002
8	1.757	0.002
10	1.849	0.015
12	1.881	0.044
14	1.911	0.085
16	1.921	0.151

2) Dry Conditions – Hydrophilic Coated Airfoil

Re 100,000

Angle of Attack (deg)	Cl	Cd
0	0.557	0.045
2	0.642	0.069
4	0.559	0.159
6	0.869	0.137
8	1.192	0.147
10	1.517	0.082
12	1.634	0.091
14	1.457	0.152
16	1.484	0.200

Re 150,000

Angle of Attack (deg)	Cl	Cd
0	0.768	0.013
2	0.937	0.028
4	1.204	0.059
6	1.385	0.033
8	1.669	0.062
10	1.811	0.049
12	1.898	0.093
14	1.790	0.131
16	1.902	0.172

Re 200,000

Angle of Attack (deg)	Cl	Cd
0	0.707	0.015
2	0.984	0.022
4	1.201	0.037
6	1.491	0.028
8	1.656	0.039
10	1.883	0.053
12	1.895	0.088
14	1.804	0.104
16	2.029	0.166

Re 250,000

Angle of Attack (deg)	Cl	Cd
0	0.719	0.010
2	1.025	0.022
4	1.251	0.029
6	1.573	0.026
8	1.795	0.037
10	1.867	0.052
12	1.938	0.073
14	2.039	0.130
16	1.981	0.169

Re 300,000

Angle of Attack (deg)	Cl	Cd
0	0.730	0.011
2	1.026	0.018
4	1.248	0.026
6	1.520	0.025
8	1.793	0.032
10	1.979	0.043
12	1.938	0.090
14	2.016	0.129
16	1.980	0.170

3) Dry Conditions – Hydrophobic Coated Airfoil

Re 100,000

Angle of Attack (deg)	Cl	Cd
0	0.237	0.003
2	0.515	0.038
4	0.678	0.049
6	0.903	0.188
8	1.222	0.136
10	1.511	0.105
12	1.544	0.118
14	1.612	0.190
16	1.094	0.297

Re 150,000

Angle of Attack (deg)	Cl	Cd
0	0.591	-0.021
2	0.968	0.020
4	1.171	0.034
6	1.499	0.111
8	1.697	0.061
10	1.626	0.077
12	1.785	0.085
14	1.714	0.142
16	1.746	0.180

Re 200,000

Angle of Attack (deg)	Cl	Cd
0	0.672	-0.023
2	1.023	0.008
4	1.258	0.024
6	1.551	0.063
8	1.685	0.035
10	1.650	0.046
12	1.745	0.067
14	1.663	0.111
16	1.787	0.166

Re 250,000

Angle of Attack (deg)	Cl	Cd
0	0.737	-0.031
2	1.090	0.005
4	1.313	0.016
6	1.610	0.052
8	1.719	0.020
10	1.810	0.040
12	1.798	0.051
14	1.812	0.101
16	1.812	0.159

Re 300,000

Angle of Attack (deg)	Cl	Cd
0	0.746	-0.030
2	1.093	-0.008
4	1.322	0.009
6	1.562	0.015
8	1.649	0.019
10	1.717	0.022
12	1.738	0.047
14	1.772	0.113
16	1.758	0.161

4) Wet Conditions – Clean Surface Airfoil

Re 100,000

Angle of Attack (deg)	Cl	Cd
0	0.682	0.200
2	1.103	0.051
4	1.195	0.061
6	1.394	0.171
8	1.545	0.035
10	2.001	0.088
12	1.630	0.052
14	1.743	0.249
16	1.948	0.217

Re 150,000

Angle of Attack (deg)	Cl	Cd
0	0.700	0.081
2	1.032	0.028
4	1.282	0.078
6	1.487	0.072
8	1.738	0.045
10	1.964	0.008
12	1.894	0.049
14	1.858	0.103
16	1.785	0.161

Re 200,000

Angle of Attack (deg)	Cl	Cd
0	0.705	0.051
2	0.982	0.027
4	1.423	0.010
6	1.744	0.035
8	2.068	0.006
10	1.862	0.015
12	2.234	0.026
14	1.892	0.087
16	1.960	0.114

Re 250,000

Angle of Attack (deg)	Cl	Cd
0	0.731	0.033
2	1.002	0.027
4	1.546	0.025
6	1.802	0.028
8	2.047	0.010
10	2.156	0.032
12	1.919	0.076
14	1.970	0.118
16	1.934	0.141

Re 300,000

Angle of Attack (deg)	Cl	Cd
0	0.801	0.034
2	0.995	0.027
4	1.499	0.014
6	1.756	0.031
8	2.005	0.027
10	2.082	0.054
12	1.921	0.062
14	1.905	0.112
16	1.955	0.150

5) Wet Conditions – Hydrophilic Coated Airfoil

Re 100,000

Angle of Attack (deg)	Cl	Cd
0	0.660	0.115
2	0.755	0.215
4	1.155	0.147
6	1.340	0.135
8	1.501	0.082
10	1.758	0.163
12	1.850	0.241
14	1.872	0.203
16	1.822	0.197

Re 150,000

Angle of Attack (deg)	Cl	Cd
0	0.703	0.055
2	0.903	0.066
4	1.236	0.072
6	1.505	0.082
8	1.590	0.051
10	1.722	0.086
12	1.918	0.128
14	1.860	0.144
16	1.826	0.170

Re 200,000

Angle of Attack (deg)	Cl	Cd
0	0.743	0.024
2	0.970	0.035
4	1.252	0.020
6	1.513	0.039
8	1.583	0.011
10	1.822	0.043
12	1.854	0.067
14	1.922	0.081
16	1.981	0.141

Re 250,000

Angle of Attack (deg)	Cl	Cd
0	0.747	0.015
2	1.050	0.024
4	1.302	0.003
6	1.576	0.014
8	1.732	0.015
10	1.873	0.051
12	1.923	0.086
14	2.014	0.138
16	2.021	0.178

Re 300,000

Angle of Attack (deg)	Cl	Cd
0	0.763	0.013
2	1.023	0.008
4	1.293	-0.001
6	1.575	0.013
8	1.728	0.015
10	1.852	0.049
12	1.879	0.099
14	1.987	0.134
16	2.023	0.193

6) Wet Conditions – Hydrophobic Coated Airfoil

Re 100,000

Angle of Attack (deg)	Cl	Cd
0	0.444	0.074
2	0.724	0.062
4	0.968	0.101
6	1.153	0.132
8	1.111	0.143
10	1.178	0.213
12	0.935	0.228
14	1.256	0.371
16	1.360	0.390

Re 150,000

Angle of Attack (deg)	Cl	Cd
0	0.544	0.055
2	0.734	0.032
4	0.859	0.068
6	1.059	0.083
8	1.177	0.123
10	1.177	0.152
12	1.213	0.200
14	1.355	0.332
16	1.280	0.361

Re 200,000

Angle of Attack (deg)	Cl	Cd
0	0.539	0.037
2	0.779	0.037
4	0.870	0.060
6	1.019	0.061
8	1.168	0.113
10	1.218	0.136
12	1.313	0.190
14	1.302	0.274
16	1.315	0.334

Re 250,000

Angle of Attack (deg)	Cl	Cd
0	0.575	0.025
2	0.787	0.040
4	0.919	0.041
6	1.103	0.061
8	1.212	0.075
10	1.341	0.098
12	1.422	0.169
14	1.448	0.255
16	1.458	0.344

Re 300,000

Angle of Attack (deg)	Cl	Cd
0	0.614	0.008
2	0.798	0.024
4	0.970	0.021
6	1.116	0.038
8	1.260	0.057
10	1.369	0.087
12	1.458	0.142
14	1.494	0.229
16	1.514	0.287

7) Comparison of Theoretical Data to Experimental Data

Airfoil Polar from PANDA

Re = 300000.00 USgrit = 1.0000 LSgrit = 1.0000 Mach = 0.000

	Theoretical		Clean	
Alpha	CL	CD	CL	CD
0	0.711059	0.011501	0.829	0.012
2	0.9572	0.011928	1.051	0.007
4	1.195898	0.01269	1.344	0.005
6	1.425989	0.013855	1.616	0.002
8	1.646353	0.015657	1.757	0.002
10	1.855917	0.017466	1.849	0.015
12	2.05366	0.023431	1.881	0.044
14	2.238616	-	1.911	0.085
16	2.409887	-	1.921	0.151

	Hydrophilic		Hydrophobic	
Alpha	CL	CD	CL	CD
0	0.730423	0.010873	0.746	0.004
2	1.02617	0.015373	1.093	0.004
4	1.247684	0.018886	1.322	0.009
6	1.519529	0.024782	1.562	0.015
8	1.792569	0.031505	1.649	0.019
10	1.979331	0.043035	1.717	0.022
12	2.007376	0.072991	1.738	0.047
14	2.016328	0.117815	1.772	0.097
16	2.02202	0.170474	1.758	0.161

8) Comparison of Surface Wettability in Simulated Rain

Dry - Clean Airfoil Surface

Angle of Attack (degrees)	Cl (unitless)	Cd (unitless)
0	0.8286	0.0118
2	1.0511	0.0070
4	1.3444	0.0052
6	1.6158	0.0024
8	1.7566	0.0022
10	1.8493	0.0154
12	1.8806	0.0440
14	1.9111	0.0854
16	1.9211	0.1509

Wet - Clean Airfoil Surface

Angle of Attack (degrees)	Cl (unitless)	Cd (unitless)
0	0.7180	0.0127
2	0.9841	0.0122
4	1.2016	0.0105
6	1.3960	0.0154
8	1.4880	0.0269
10	1.5562	0.0446
12	1.6117	0.0857
14	1.6216	0.1288
16	1.5814	0.1973

Wet - Hydrophilic Coated Surface

Angle of Attack (degrees)	Cl (unitless)	Cd (unitless)
0	0.7525	0.0024
2	1.0230	0.0016
4	1.3350	0.0024
6	1.5576	0.0009
8	1.7215	0.0117
10	1.8080	0.0331
12	1.8510	0.0714
14	1.8781	0.1130
16	1.8878	0.1658

Wet - Hydrophobic Coated Surface

Angle of Attack (degrees)	Cl (unitless)	Cd (unitless)
0	0.6729	0.0098
2	0.8609	0.0057
4	1.0236	0.0073
6	1.1951	0.0129
8	1.2687	0.0300
10	1.3590	0.0556
12	1.4599	0.1071
14	1.4415	0.1652
16	1.4327	0.2537

Appendix F

Contents:

1) PANDA Input File

```
! Airfoil Coordinates for PANDA
! x        yup          ylo
  0.000000    0.000000    -0.000000
  0.001541    0.006606    -0.009939
  0.006156    0.018123    -0.017325
  0.013815    0.031871    -0.022801
  0.024472    0.044452    -0.027022
  0.038060    0.055545    -0.030581
  0.054497    0.066798    -0.033999
  0.073680    0.077503    -0.037453
  0.095491    0.087845    -0.040190
  0.119797    0.097535    -0.042462
  0.146447    0.106528    -0.044459
  0.175276    0.114740    -0.045597
  0.206107    0.122025    -0.046444
  0.238751    0.128329    -0.047027
  0.273005    0.133540    -0.046997
  0.308658    0.137559    -0.046508
  0.345491    0.140305    -0.045597
  0.383277    0.141514    -0.044553
  0.421783    0.141091    -0.042823
  0.460770    0.138902    -0.040647
  0.500000    0.134648    -0.038303
  0.539229    0.128654    -0.035357
  0.578217    0.121315    -0.031907
  0.616723    0.113208    -0.028621
  0.654508    0.104598    -0.025199
  0.691342    0.095665    -0.021647
  0.726995    0.086653    -0.018319
  0.761249    0.077629    -0.014953
  0.793893    0.068579    -0.011239
  0.824724    0.059886    -0.007541
  0.853553    0.051478    -0.004107
  0.880203    0.043502    -0.001261
  0.904508    0.036169     0.000192
  0.926320    0.029380     0.004365
  0.945503    0.023064     0.001585
  0.961940    0.017012     0.001141
  0.975528    0.011456     0.001554
  0.986185    0.006712     0.001414
  0.993844    0.003073     0.000843
  0.998459    0.000782     0.000247
  1.000000    0.000000     0.000000
end
```

2) PANDA Output File

! Airfoil Polar from PANDA
! Re = 300000.00 USgrit = 1.0000 LSgrit = 1.0000 Mach = 0.000

! Alpha	CL	Cm	CD
0.000000	0.711059	-0.163166	0.011501
1.000000	0.834986	-0.164789	0.011638
2.000000	0.957200	-0.166558	0.011928
3.000000	1.077553	-0.168471	0.012280
4.000000	1.195898	-0.170526	0.012690
5.000000	1.312090	-0.172721	0.012806
6.000000	1.425989	-0.175052	0.013855
7.000000	1.537455	-0.177518	0.014530
8.000000	1.646353	-0.180114	0.015657
9.000000	1.752551	-0.182838	0.016415
10.000000	1.855917	-0.185686	0.017466
11.000000	1.956328	-0.188655	0.019678
12.000000	2.053660	-0.191742	0.023431
13.000000	2.147794	-0.194942	0.000000
14.000000	2.238616	-0.198251	0.000000
15.000000	2.326016	-0.201667	0.000000
16.000000	2.409887	-0.205184	0.000000

end

Appendix G

Contents:

1) MIWT Set Point Chart

Data sheet that was placed on the control panel of the MIWT. This relates the Reynolds number to the inclined manometer reading (inches of gauge fluid).

Reynolds Number (unitless)	Corrected Velocity (m/s)	Free stream Velocity (m/s)	Manometer Reading (in g.f.)
96319	8.14	5.87	0.09
101529	8.61	6.19	0.10
106485	9.03	6.49	0.11
147130	12.47	8.97	0.21
150592	12.76	9.18	0.22
106485	13.05	9.39	0.23
197917	16.78	12.07	0.38
200504	17.00	12.23	0.39
203059	17.21	12.38	0.40
248695	21.08	15.17	0.60
250759	21.25	15.29	0.61
252806	21.43	15.42	0.62
299468	25.38	18.26	0.87
301185	25.53	18.36	0.88
302891	25.67	18.47	0.89